

ISSN 0377-9416



www.pmai.in

TRANSACTIONS OF POWDER METALLURGY ASSOCIATION OF INDIA

Vol. 47, June-December 2022

Chief Editor - Prof. Ramakrishnan P.

ISSN 0377-9416



www.pmai.in

TRANSACTIONS OF POWDER METALLURGY ASSOCIATION OF INDIA

Vol. 47, June-December 2022

Chief Editor - **Prof. Ramakrishnan P.**



Powder Metallurgy Association of India

Office Bearers

President

Mr. Aniket Gore

Vice President

Dr. N. B. Dhokey

Mr. Sandeep Fatangare

Mr. Rajendra Sethiya

Mr. Niranjana Narkhede

General Secretary

Mr. Prakash Khole

Joint Secretary

Dr. Malobika Karanjai

Mr. Deepak Kumar Pattanayak

Hon. Treasurer

Mr. Mahesh Nipanikar



Chief Editor

Prof. Ramakrishnan P.

Editorial Advisory Board

Dr. Ashok S.

Mr. Chandrachud N.L.

Editorial Board

Dr. Appa Rao G.

Dr. Bhargava Parag

Dr. Dabhade Vikram

Dr. Dhokey N. B.

Dr. Deep Prakash

Dr. Kumar Y.V.S.

Dr. Malobika Karanjai

Dr. Murli Gopal K.

Dr. Panigrahi B.B.

Dr. Sastry I.S.R.

Dr. Tarasankar Mahata

Published by :

Powder Metallurgy Association of India (PMAI)

102, Anandi, 1st Floor,

M.B. Raut Road, Shivaji Park,

Dadar, Mumbai - 400028, India

Tel.: +91 9820951180

+91 9821111677

E-mail: info@pmai.in

Neither the Powder Metallurgy Association of India nor the editor assumes responsibility of opinions expressed by the authors of the papers published in this transaction.

Editorial



This edition of Trans. PMAI. Vol.47, 2022, contains selected papers from the International Conference on PM 22, conducted in virtual mode during April 2022. The first paper is the Tamhankar Memorial lecture entitled Tungsten heavy alloys: processing, microstructure and mechanical behavior dealing with the physical metallurgy of Tungsten heavy alloys for

kinetic energy penetrator applications. Next paper is on the effect of alumina content on the phase development and mechanical properties of alumina-mullite composite synthesized from alluvial clay of the Indian Ganches. This is followed by a review paper on the evolution, stability and transformation of phases in high entropy alloys which are emerging class of materials. Synthesis and characterization of Magnesium aluminate spinel through solid state sintering is the subject matter of the next paper. Assessment of the tribological behavior of silicon nitride reinforced aluminium alloy composite against EN 31 steel, unlubricated condition of varying loads and sliding distances have been investigated and reported. This is followed by a paper on the synthesis of nanostructured equiatomic TiCrFeCoNi alloy by mechanical alloying and sintering. Next paper is on the optimizing metal powders for cold isostatic pressing by analytical techniques such as image analysis, X ray diffraction and X ray fluorescence. This is followed by a paper proposing few MIM components for Off Highway industry. The growth from research to industry of field assisted sintering and spark plasma sintering is discussed in the next paper. This is followed by a paper on the densification and characterization of sintered

ZrB₂-20 Vol.% MoSi₂ ultrahigh temperature ceramic composites. Next paper is on the fabrication and characterization of carbon nanotube dispersed aluminium composites. This is followed by a review paper on the effect of different reinforcement on the properties of copper matrix composites. Final paper is on the cost saving opportunities by using PM components in agricultural, construction and forestry machines.

Prof. Ramakrishnan P.

TRANSACTIONS OF
POWDER METALLURGY ASSOCIATION OF INDIA

Vol. 47, June-December 2022

CONTENTS

- 1 *R. V. Tamhankar Memorial lecture*
Tungsten Heavy Alloys: Processing, Microstructure and Mechanical Behavior 1-8
U Ravi Kiran, G Prabhu and TK Nandy

- 2 **Effect of Alumina Content on the Phase Development and Mechanical Properties of Alumina-mullite Composite Synthesized from Alluvial Clay of the Ganges** 9-18
Arpan Kool, Runumi Seal, Somtirtha Kool Banerjee, Sukhen Das

- 3 **A Review on Evolution, Stability, and Transformation of Phases in High Entropy Alloys (HEAs)** 19-31
Manashi Sabat, Gourahari Behera, Manila Mallik

- 4 **Synthesis and Characterization of Magnesium Aluminate ($MgAl_2O_4$) Spinel Through Solid State Pressureless Sintering** 32-40
Abdur Roufa, Krishna Priya Yagatia and Manab Mallika

- 5 **Assessment of the Tribological Behavior of a Metallic Tribopair: LM25 alloy- Si_3N_4 Composites Against EN 31 Steel** 41-50
Zeeshan Ahmad, Sabah Khan, Ronaldo Câmara Cozza, Ramkumar Penchaliah, Vikas Verma

- 6 **Synthesis of Nanostructured Equiatomic TiCrFeCoNi High-Entropy Alloy by Mechanical Alloying and Conventional Sintering** 51-57
Vikas Shivam, Vadapalli Sanjana, Yagnesh Shadangi, V.C. Srivastava and N.K. Mukhopadhyay

- 7 **Optimizing Metal Powders for Cold Isostatic Pressing** 58-61
Anand Tadas, Nicholas Norberg, John Duffy

- 8 **Use of Metal Injection Moulding (MIM)- Off Highway Industry Perspective** 62-65
Manish Gokhale

- 9 **From Research to Industry - Applications and Latest Developments in the Field of FAST/SPS Sintering** 66-76
Jens Huber

10 Densification and Characterization of Pressureless Sintered ZrB₂-20 vol% MoSi₂ Ultra High Temperature Ceramic Composites	77-82
<i>Manab Mallik, Mainak Saha, Sayantani Santra, Sushree Ananya Tanaya, Sonam Kumari and Divyadutta Behura</i>	
<hr/>	
11 Fabrication and Characterizations of Carbon Nanotube Dispersed Aluminum Composites	83-89
<i>Saptarshi Saha, Lokesh Sarkar, Apurba Das, Arijit Sinha</i>	
<hr/>	
12 A Short Review on the Effect of Ceramic Particles, MWCNT, and Graphene on the Properties of Cu Matrix Composites by Powder Metallurgy Route	90-95
<i>Saroj Kumar Saha, Suhree P Mohapatraa, Dinesh Kumar Mishraa, Renu Prava Dalaia</i>	
<hr/>	
13 Cost Saving Opportunities Using PM & Approach Used in Off Highway Vehicles	96-98
<i>Amol Devikar</i>	

TUNGSTEN HEAVY ALLOYS: PROCESSING, MICROSTRUCTURE AND MECHANICAL BEHAVIOR

U Ravi Kiran, G Prabhu and TK Nandy

Defence Metallurgical Research Laboratory, Hyderabad, India.

Email - nandy@dmrl.drdo.in

Abstract: Physical metallurgy of tungsten heavy alloys for kinetic energy penetrator application that demands enhanced levels of mechanical properties has been discussed. The effects of alloy chemistry, sintering parameters, heat treatment and swaging have been briefly described followed by elucidation of microstructures. Mechanical properties that include strength and toughness have been briefly described. Scatter in mechanical properties given that the alloy is processed using powder metallurgy technique has been highlighted and possible means to alleviate this issue discussed. Recent developments especially in sintering and thermomechanical processing have been highlighted. Finally, the status and future direction for heavy alloys and other promising alloy systems have been presented.

1. Introduction

Tungsten heavy alloys possess excellent balance of physical and mechanical properties which include superior corrosion resistance, elevated strength, high elastic modulus and high density. These render the alloy suitable for a variety of applications such as weight adjusters, ballasts, radiation shields, electrical contact, cubes/ prefragments in warheads and kinetic energy penetrators (Cai et al. 1995, Upadhyaya 2001, Sahin 2014). Ever since the inception of these alloys almost 5 decades back, the development of the alloy still continues, and it has been traditionally driven by continuously advancing kinetic energy penetrators (KEP) used in main battle tanks.

Kinetic energy penetrators (KEP) have evolved over a period and the first instance of application of tungsten in KEP was in form of tungsten carbide (hard core) because its hardness and relatively higher density. Subsequently, tungsten carbide was replaced by tungsten heavy alloy primarily because of the brittleness of tungsten carbide that leads to fracture of the penetrating rod as it engages with the target (Lanz et al. 2001). Tungsten heavy alloys are referred to as soft core since they have significantly lower hardness as compared to tungsten carbide. The heavy alloy also has higher density that results in superior ballistic performance since the

depth of penetration is directly proportional to $(\text{density})^{1/2}$ (de Rossett 2001). Over last 6-7 decades, the depth of penetration has increased from around 300 to 800 mm or even 1000 mm in order to defeat continually developing armor systems. Accordingly, superior versions of heavy alloy penetrators have emerged and there has been a considerable improvement in the properties of heavy alloys as listed in Table 1.

In this overview, the development of tungsten heavy alloy has been discussed in terms of alloy chemistry, sintering, heat treatment and swaging. These are discussed especially in relation to microstructural features such as tungsten particle size, matrix volume fraction, matrix composition, tungsten-tungsten contiguity etc. The effect of different microstructural parameters on mechanical properties has been discussed. The issues related to scatter in mechanical properties are presented. Finally, the alternative materials that are emerging candidates for kinetic energy penetrators are also discussed.

Table 1: Mechanical properties of tungsten heavy alloy (Nicolas 1990, Lanz et al. 2001)

Year of development	1970	1978	1985	2015
Ultimate tensile strength, MPa	800	1200	1450	1800
% elongation	1-4	6	8	8

TUNGSTEN HEAVY ALLOYS: PROCESSING, MICROSTRUCTURE AND MECHANICAL BEHAVIOR

2. Processing of heavy alloys

Tungsten heavy alloys are processed using liquid phase sintering followed by thermomechanical processing. These are briefly described in the present section.

(a) Sintering

The alloys are subjected to liquid phase sintering to obtain oval shaped rods which are machined to cylindrical cross section rods, further subjected to processing. Typical sintering temperatures that are primarily dependent of tungsten content, are in the range of 1450-1500°C (Bose et al. 1989, Cai et al. 1995). Alloying additions that are also termed as dopants such as Ni, Fe, Co, Cu, Mo melt at sintering temperature (Eliasson et al. 2008), penetrate W-agglomerate, separate W particles and form a molten envelope surrounding tungsten particles. The growth of W particles that adopt nearly spherical morphology occurs by solution-reprecipitation which involves dissolution of smaller particles and growth of the coarser particles (Yang et al. 1990).

The resultant microstructure is nearly round W-particles (10-40 μm) surrounded by an FCC matrix phase (20-30%) depending on the tungsten content (Fig. 1). The matrix phase which is a solid solution of Ni, Fe, Co, Mo and W (Kumari

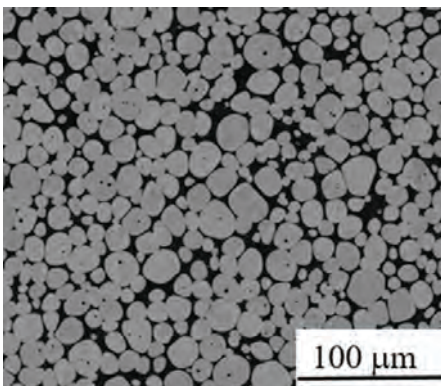


Fig. 1: Typical microstructure of a tungsten heavy alloy. Bright W particles surrounded by darker matrix

et al. 2017) that are dissolved in the liquid phase during sintering, holds the W particles (with very small amounts of alloying additions) together and imparts the alloy ductility that is needed for processing and applications.

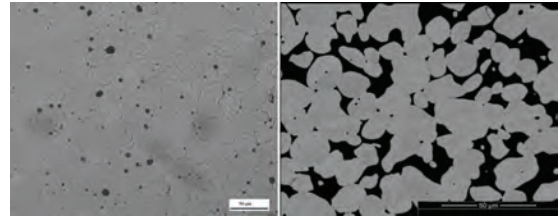


Fig. 2: Defects in tungsten heavy alloys (a) porosity, (b) irregular particles



Fig. 3: Oval cross section indicating excessive slumping

Sintering at lower temperature could lead to incomplete densification which would result in the formation of porosity and undesirable microstructure comprising W particles with irregular morphology (Fig. 2). Sintering at higher temperature results in slumping of the compact leading to sintered blank having an excessively oval cross section (Fig. 3) that would necessitate more machining and wastage of material. Lower sintering time will lead to incomplete sintering and higher sintering time will lead to coarsening of tungsten particles. Thus, there appears to be a narrow window of sintering time and

TUNGSTEN HEAVY ALLOYS: PROCESSING, MICROSTRUCTURE AND MECHANICAL BEHAVIOR

temperature. A typical microstructure of W-Ni-Fe alloy (low magnification picture) obtained after sintering at 1450°C for 60 min is shown in Fig. 4.

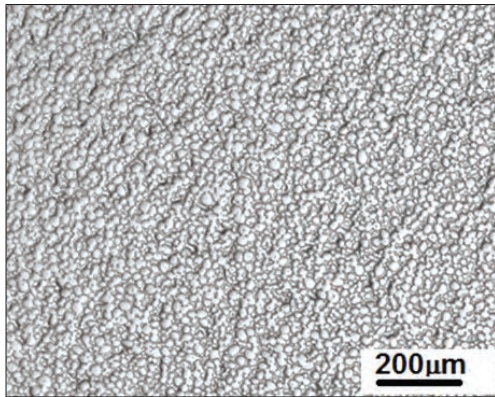


Fig. 4: Low magnification optical micrograph of a sintered heavy alloy

Sintering is usually carried out in dry hydrogen atmosphere (dew point <math>< -40\text{ }^\circ\text{C}</math>) in order to remove oxygen from the powder particles. However, during the final stages, a wet hydrogen cycle is employed in order to prevent the formation of water vapour inside the blank leading to porosity (Bose et al. 1989). A typical sintering cycle is shown in Fig. 5.

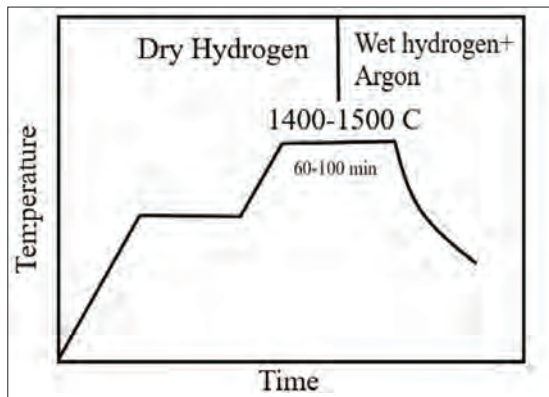


Fig. 5: Typical Sintering cycle for tungsten heavy alloy (Bose et al 1989)

Sometimes two stage sintering is employed which helps in densification to get a defect free product (Hong and Ryu 2003). Single stage sintering may sometimes lead to formation of crack because of rapid slumping of the green compact which may result in cracks. Additionally, complete densification is attained with relatively lower ovality in case of two stage sintered specimens. There is possibility of starting with oval cross section and ending with cylindrical cross section post sintering to avoid excessive machining. One of the sintering defects is matrix pool (Fig. 6), which may be avoided by fine-tuning the blending parameters and also employing appropriate sintering time-temperature window.

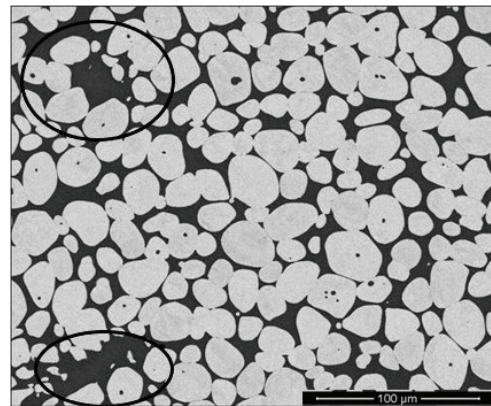


Fig. 6: Matrix pool due to incomplete sintering

(b) Heat Treatment

As sintered tungsten heavy alloys are brittle primarily because of three reasons: (1) dissolution of hydrogen during sintering, (2) segregation of impurities at the interface during cooling (3) intermetallic formation (Edmonds and Jones 1979). Therefore, the alloy is subjected to heat treatment that confers much needed ductility so that the blanks can be processed for realizing long rods. Sometimes, the heat treatment schedule may be slightly more elaborate to improve the impact toughness without significantly changing

the tensile properties. Cyclic heat treatment has been employed by Noh et al. (1993) that leads to significantly improved impact properties. Ravi Kiran et al. (2016) have shown that this improvement which is initially realized in heat treatment is also retained in swaged condition. W-Ni-Co alloys are given a special cyclic treatment that results in precipitation of fine W particles in the matrix (Stuitje et al. 1995). This innovative heat treatment has resulted in significant enhancement in mechanical properties especially the balance of tensile strength, % elongation and impact. Aging has also been attempted to improve tensile strength (Katavic and Odanovic 2005), however this needs to be examined with caution since enhancement of strength may be accompanied with compromise on other properties such as % elongation or impact.

(c) Swaging

Kinetic energy penetrator application that needs long rods (200-800 mm length) also demands high strength (1100-1600 MPa) with good elongation (>8%) and impact toughness > 100 J/cm². These strength levels cannot be attained in heat treated condition since the alloy is not a precipitation strengthening type, the microstructural features being relatively coarser (W particle size ~ 10-40 μm and the matrix mean free path~1-2 μm). Therefore, the alloys are processed by imparting deformation, swaging being the most preferred method. Generally, 20-40 % reduction is imparted with or without intermediate annealing. Strength level as high as 1850 MPa with elongation ranging from 4-5% has been achieved in 93% W alloy by imparting deformation of 35% along with heat treatment (Nicolas 1990). In a similar investigation carried out on 90% W-NiFeCo, 1700 MPa has been achieved following deformation of 75% (Ravi Kiran et al. 2012). Kumari et al. (2017) have shown that 1600 MPa with an impact toughness of 100J can be achieved by imparting

50% deformation in a heavy alloy with 90% W. Strength as a function of % swaging deformation is shown in Fig. 7

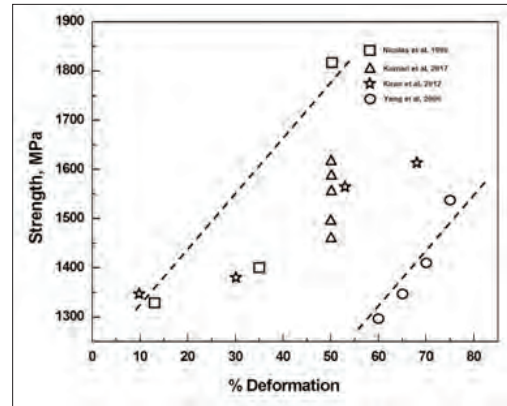


Fig. 7: Tensile strength of heavy alloys as a function of swaging deformation

3. Microstructure

As mentioned earlier, tungsten heavy alloy comprises two phases: W rich phase that contains a very small amount of alloying elements such as Ni, Fe and Co and an fcc matrix that is a solid solution of Ni, Fe, Co and W. There are four major microstructural parameters: (a) W particle size, (b) Matrix mean free path, (3) Matrix volume fraction and (4) W-W contiguity that is the fraction of W-W interface

The W particle size that varies from 10-40 μm depends on the sintering time-temperature window. The expression for W-particle size (Yang et al. 1990) is as follows:

$$r^{1/3} - r_0^{1/3} = Kt \tag{1}$$

Where r is the W particle radius at any given time t , r_0 is the initial radius, k is constant which is given by:

$$k = \frac{8X_o\sigma V_m^2 D}{9RT} f(V_s) \tag{2}$$

TUNGSTEN HEAVY ALLOYS: PROCESSING, MICROSTRUCTURE AND MECHANICAL BEHAVIOR

X_o is the equilibrium solubility of W in liquid, σ is the interfacial energy between particle and matrix, V_m is the molar volume of the particle, D is the diffusivity of W , $f(V_s)$ is the volume fraction modification parameter. There are three important parameters: the equilibrium solubility (X_o), diffusivity (D) and interface energy (σ). The alloying elements affect these parameters thereby influencing the particle size of tungsten. Mo is one of the elements that refine W particle size by decreasing the solubility of W in the matrix (Kemp et al.), Re also refines the microstructure by a similar mechanism (Ravi Kiran et al. 2015). Matrix mean free path that influences the yield strength of the alloy is dependent of W particle size and the matrix volume fraction.

Contiguity is another quantifiable parameter giving an estimate for the fraction for W - W interface which the weakest link in the microstructure as they act as potential void nucleation sites; Therefore, it has a key role in influencing tensile strength, % elongation to failure and impact toughness. Contiguity is affected by alloying additions. Kumari and coworkers (2017) have shown that increasing W in the matrix phase leads to reduction in contiguity, Co additions results in reduction in contiguity because of its influence on solid liquid interface energy. The relevant microstructural parameters are listed in Table 2.

Table 2: Microstructural parameters of tungsten heavy alloys

Microstructural parameters	92W-6.4Ni-1.6 Fe (Ni/Fe=8/2) Panchal et al. 2020	92W-5Ni-3Co (Ni/Co=5/3) Rao et al. 2015
W-grain size	33.4 ± 12.1	22.7
Matrix vol. %	22.0 ± 0.17	23
Contiguity (microstructure)	0.27 ± 0.05	0.24
Dihedral angle (degree)	42 ± 8	-
Connectivity	1.6 ± 0.8	-
Neck length, μm	11.9 ± 4.2	-

4. Mechanical Behavior

A typical stress-strain curve of a swaged W-Ni-Co alloy is shown in Fig.8. The curve is relatively flatter that indicates lower work hardening rate, reminiscent of beta titanium alloys that deform by planar slip (Bhattacharjee et al. 2007). Therefore, the values of yield strength and ultimate tensile strength often remain similar. On the other hand, the heat-treated alloy shows lower strength with perceptible work hardening. Lower work hardening of the alloy especially in as swaged condition is possibly due to two factors: (1) lower stacking fault of the matrix phase leading to planar slip (Das et al. 2014). (2) high dislocation density in the matrix phase, a result of swaging, that makes the initiation of macroscopic deformation difficult resulting in high strength but once the deformation initiates, further deformation is easier.

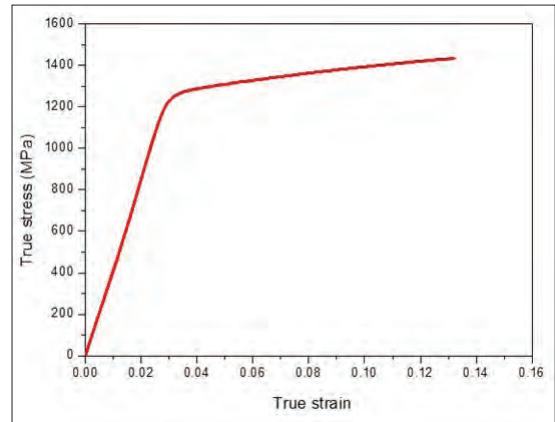


Fig. 8: Stress-strain curve of a swaged heavy alloy

The yield strength of the two-phase tungsten heavy alloy is dependent on W particle size (Ryu et al. 2000), which is expressed as:

$$\sigma_y = \sigma_o + k\sqrt{D}^{1/2} \quad (3)$$

$$\sigma_y = \sigma_o + kGb \left(\frac{1 - V_M}{DV_M} \right)^{1/2} \quad (4)$$

TUNGSTEN HEAVY ALLOYS: PROCESSING, MICROSTRUCTURE AND MECHANICAL BEHAVIOR

where σ_y is the yield strength, σ_o is the intrinsic strength, k is a constant, G is the shear modulus, b is the Burgers vector, D is the tungsten particle size and V_M is the matrix volume fraction. It must be noted that the last term in the equation 4 is the mean free path of the softer phase that is matrix in this case. Kumari et al. (2017) have also correlated both yield and ultimate tensile strength with W content in the matrix (Fig. 9). Thus, the matrix composition is an important parameter that influences tensile properties of the heavy alloy.

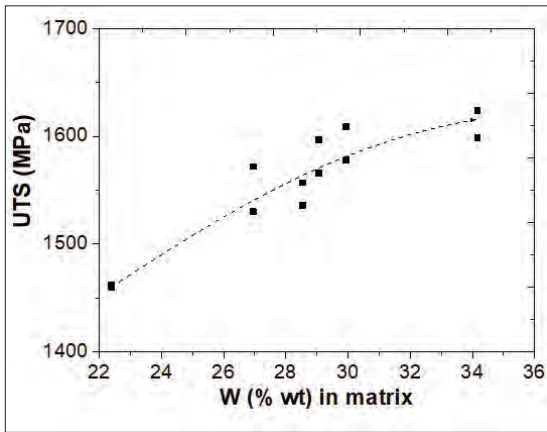


Fig. 9: Tensile Strength of a tungsten heavy alloy as a function of W (Kumari et al. 2017)

% elongation to failure that is ductility of tungsten heavy alloys is critically dependent on the fraction of W - W contact that is quantified as contiguity. As contiguity increases, % elongation comes down. This is since as the contiguity increases, W - W contact area increases and W - W contact area being relatively weaker acts as potential crack nucleation sites leading to early failure. % elongation is also dependent on the volume fraction of the matrix that in turn mainly depends on the W content. A combined contiguity-matrix volume fraction can describe the ductility trends in heavy alloys. (Fig. 10) (Ravi Kiran et al. 2017). This holds true

for impact toughness also. Being a PM alloy, the alloys exhibit substantial scatter in mechanical properties especially impact toughness (Fig. 11) that is one of the primary requirements for penetrator applications. This may be addressed by fine tuning thermomechanical parameters so as to obtain fine microstructure with reduced contiguity.

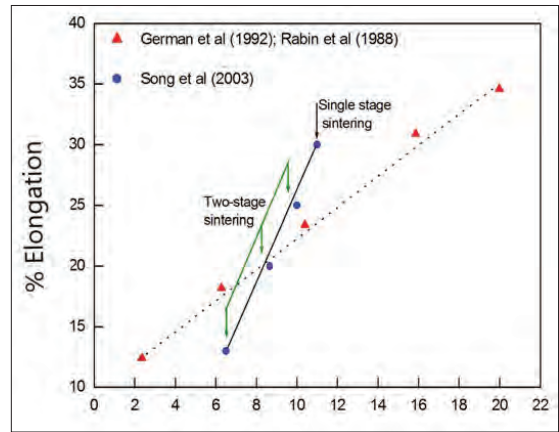


Fig. 10: Elongation to failure as a function of contiguity and matrix volume fraction (Ravi Kiran et al. 2017).

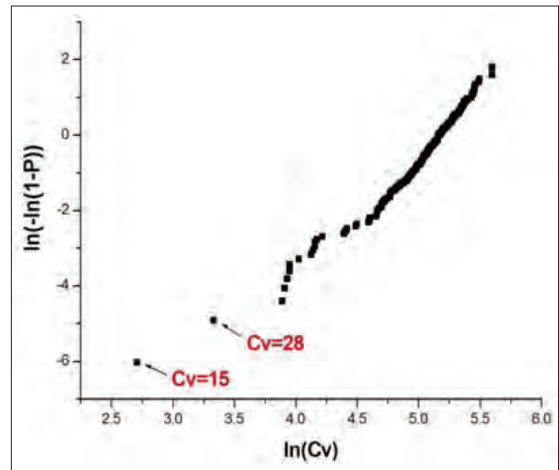


Fig. 11: Scatter in Impact property, Weibull plot of impact toughness. Notice very low values on the left side of the plot.

TUNGSTEN HEAVY ALLOYS: PROCESSING, MICROSTRUCTURE AND MECHANICAL BEHAVIOR

As regards composition, Co containing alloys show superior properties (Curry et al. 2013) as compared to those without Co (Fig. 12). The reasons are two fold: (1) Co increases the solubility of W in the matrix (2) it decreases contiguity in the microstructure. Figure 12 shows a clear example where Co containing alloys exhibit superior balance of strength and impact. In fact, W-Ni-Co alloys without Fe have shown excellent combinations of strength and impact toughness that is important for kinetic energy penetrator applications. These are due to different factors (1) increased W solubility in the matrix phase, (2) presence of fine W particles in the matrix and (3) refined W particles.

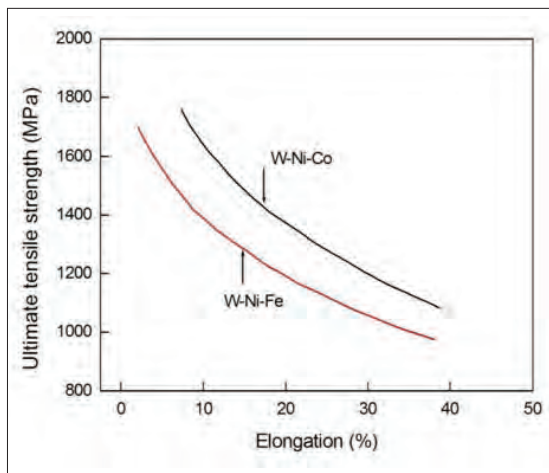


Fig. 12: Strength-ductility balance in W-Ni-Fe and W-Ni-Co (Stuitje et al. 1995)

5. Recent advancements

Attempts towards enhancement of mechanical properties of tungsten heavy alloys is a continuous process since armor systems protecting the tanks are evolving steadily providing enhanced protection. The projectiles made using heavy alloys need to be longer and they should be fired

with greater acceleration that in turn demands superior properties to withstand relatively higher stresses encountered during firing. One useful approach towards realizing this objective would be to engineer the microstructure that is realization of microstructures with fine W grains (1-2 μm) and substantially reduced contiguity (Mahot et al. 1988). Initial attempts in this direction are very promising. Significantly improved balance of mechanical properties has been achieved. However, issues related to scaled up production need to be addressed.

Additionally, while attaining enhanced quasi static properties, there are simultaneous efforts to realize better ballistic properties in order to obtain higher depth of penetration. In recent times, W-Bulk metallic glass composites (Dowding et al. 2004) have attracted attention primarily because of superior ballistic properties. While the work is in its infancy, the challenge could be to scale the process and also obtain long rods with enhanced quasi static properties, comparable to those of heavy alloys.

6. Conclusions

Different aspects of physical metallurgy of heavy alloys have been elucidated with an emphasis on alloy development for penetrator applications. Amidst a continuously evolving landscape in the field of tank protection, there has been an extensive R&D on tungsten heavy alloys that face significant challenges to provide viable solution as effective weapons for the destruction of main battle tanks and this needs innovative research efforts as other promising materials such as bulk metallic glass continue to emerge.

Acknowledgments

Authors are grateful to Director DMRL for his permission to publish this manuscript

TUNGSTEN HEAVY ALLOYS: PROCESSING, MICROSTRUCTURE AND MECHANICAL BEHAVIOR

References

1. Bhattacharjee A, Ghosal P, Gogia AK, Bhargawa S, Kamat SV, MSE A, 452-453, 2007, p. 219.
2. Bose A., Randall GM, Sims DM, US Patent no. 4801330, 1989
3. Cai W D, Li Y, Dowding RJ, Mohamed FA, Lavernia EJ, Rev. Part. Mater. 1995; 3:71-132.
4. Cury, R., Issartel, F., Joubert, J. M., Couque, H., 2013. Powder Metallurgy. 56, 347-350.
5. Das J, Appa Rao G, Pabi SK, Sankaranarayan M, Nandy TK, MSE A, 613, 2014, p. 48.
6. De Rossett W S, AFRL-TR-2395, 2001
7. Dowding RJ, Cho KC, Drysdale WH, Kecskes LJ, Minnicino MA, Staker MR, The Amptiac Quarterly, 8, 2004, p.71
8. Edmonds DV, Jones PN, Metallurgical Transactions A 1979; 10A:p. 289-293
9. Eliasson A., Ekbohm L., Fredrikson H., Powder Metallurgy, 2008, p. 343
10. German RM, Bose A, Mani SS, Metallurgical and Materials Transaction A, 23 (1992), p. 211
11. Hong SH, Ryu HJ, MSE A, 344, 2003, p. 253
12. Katavic´ B, Odanovic Z, 2005; 48 (3): 288-294.
13. Kemp PB, German PB, Metallurgical and Materials Transaction A, 26 (1995), p. 2187.
14. Kumari A, Sanakaranarayan M, Nandy TK, IJRMHM, 67, 2017, p. 18
15. Lanz W, Odermatt W, Weiraunch G., 19th international Symposium on Ballistics, Interlaken, Switzerland, 2001
16. Mahot P, Nicholas G, Voltz M., US Patent No.4762559, 1988:1-13
17. Nicolas G, US Patent 4960563, 1990
18. Noh JW, Kim EP, Song HS, Baek WH, Churn KS, Kang SJ, Metallurgical Transactions A. 1993; 24 A: 2411-2416
19. Panchal A, Venugopal Reddy K, Azeem PA, Nandy TK and Singh AK Philosophical Magazine (Taylor & Francis), 2020, DOI: <https://doi.org/10.1080/14786435.2020.1831704>
20. Rabin BH and German RM, Metallurgical and Materials Transaction A, 19 (1988), p. 1523
21. Ravi Kiran U, Kumar J, Kumar V, Sankarnarayan M, Nageswara Rao GVS, Nandy TK, MSE A, 656 (2016), p. 256.
22. Ravi Kiran U, Panchal A, Prem Kumar M, Sankarnarayan M, Nageswara Rao GVS, Nandy TK, MSE A, 640 (2015), p. 82
23. Ravi Kiran U, Panchal A, Prem Kumar M, Sankarnarayan M, Nageswara Rao GVS, Nandy TK, Journal of Alloys and compounds, 709, 2017, p. 609
24. Ravi Kiran U., Sambasiva Rao A, Sankaranarayana S, Nandy TK, IJRMHM, 33, 2012, p. 113
25. Ryu HJ, Hong SH, Baek WH, MSE A291, 2000, p. 91
26. Sahin Y, Journal of Powder Technology, Article ID 764306, Hindawi, 2014
27. Song SH, Ryu HJ, MSE A, 344 (2003), p. 253
28. Stuitje P, Harkema R, Taal C, US Patent, 1995, 5462576
29. Upadhyaya A, Materials Chemistry and Physics, 67, 2001, p.101
30. Y. Venkateswara Rao, G. Prabhu, M. Sankaranarayana and T.K. Nandy, "Development of a W-Ni-Co Alloy with Two Phase Matrix and Preliminary Property Evaluation -Part-I" DMRL technical report, 2015, DRDO-DMRL-PMG-108-2015
31. Yang Y, Lianxi H, Erde W, MSEA, 435(2006), p. 620
32. Yang SC, Mani SS, German RM, JOM, April, 1990, p. 16

EFFECT OF ALUMINA CONTENT ON THE PHASE DEVELOPMENT AND MECHANICAL PROPERTIES OF ALUMINA-MULLITE COMPOSITE SYNTHESIZED FROM ALLUVIAL CLAY OF THE GANGES

Arpan Kool^{a*}, Runumi Seal^b, Somtirtha Kool Banerjee^{c#}, Sukhen Das^{b*}

^aDepartment of physics, Vidyanagar College, West Bengal, India.

^bDepartment of Physics, Jadavpur University, Kolkata, India.

^cDepartment of microbiology, Lady Brabourne College, Kolkata, India.

* Email id of corresponding author: akphysics89@gmail.com

Abstract: High dense mullite-alumina composites with suitable mechanical properties have been developed using chemical alumina source and the Indian Ganges clay as the source of silica. The use of the clay from bed of the Ganges not only make the synthesis process of the composite economically favourable but also ensures the large-scale production and extensive applications of the same. In the composite, the total alumina content was varied from 72 to 78 mass percentage and the precursors of the alumina-mullite composite is sintered at 1400°C to ensure the crystalline phase formation of the composite. The developed phases have been investigated using XRD (X-ray diffraction) and characteristic reflections of α -mullite and crystalline alumina phases in the diffraction spectra confirms the formation of alumina-mullite composite. The Fourier transform infrared (FTIR) spectra of the composite showed the reflections corresponding to stretching vibrations of aluminium-oxygen, silicon-oxygen and aluminium-oxygen-silicon which confirms the formation of bonds between the constituent chemical elements. In the field effect scanning electron micrographs (FESEM), the elongated rods and equiaxed grains of mullite in addition to the alumina platelets are clearly visible and the length of the embedded mullite rods have length of $\sim 3\mu\text{m}$ and the grains of mullite and platelets of alumina have diameter in the nanometer range. The density of the alumina-mullite composite pellets as measured by well-known Archimedes' principle has arrived at $\sim 83\%$ for 78 mass% of alumina in the composite. The highest Vickers hardness and Knoop hardness of the composite are 3.98 and 4.12 GPa respectively for the highest alumina content. Thus, the mullite-alumina composite derived from the Ganges clay with decent densification and mechanical properties not only make the production cost of the ceramic composite lower but also seek good structural applications.

Keywords: Mullite; Composite; Hardness; Ceramic; Clay

1. Introduction

Mullite is an aluminosilicate having diverse functional and structural applications as it possess combination of unique engineering properties like stability at high temperature [1-2], high mechanical strength and creep resistance [3-4], high thermal resistance with low coefficient of thermal expansion [5-6], low dielectric constant etc. [7-8] The general formula of mullite is $\text{Al}_{4+2x}\text{Si}_{2-2x}\text{O}_{10-x}\Theta_x$ where Θ indicates oxygen vacancy and x generally takes

value between 0.18 and 0.88. Among these wide varieties of molar ratio between alumina and silica, the thermodynamically stable mullite have alumina to silica mole ratio fixed at 1.5 with x taking value 0.25 [9-11]. The physicochemical characteristics of the mullite have a strong relation not only with the choice of precursors but also the method of synthesis involved [12-13]. There are many reports regarding the development of pure mullite like sintering of silica and alumina powder mixture [14-16], sol-

EFFECT OF ALUMINA CONTENT ON THE PHASE DEVELOPMENT AND MECHANICAL PROPERTIES OF ALUMINA-MULLITE COMPOSITE SYNTHESIZED FROM ALLUVIAL CLAY OF THE GANGES

gel technique [17-18], spray pyrolysis technique [19-20], hydrothermal route [21], spark plasma sintering [22], molten salt synthesis method [23-24] etc.

However, the technology of processing and expensive starting material hinder the possibility of the large scale production of mullite. For this reason, clay still remains as a cheaper alternative resource to produce mullite after sintering at high temperature. Many natural clays containing minerals like kaolinite [25-26], pyrophyllite [27], silimanite [28], kyanite [29], bentonite [30] etc. were reported to transform into mullite phases after high temperature thermal treatment and numerous natural resources of silica like rice husk silica, slate rock silica were utilised to develop mullite and mullite composites upon addition of necessary external alumina with desired physicochemical properties [31-33].

On the other hand, materials which contain two crystalline phases may possess better mechanical properties and hence alumina-mullite ceramic composite positively influence the ceramic properties when the alumina content in the composite falls below 98%. Increasing alumina content creates more oxygen vacancies in the structure of mullite for maintaining charge neutrality which in turn improves the dielectric, mechanical and optical properties of mullite. Thus, silicon deficient alumina-mullite composite results in a good mechanical strength [34].

In this paper, we have prepared precursor of alumina-mullite composites using natural Ganges clay as the primary source of silica. The clay was collected from the state of West Bengal of India. The effect of the alumina content on the physico-chemical and mechanical properties of the composite is studied thoroughly. The composite shows decent physicochemical

characteristics along with good mechanical behaviour.

2. Experimentals

2.1. Materials

The clay was collected from the bed of the Ganges near Budge Budge area of the district of 24 Parganas (South) of West Bengal, India. It was washed several times with millipore water before use as the silica source of the alumina-mullite composite. Aluminium iso-propoxide (AIP) (C₉H₂₁O₃Al) (Loba Chemie) was utilised as the source of alumina.

2.2. Preparation of the mullite-alumina composites

The mullite-alumina composites with different contents of alumina were synthesized using alluvial soil of the Ganges as the primary source of silica. The clay was washed with deionized water and then treated with 3% H₂O₂ for the removal of organic impurities. The clay contains 63.7 mass% of silica and 14.59 mass% of alumina. In addition to silica and alumina the clay also consists of other oxides like Fe₂O₃, MnO, TiO₂, Cao, MgO, Na₂O, K₂O, P₂O₅ etc to lesser extent. In order to prepare the precursors of the composite, required amount of aluminium isopropoxide was first put into the 100 cc of deionized water and vigorously mixed magnetically till its complete dispersion in water. Amounts of aluminium isopropoxide is such adjusted that the total mass percentage of alumina in the composite become 72% (72AMAS), 74% (74AMAS), 76% (76AMAS) and 78% (78AMAS). The chemically treated clay was thereafter mixed the aluminium isopropoxide solution and the mixture was stirred for 72 hours to achieve homogeneous mixing. After complete dispersion of AIP and clay, the mixtures were dried in an air oven at 80°C and the dried precursors were ground to form fine powders and circular pellets prepared for mechanical strength and

EFFECT OF ALUMINA CONTENT ON THE PHASE DEVELOPMENT AND MECHANICAL PROPERTIES OF ALUMINA-MULLITE COMPOSITE SYNTHESIZED FROM ALLUVIAL CLAY OF THE GANGES

density measurement. The composite precursors and pellets were sintered at 1400°C under air atmosphere in a high temperature furnace in order to ensure mullitization. The rate of heating was fixed at 50°C per hour upto 500°C and the heating rate was maintained at 100°C per hour for the rest followed by soaking for 5 hours. The synthesis procedure is summarized in the Fig. 1.

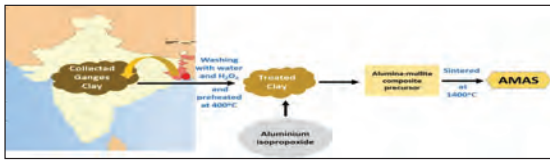


Fig. 1: Schematic of synthesis procedure of alumina-mullite composite

The mass percentages and mole ratio of alumina and silica for different samples have been given in the Table 1.

Table 1: Alumina-mullite composite sample description

Name of the sample	Mass % of alumina	Mass % of silica	Mole ratio of alumina and silica
72 AMAS	72	28	1.5
74 AMAS	74	26	1.7
76 AMAS	76	24	1.9
78 AMAS	78	22	2.1

2.3. Characterisations

The Formation of phases and crystallization behaviour of the alumina-mullite composites with different alumina content were investigated by X-ray diffractometer (Bruker, Madison, Wisconsin) (XRD) and Fourier transform infrared spectrometer (FTIR) (Shimadzu) (8400S). In X-ray diffraction, CuK α radiation of 1.54 Å wavelength with range of 2 θ = 10°–70° at a scan speed of 0.3 sec per step. The increment, working voltage, and working current were fixed 0.02, 40 kV and 40 mA respectively during the diffraction experiment. The comparative FTIR spectroscopic studies of alumina-mullite composite were performed by the potassium bromide pellet

method in the range of wavenumbers 400 cm⁻¹ to 1200 cm⁻¹. Microstructures of the composite were analysed using the FESEM (Field effect scanning electron microscopy, INSPECT F50 model, Netherland) images.

The apparent porosity and density of the pellets of the composites were carried out using Archimedes' principle ($\rho = m/v$). The sample pellets were soaked in Xylene under vacuum and then the following formula is to calculate the bulk density of the samples.

$$\text{Bulk Density } (\rho) = \frac{\text{weight in air } (W_{air})}{\text{Soaked weight } (W_{soaked}) - \text{Suspended weight } (W_{suspended})} \times \text{density of Xylene } (0.86 \text{ g/cc})$$

The hardness (Vickers and Knoop) of the alumina-mullite composites were measured indenting on polished sample pellets using the hardness tester of 'Leco' containing nanoindenter (Leco, LV700). For the measurement of Vickers hardness, the used indenter has a shape of pyramid having square base with angle of 136° between two opposite edges while for Knoop hardness measurement the used indenter has a pyramid shape with lozenge base having the angle between one pair of opposite faces as 172°5' and between the other opposite pair fixed at 130°. The hardness values are measured using the 3 kgf indentation load on the surface of the samples for 10 s to minimize effect of indenter size. The hardness numbers (denoted by Hv and HK for Vickers and Knoop hardness respectively) of the samples are calculated using the following equations:

$$H_V = \frac{P}{A_{TAC}} = \frac{P}{\frac{d^2}{2} \sin \frac{\psi}{2}} = 1.8544 \frac{P}{d^2} \dots \dots (1)$$

$$H_K = \frac{P}{A_{PAC}} = \frac{P}{L^2 \frac{\tan \phi / 2}{2 \tan \theta / 2}} = 14.299 \frac{P}{L^2} \dots \dots (2)$$

Where P, d and L denote the applied load (in Newton unit), indentation diagonal in case of Vickers hardness (in mm unit) and diagonal of longer indentation by Knoop indenter (in mm unit). Here, APAC and ATAC denote projected

EFFECT OF ALUMINA CONTENT ON THE PHASE DEVELOPMENT AND MECHANICAL PROPERTIES OF ALUMINA-MULLITE COMPOSITE SYNTHESIZED FROM ALLUVIAL CLAY OF THE GANGES

area of contact and the true area of contact regarding Knoop and Vickers indentations respectively [35-36].

3. Results and discussions

3.1. XRD analysis:

The corelative XRD patterns of the alumina-mullite composites containing 72-78% of alumina by mass is shown in Fig. 2. Characteristic reflections of high crystalline alumina and mullite phases were visible in powder X-ray diffraction spectra which is indicative of formation of the composite. In case of higher mass percentage of alumina, the crystalline peaks of alumina became more prominent as crystallization of excess alumina occurs from the external aluminium isopropoxide (AIP). In addition, orthorhombic mullite formation after sintering of the composite precursor at 1400°C was confirmed from the splitting of the characteristic peak of mullite at $2\theta=26^\circ$. The silica from the clay source melts at higher temperature to form the viscous phases into which the alumina diffuses to form the mullite phases followed by nucleation and growth of mullite crystals. Here, the rate of growth is determined by means of Al_2O_3 dissolution rate into the viscous SiO_2 formed at higher temperature. During high temperature sintering process mullite will start to grow at the interface of alumina and silica and the unreacted alumina crystallizes to develop crystalline alumina phases and that increases with higher mass percentage of alumina.

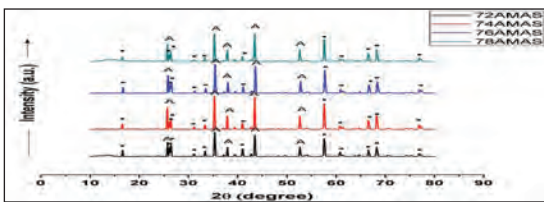


Fig. 2: Comparative XRD pattern of alumina-mullite composites (■ indicates mullite phases and ▲ indicates crystalline alumina phase)

The average crystallite diameter for both alumina and mullite phases are calculated and given in Table 2 according to the Scherrer's equation: $\delta=0.9\lambda^1/\beta\cos\theta$ where δ is average diameter of crystallite, λ^1 is wavelength of the Cu-K α radiation, β is FWHM (Full width of half maximum) in radian [37]. The crystallite size for both mullite and alumina is observed to increase to 74 mass% of alumina from 72 mass percentage which in turn affect the mechanical properties of the composite.

Table 2: Crystallite size for mullite and crystalline alumina as calculated from Debye-Scherrer's equation

Name of the sample	Average crystallite size for mullite (nm)	Average crystallite size for alumina (nm)
72AMAS	42	36
74AMAS	44	38
76AMAS	40	37
78AMAS	38	36

3.2. FTIR analysis

The comparative (FTIR spectra of the alumina-mullite composites (with varying mass percentages of alumina) sintered at 1400oC are given in Fig. 3.

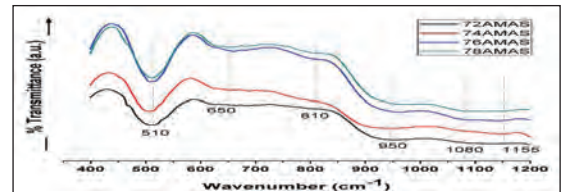


Fig. 3: Comparative FTIR spectra of alumina-mullite composites

The characteristic bands corresponding to both mullite and alumina were found in the FTIR spectra at 510, 650, 810, 950, 1080, 1155 cm^{-1} which were associated to stretching of Al-O bonds, octahedral stretching mode of AlO_6 , Si-O-Al vibrational mode, Si-O stretching, Al-O-Si bond vibration and vibrations of Si-O stretching respectively. The presence of these characteristic bands clearly indicates the formation of mullite. Appearance of 510 cm^{-1} band which corresponds to Al-O stretching vibrational modes indicates

EFFECT OF ALUMINA CONTENT ON THE PHASE DEVELOPMENT AND MECHANICAL PROPERTIES OF ALUMINA-MULLITE COMPOSITE SYNTHESIZED FROM ALLUVIAL CLAY OF THE GANGES

the presence of alumina. The brief description of the FTIR peaks was given in Table 3.

Table 3: Designation of vibrations reflected in FTIR Spectra

Peak positions (cm ⁻¹)	Assignment of peaks
510	Al-O stretching mode
650	AlO ₆ octahedral stretching mode
810	Si-O-Al vibrational band
950	Si-O stretching vibration
1080	Al-O-Si vibrational band
1155	Si-O stretching vibration

3.3. FESEM analysis:

The FESEM micrographs of alumina mullite composites with different mass percentages of alumina are given in Fig. 4 (a-d). Mullite whiskers along with equiaxed grains of mullite were observed in the microstructure of the composite. Alumina platelets were found to grow as the content of alumina in the composite increases. All the microstructures (Figs. 4 a-d) show well grown mullite and alumina crystalline phases which confirms the formation of the composite. Needles of mullite are 3µm long and 500 nm on an average whereas average diameter of the alumina platelets is 600-800 nm. The thickening of the grains is observed for 74AMAS which is also the trend for crystallite size as calculated using Debye Scherrer’s equation from X-ray diffraction pattern. Moreover, the well densification behaviour of the composite can also be prescribed from the FESEM micrographs.

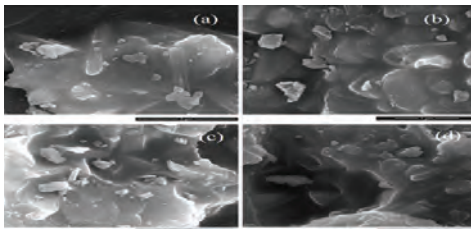


Fig. 4: The FESEM images of mullite-alumina composite with mass percentages of alumina within the composite as (a) 72%; (b) 74%; (c) 76% and (d) 78%.

3.4. Densification and Linear shrinkage:

The relative density ((Measured bulk density/ Theoretical density) × 100%) along with apparent porosity (100-relative density) of the alumina-mullite composite pellets with different alumina content were calculated by taking the theoretic density of mullite as 3.16 g/cc and linear shrinkage was determined by measuring the diameters and thickness using a micrometer screw gauge. (Table 4).

Linear shrinkages of the sample pellets (LS1 and LS2) were calculated using the formulae:

$$LS1 = \frac{(d_0 - d_1)}{d_0} \times 100\%$$

$$LS2 = \frac{(t_0 - t_1)}{t_0} \times 100\%$$

where, d₀, d₁ correspond to the diameter of the pellets before and after sintering respectively and t₀, t₁ correspond to the thickness of the pellets before and after sintering respectively [38].

Table 4: Values of Relative Density, Apparent Porosity and Linear Shrinkages (LS1 & LS2) from measurements of dimensions of sample pellets:

Sample name	Relative density (%)	Apparent Porosity (%)	Linear Shrinkage, LS1 (%)	Linear Shrinkage, LS2 (%)
72 AMAS	73.41	26.59	14.42	19.97
74 AMAS	75.95	24.05	16.79	22.04
76 AMAS	78.48	21.52	16.86	22.19
78 AMAS	82.91	17.09	16.98	22.52

Physical properties of composites are enlisted in Table 3 and physical texture of all the composite pellets before and after sintering is shown in the Fig. 5. Both the relative density and linear shrinkage increase as the percentage of alumina content increases in the composite which is evident not only from the calculated data but also visible in Fig. 5. Moreover, shrinkages are uniform in the directions along both the thickness and diameter for every samples.

EFFECT OF ALUMINA CONTENT ON THE PHASE DEVELOPMENT AND MECHANICAL PROPERTIES OF ALUMINA-MULLITE COMPOSITE SYNTHESIZED FROM ALLUVIAL CLAY OF THE GANGES

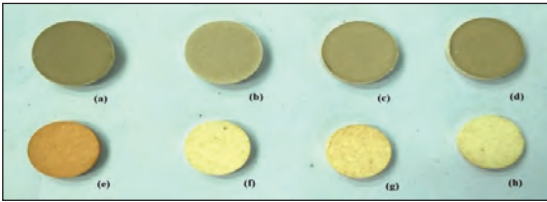


Fig. 5: Physical texture of the alumina-mullite composite pellets before & after sintering at 1400°C. Pellets of (a) 72 AMAS, (b) 74AMAS, (c) 76AMAS and (d) 78AMAS before sintering and pellets of (e) 72 AMAS, (f) 74AMAS, (g) 76AMAS and (h) 78AMAS after sintering at 1400°C.

The graph showing the change of apparent porosity and relative density of the composite with increasing alumina content is shown in Fig. 6.

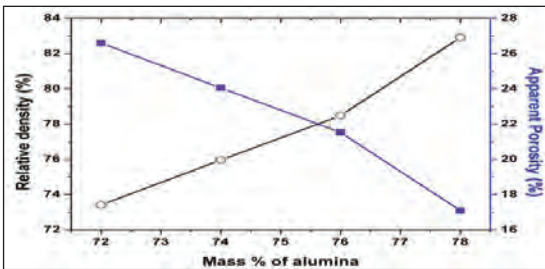


Fig. 6: Variation of Relative Density and Apparent porosity for 72AMAS, 74AMAS, 76AMAS and 78AMAS

The relative density was found to increase associated with decrease of apparent porosity for increasing alumina content. Almost 83 % bulk density of the composite relative to that of pure mullite was observed at highest alumina content in the composite because of interstitial alumina grains between mullite crystals. The interstitial alumina platelets formation and presence non-uniform equiaxed grains of mullite in between whiskers as obtained in scanning electron micrographs are primarily responsible for the highly compact nature. Increased linear shrinkage of the composite with higher alumina content ensures the increased crystallinity in the composite.

3.5. Hardness and Mechanical Properties:

The Hardness (Vickers and Knoop) of the samples are calculated using the equation (1) and (2) and the values are given in Table 5. The Young’s modulus (Y) of the composites are also included in the Table 4 which are measured according to the formula:

$$\left(\frac{b'}{a'}\right)_{measured} = 0.1406 - 0.5 \left[\frac{HK}{Y}\right]$$

where b’ and a’ indicates the length of minor and major diagonals respectively for Knoop indentation.

Table 5: Hardness measurement data

Mass% of alumina	F (kgf)	b’ (µm)	a’ (µm)	b’/a’	HV (GPa)	HK (GPa)	(HK) _{TAC} (GPa)	HV/(HK) _{TAC}	Y (GPa)
72	3	39.1	345.2	0.113	3.4	3.5	3.2	1.08682	74.3
74	3	43.3	351.2	0.123	3.3	3.4	3.1	1.08618	71.9
76	3	48.1	319.5	0.150	3.7	3.8	3.4	1.08049	81.8
78	3	54.5	332.1	0.164	3.9	4.1	3.7	1.07177	90.9

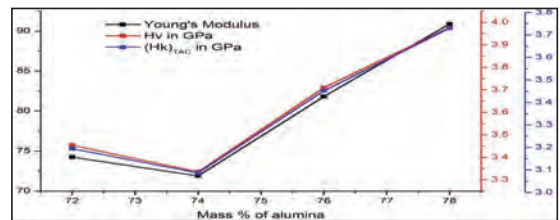


Fig. 7: Variation of Vickers hardness, Knoop hardness and Young’s modulus of mullite-alumina composite with respect to the content of alumina in the composite

The change of Vickers hardness, Knoop hardness and Young’s modulus with respect to the mass% of alumina in the composite is shown together in Fig. 7. A drop in the hardness value as well as Young’s modulus is observed for 74% alumina after 72% alumina content and then again all the values increase with further increase in alumina content. This occurs due to a little increase in the grain size for 74% alumina content in the composite as obtained from the Debye-Scherrer’s equation and FEEM micrographs. As grain

EFFECT OF ALUMINA CONTENT ON THE PHASE DEVELOPMENT AND MECHANICAL PROPERTIES OF ALUMINA-MULLITE COMPOSITE SYNTHESIZED FROM ALLUVIAL CLAY OF THE GANGES

size increases it is easier for the dislocations to propagate through the grain boundaries under the external stress which in turn results in a lower strength of the composite according to Hall-Petch effect.

In general, the Vickers hardness number is higher than Knoop hardness number when the value of hardness is comparatively high. However, this behaviour reverses when the hardness values are lower than a particular value (~7.9 GPa). Hardness is known to be a contact-area-related parameter. As soon as the indentation load is withdrawn, elastic recovery occurs in the material because of plastic zone mismatch between the zone just under the impression indentation and the surrounding region. Thus, distinct difference arises between the true contact area which formed during indentation and the apparent area of contact measured after the indenter is removed. Generally the elastic recoveries after unloading Vickers and Knoop indenters from the surface of the sample are different. In case of Vickers hardness measurement, the elastic recoveries of the samples occur in the direction of indentation depth with the length of indentation diagonal remaining almost unchanged. However, removal of Knoop indenter from the surface often leads to a decrease of the minor diagonal length due to elastic recovery. Hence, a difference in the measured values of Vickers and Knoop Hardness remains because of dissimilarity between the type and extent of elastic recoveries in both the cases. The ratio of the minor diagonal length to the major diagonal length (b^*/a^*) in case of Knoop indentation is a measure of elastic recovery of the composite. When no post-indentation elastic recovery occurs, b^*/a^* takes a value of 0.1406. The relation between b^*/a^* and the ratio of two hardness numbers were correctly given by Chicot et al. for all range of hardness. They approached with the measurement of true area of contact (TAC) during indentation and obtained the Knoop

hardness number with true area of contact ($(H_k)_{TAC}$) by multiplying the traditional Knoop hardness number by 0.9047. The equation given by Chicot et al. [36] is as follows:

$$\left(\frac{b^*}{a^*}\right)_{measured} = 0.1908 - 0.0658 \left[\frac{H_V}{(H_k)_{TAC}} \right] \text{ Where } (H_k)_{TAC} = 0.9047 H_K$$

The measured Vickers and Knoop hardness values may only be the same if there is zero elastic recovery after withdrawal of indenter. So difference in hardness values as observed in table 4 is indicative of elastic recovery of the material after the indentation load is withdrawn. As observed from the results, it was obvious that with increasing alumina content in the composite, the ratio of minor and major diagonals of the indentation after the indenter being removed is increasing as $\frac{H_V}{(H_k)_{TAC}}$ decreases (Fig. 8).

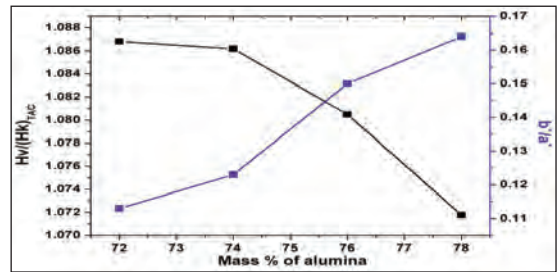


Fig. 8: Variation of $\frac{H_V}{(H_k)_{TAC}}$ and b^*/a^* with mass% of alumina in the mullite-alumina composite

This indicates that the elastic recovery of high alumina composite is lower than that of low alumina composite which can be attributed to the crystal mismatch between crystalline alumina and mullite phases resulting in lower elastic behavior of the composite.

Conclusions

In summary, we have successfully prepared alumina-mullite composites using natural Ganges clay as silica source and chemical precursor of alumina with alumina content

EFFECT OF ALUMINA CONTENT ON THE PHASE DEVELOPMENT AND MECHANICAL PROPERTIES OF ALUMINA-MULLITE COMPOSITE SYNTHESIZED FROM ALLUVIAL CLAY OF THE GANGES

in the composite being varied from 72 to 74 mass%. Reflections of mullite phases along with the reflections of crystalline alumina in X-ray diffraction pattern and characteristic bond vibrations present in FTIR spectra confirms the successful preparation of the composite. The relative density attained a value of ~83% for 78 mass% alumina in the composite due to the higher interstitial formation of crystalline alumina between mullite grains. The Vickers and Knoop Hardness along with Young's modulus for 74% alumina fell below those for 72 mass% alumina due to the increase in grain size which results in lower resistance to the dislocation motion. However, their values increased with further increase in alumina content reaching at the values of 3.9, 3.7 and 90.9 GPa respectively for 78% alumina. Thus, the alumina-mullite composite prepared using natural source of clays from the Ganges bed seek its broader applications due to its lower production cost and decent mechanical properties.

Acknowledgements

The authors sincerely acknowledge DST (Department of science and technology) under Government of India for their financial assistance. We are also thankful to Mr. S. Mondal for collection of the clay from the Ganges bed.

References

- [1] Torrecillas R, Calderon JM, Moya JS, Reece MJ, Davies CKL, Olagnond C, Fantozzi G. Suitability of mullite for high temperature applications. *J Eur Ceram Soc* 1999;19:2519-27.
- [2] Schneider H, Schreuer J, Hildmann B. Structure and properties of mullite-A review. *J Eur Ceram Soc* 2008;28:329-44.
- [3] Ohira H, Ismail MGMU, Yamamoto Y, Akiba T, Somiya S. Mechanical properties of high purity mullite at elevated temperatures. *J Eur Ceram Soc*. 1996;16:225-29.
- [4] Okamoto Y, Fukudome H, Hayashi K, Nishikawa T. Creep deformation of polycrystalline mullite. *J Eur Ceram Soc* 1990;6:161-8.
- [5] Schneider H. Thermal Expansion of Mullite. *J Am Ceram Soc* 1990;73:2073-6.
- [6] Hildmann B, Schneider H. Thermal Conductivity of 2/1-Mullite Single Crystals. *J Am Ceram Soc*. 2005;88:2879-82.
- [7] Giess EA, Roldan JM, Bailey PJ, Goo E. Microstructure and Dielectric Properties of Mullite Ceramics. In: Nair KM, Pohanka RC, Buchanan RC, editors. *Ceramic Transactions, Vol 15, Microelectronic Systems*; Westerville, OH: American Ceramic Society; 1990, p. 167-72.
- [8] da Silva VJ, de Almeida EP, Gonçalves WP, da Nóbregab RB, de Araújo Neves G, de Lucena Liraa H, Menezesa RR, de Lima Santana LN. Mineralogical and dielectric properties of mullite and cordierite ceramics produced using wastes. *Ceram Int*. 2018;11:161-8.
- [9] Angel RJ, Prewitt CT. Crystal Structure of Mullite: A Re-examination of the Average Structure. *Am Mineral* 1986;71:1476-82.
- [10] Aksay IA, Dabbs DM, Sarikaya M. Mullite for Structural, Electronic, and Optical Applications. *J Am Ceram Soc*. 1991;74:2343-58.
- [11] Ruscher CH, Schrader G, Gotte M. Infra-red Spectroscopic Investigation in the Mullite Field of Composition: $Al_2(Al_{2+2x}Si_{2-2x})O_{10-x}$ with $0.55 > x > 0.25$. *J Eur Ceram Soc*. 1996;16:169-75.
- [12] Bagchi B, Das S, Bhattacharya A, Basu R, Nandy P. Nanocrystalline Mullite Synthesis at a Low Temperature: Effect of Copper Ions. *J Am Ceram Soc*. 2009;92:748-51.
- [13] Viswabaskaran V, Gnanam FD, Balasubramanian M. Mullite from clay-reactive alumina for insulating substrate application. *Appl Clay Sci*. 2004;25:29-35.
- [14] Kong LB, Zhang TS, Chen YZ, Ma J, Boey F, Huang H. Microstructural composite mullite derived from oxides via a high-energy ball milling process. *Ceram Int*. 2004;30:1313-7.
- [15] Kleebe H.-J, Siegelin F, Straubinger T, Ziegler

EFFECT OF ALUMINA CONTENT ON THE PHASE DEVELOPMENT AND MECHANICAL PROPERTIES OF ALUMINA-MULLITE COMPOSITE SYNTHESIZED FROM ALLUVIAL CLAY OF THE GANGES

- G. Conversion of Al_2O_3 - SiO_2 powder mixtures to 3:2 mullite following the stable or metastable phase diagram. *J Eur Ceram Soc.* 2001;21:2521-33.
- [16] Boch P, Chartier T, Rodrigo PDD. High-purity mullite ceramics by reaction-sintering. *Ceramic Trans.* 1990;6:353-74.
- [17] Kool A, Thakur P, Bagchi B, Hoque NA, Banerjee S, Das S. Sol-gel synthesis of transition-metal ion conjugated alumina-rich mullite nanocomposites with potential mechanical, dielectric and photoluminescence properties. *RSC Adv.* 2015;5:104299-313.
- [18] Cividanes LS, Campos TMB, Rodrigues LA, Brunelli DD, Thim GP. Review of mullite synthesis routes by sol-gel method. *J Sol-Gel Sci Technol.* 2010;55:111-25.
- [19] Kanzaki S, Tabata H, Kumazawa T. Sintering and mechanical properties of mullite derived via spray pyrolysis. *Ceramic Trans.* 1990;6:339-51.
- [20] Baranwal R, Villar MP, Garcia R, Laine RM. Flame Spray Pyrolysis of Precursors as Route to Nano-mullite Powder: Powder Characterization and Sintering Behavior. *J Am Ceram Soc.* 2001;84:951-61.
- [21] Komarneni S, Roy R, Breval E, Ollinen M, Suwa Y. Hydrothermal route to ultrafine powders utilizing single and di-phasic gels. *Adv Ceram Mater.* 1986;1:87-92.
- [22] Munir ZA, Anselmi-Tamburini U, Ohyanagi M. The effect of electric field and pressure on the synthesis and consolidation of materials: A review of the spark plasma sintering method. *J Mater Sci.* 2006;41:763-77.
- [23] Kool A, Thakur P, Bagchi B, Hoque NA, Banerjee S, Das S. Salt-melt synthesis of B_2O_3 , P_2O_5 and V_2O_5 modified high-alumina mullite nanocomposites with promising photoluminescence properties. *Mater Res Express.* 2017;10:105005.
- [24] Zhang P, Liu J, Du H, Li Z, Li S, Xu R. Molten salt synthesis of mullite whiskers from various alumina precursors. *J Alloys Compd.* 2010;491:447-51.
- [25] Bagchi B, Das S, Bhattacharya A, Basu R, Nandy, P. Mullite phase enhancement in Indian kaolins by addition of vanadium pentoxide. *Appl Clay Sci.* 2010;47:409-13.
- [26] Lee S, Kim YJ, Moon HS. Phase transformation sequence from kaolinite to mullite investigated by an energy filtering transmission electron microscope. *J Am Ceram Soc.* 1999;82:2841-8.
- [27] Sanchez-Soto PJ, Perez-Rodriguez JL. Formation of Mullite from Pyrophyllite by Mechanical and Thermal Treatments. *J Am Ceram Soc.* 1989;72:154-7.
- [28] Schneider H, Majdic A. Preliminary investigations on the kinetics of the high-temperature transformation of sillimanite to 3/2-mullite plus silica and comparison with the behaviour of andalusite and kyanite. *Sci Ceram.* 1981;11:191-6.
- [29] Schneider H, Majdic A. Kinetics of the thermal decomposition of kyanite. *Ceramurgia Int.* 1980;6:32-7.
- [30] Gomes J, Rocha AIO, Menezes RR, de Araujo Neves G, Brasileiro MI, de Lima Santana LN. Obtaining of Mullite by Rapid Sintering from Bentonite Clay. *Mater Sci Forum* 2010; 660-661:936-42.
- [31] Sembiring S, Simanjuntak W, Manurung P, Asmi D, Low IM. Synthesis and characterisation of gel-derived mullite precursors from rice husk silica. *Ceram Int.* 2014;40:7067-72.
- [32] Sembiring S, Simanjuntak W, X-ray diffraction phase analyses of mullite derived from rice husk silica. *Makara J Sci.* 2012;16:77-82.
- [33] Vieira SC, Ramos AS, Vieira MS. Mullitization kinetics from silica- and alumina rich wastes. *Ceram Int.* 2007;33:59-66.
- [34] Kool A, Thakur P, Bagchi B, Hoque NA, Das S. Mechanical, dielectric and photoluminescence properties of alumina-mullite composite derived from natural Ganges clay. *Appl Clay Sci.* 2015;114:349-58.
- [35] Gong J, Wang J, Guan ZA. Comparison between Knoop and Vickers hardness of silicon nitride ceramics. *Mater Lett.* 2002;56:941-4.

EFFECT OF ALUMINA CONTENT ON THE PHASE DEVELOPMENT AND MECHANICAL PROPERTIES OF ALUMINA-MULLITE COMPOSITE SYNTHESIZED FROM ALLUVIAL CLAY OF THE GANGES

- [36] Chicot D, Mercier D, Roudet F, Silva K, Staia MH, Lesage J. Comparison of instrumented Knoop and Vickers hardness measurements on various soft materials and hard ceramics. *J Eur Ceram Soc.* 2007;27:1905-11.
- [37] Kool A, Thakur P, Bagchi B, Sepay N, Das, S. Physico-chemical property-driven dielectric behaviour and catalytic activity of nanocrystalline mullite synthesized from monophasic precursor gel. *J Sol-gel Sci Technol.* 2016; DOI: 10.1007/s10971-016-4155-4
- [38] Wang Y, Liu H, Cheng H, Wang J. Densification behavior and microstructure of mullite obtained from diphasic Al_2O_3 - SiO_2 gels. *Ceram Int.* 2014;40:12789-96.

A REVIEW ON EVOLUTION, STABILITY, AND TRANSFORMATION OF PHASES IN HIGH ENTROPY ALLOYS (HEAs)

Manashi Sabat¹, Gourahari Behera¹, Manila Mallik^{1*}

¹Department of Metallurgical & Materials Engineering, VSSUT, Burla,
Sambalpur, Odisha, India.
me.manashi20@gmail.com

Abstract: Starting from the bronze age men have been trying to explore the properties of materials by mixing two or more elements and named them as alloy. But the never satisfied mind and unlimited desire of humans always leads towards new scientific inventions and discoveries. The high entropy (HEAs) are the outcome of such an invention, which is now a most encouraging and dynamic class of materials with many more explorations to come up. Unlike the conventional alloys, the HEAs are mixed in equiatomic or near equiatomic ratios of a minimum of five constituent elements, which provides many interesting and peculiar properties to these materials. Excellent stability at both high temperature and low temperature (cryogenic temperature), very good energy storing capacity, irradiation tolerance, and excellent corrosion resistance are some uniqueness of HEAs which is drawing most of the attention of material scientists. The foremost thing in getting the ideas about the characteristics properties of HEAs is understanding the phases and microstructures of this particular group of alloys because as learned from the material-tetrahedron, the importance of structure-properties correlation is well understood by material scientists. This review paper put forward some basics about the evolution, stability, and transformation of phases in HEAs.

Keywords: High entropy alloy: multi principal elements: sluggish diffusion: enthalpy of mixing: valence electron concentration.

1. Introduction

High entropy alloys (HEAs) are an emerging class of materials in today's world, which are basically multiprincipal elements having five or more elements in equiatomic proportion with some exceptional potential characteristics. Unlike conventional alloys, which generally have two base elements, the HEAs consist of many principal elements, which are the base for imparting high entropy value in these alloys. As in conventional alloys, one is a base element and the other one is a minor, the HEAs have many principal elements in equiatomic or near equiatomic proportions. The HEAs generally have a minimum of five elements with a 5 to 35 % of atomic ratio or molar ratio [1]. This method eliminates the base element concept of the conventional alloy system. The novel concepts engaged here are undiscovered domain

of alloy compositions and solid solution phase stability through regulation of configuration entropy of the system. Earlier, the main concern was at the corners of the phase diagrams to develop a conventional alloy, however, with the advancement of HEAs, the focus has been shifted to the central region, which provides the base for the advanced stability of HEAs, which is shown in the figure 1. There are many extraordinary applications of HEAs in the fields of engineering like nuclear power plants, cryogenic areas, energy storage areas, excellent corrosion resistant areas, etc. The presence of multiple numbers of base elements in equiatomic or near equiatomic proportion gives some exceptional properties to the HEAs, like high entropy, severe lattice distortion, sluggish diffusion, and cocktail effect to the alloy.

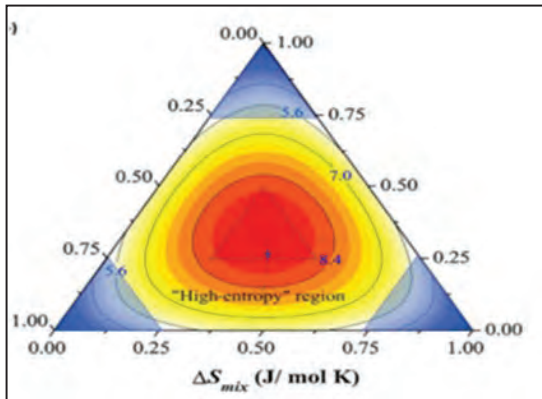


Fig.1. shows the configurational entropy value of a ternary system [2].

German metallurgist Franz Karl Achard is the first, to do research taking 5 or 7 elements in equal amounts and mixing them to form an alloy in the 18th century. Surprisingly he found many improved properties of this type of alloy than the conventional alloys. Then later on another scientist George Cantor and his co-workers worked on this concept and synthesized alloys by taking many elements in equiatomic proportion. He worked on 16 to 20 elements. The resulted alloys were generally multiphase and brittle. But interestingly Fe₂₀Cr₂₀Mn₂₀Ni₂₀Co₂₀ alloy was single-phase FCC and the number of phases formed were less than as proposed by Gibb's phase rule [1][3]. At the same time, the work on this type of alloy was also carried on by another scientist named Jien-Wei Yeh. According to him high solid solution stability and less number of phases formation in these alloys are due to the high configurational entropy of the system. Initially, these alloys were termed as multi principal element alloy by George Cantor, but Jien-Wei Yeh coined these alloys as High Entropy Alloys (HEAs). Later on, many of their exceptional and interesting characteristics attract many scientists to work with these alloys.

2. Understanding of High Entropy Alloys

2.1. Alloy: An alloy is a mixture of one base element with one minor element in a definite weight ratio, which may be a substitutional or interstitial solid solution depending upon the atomic arrangement of atoms. For example: brass, bronze, steel, etc.

2.2. High entropy alloy: These are the alloys where there is no base element and 5 or more than 5 principal elements are mixed in equiatomic or near equiatomic ratio giving rise to high configurational entropy value and hence the name high entropy alloys. Here each of the principal elements has a 5 to 35 % atomic weight percentage composition. When five elements with equiatomic proportion are mixed their configurational entropy value is raised to a large extent. When the ΔS_{mix} value is $\geq 1.5R$, this is known as high entropy alloy, where R is the universal gas constant and ΔS_{mix} is configurational entropy of mixing as suggested by Yeh et al [2] which is schematically represented in the figure 2.

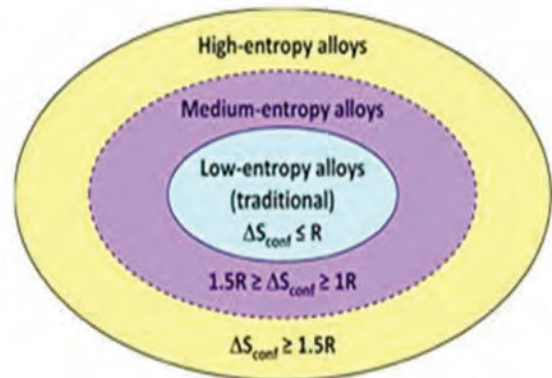


Fig.2. shows the considered entropy value for high entropy, medium entropy, and low entropy alloys [4].

The base element concept of conventional alloy has been discarded in the high entropy alloy where all the constituent elements are the base elements and present in equimolar or near equimolar proportion as shown in the figure 3.

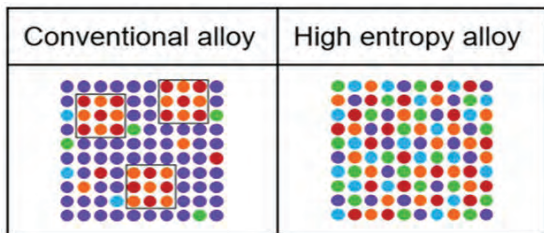


Fig.3. shows conventional alloy (left) and high entropy alloy (right)

3. Properties and Applications of HEAs

This newly evolving class of alloys has many attractive properties which draw the attention of researchers and scientists. Unlike the conventional alloys, where there is only one major element, do not provide much scope to alter properties by changing the compositions, whereas in the case of HEAs there are thousands of possible compositions and new properties that can be obtained by simply interchanging the composition of any of the elements or by adding a new or subtracting one from the existing one. The most eye-catching properties that the HEAs have are known as “the four core effects” [2][5]. They are described as:

- 3.1. High entropy
- 3.2. Severe lattice distortion
- 3.3. Sluggish diffusion
- 3.4. Cocktail effect

3.1. High Entropy: The presence of five or more elements in equiatomic proportion in the alloy system increases the entropy of configuration to a large extent; which consequently increases the stability of phases by decreasing the free energy

of the system. As we know, $\Delta G_{mix} = \Delta H_{mix} - T\Delta S_{mix}$ where ΔG_{mix} is Gibb’s free energy, ΔH_{mix} is the enthalpy of formation, and T is temperature [6].

3.2. Severe Lattice Distortion: The lattice in HEAs consists of a number of different sizes of atoms; which leads to high distortion of lattice in HEAs. This again provides high strain energy in the system. This lattice distortion affects properties like restricted dislocation motion results in increase in solid solution strengthening and the increased electrons scattering declines the transformation kinetics of the material and also leads to low thermal conductivity of the HEAs. Figure 4 shows the distortions that arise due to introduction of different size of atoms in HEAs.

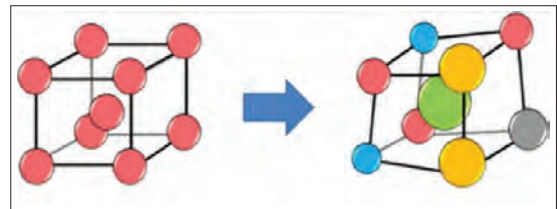


Fig.4. shows lattice distortion effect in the HEAs [2]

3.3 Sluggish Diffusion: It has been seen that the diffusion and the phase transformation kinetics in HEAs are slower than the other conventional alloys. In HEAs, there are varieties of neighboring atoms with different types of atomic bonding and each bonding corresponds to different energy sites. When an atom sits in low energy sites it gets trapped and preferred to stay there and hence, diffusion becomes slower.

3.4. Cocktail Effect: The properties which arise in the HEAs due to inter elemental interaction other than the normally expected properties is considered as the cocktail effect. For example: Al is a soft metal with FCC structure, so, as expected when it is added in the alloy, it would soften the alloy but when it is added it interacts with other alloying elements in the HEAs and

provides a hard BCC phase, thus its addition makes a comparatively hard and brittle phase of the alloy system.

Thus HEAs provide a wide range of applications in various fields like high-temperature applications, applications such as energy-storing materials, radiation-tolerant materials, extremely corrosion-resistant materials, etc [7]. Some of the applications of HEAs are cited below:

- 1) HEAs have been successfully utilized in nuclear power plants as cladding materials and high-pressure vessels due to their improved radiations tolerance and corrosion resistance properties.
- 2) HEAs can form metal hydride with hydrogen and hence can store hydrogen with a very good capacity. Thus, it provides a field for energy storage.
- 3) Due to high-temperature stability, HEAs are applied in aerospace and jet engines.
- 4) HEAs can be used as a high corrosion-resistant coating in many areas and also provide a very stable adhesive bonding during coating.
- 5) Many HEAs like Al₂.08CoCrFeNi are used in electronic applications due to their nearly constant electrical resistivity.
- 6) High entropy carbides and high entropy nitrides are used in biomedical coatings and hard coating materials and diffusion barriers in tool cutting steels etc.

4. Thermodynamics of HEAs

The thermodynamic stability of a system depends on Gibb's free energy of mixing of the system. Gibb's free energy of the system can be defined as the amount of energy set free to make the transformation possible of a chemical reaction at a particular pressure and is expressed as:

$$\Delta G_{mix} = \Delta H_{mix} - T\Delta S_{mix} \quad (1)$$

Less is the value of ΔG_{mix} , more stable is the system and at a constant temperature and constant enthalpy of formation value, this can be achieved by increasing the ΔS_{mix} value only. ΔS_{mix} of a system can be defined as the degree of randomness and entropy and randomness of a system and can be related as:

$$\Delta S_{conf} = k \ln w \quad (2)$$

Where ΔS_{conf} = configurational entropy of the system, k = Boltzman's constant, and w = possible number of arrangements of atoms. But the total mixing entropy, ΔS_{mix} , is the summation of thermal entropy ($\Delta S_{thermal}$), configurational entropy ($\Delta S_{configurational}$), vibrational entropy ($\Delta S_{vibrational}$), and magnetic entropy ($\Delta S_{magnetic}$). ΔS_{mix} is expressed as [8]:

$$\Delta S_{mix} = \Delta S_{thermal} + \Delta S_{configurational} + \Delta S_{vibrational} + \Delta S_{magnetic} \quad (3)$$

Again when the system is considered at a particular temperature the difference in thermal entropy after and before mixing is zero, likewise, the vibrational and magnetic entropy of a system before and after mixing is nearly equal. So, the difference can be considered as zero. Now only configurational entropy comes for the full contribution of ΔS_{mix} . Hence, the total mixing of entropy can be increased by increasing the configurational entropy of the system, which is the basis of stability of the phases in HEAs. For an ideal system with "n" number of components, the ΔS_{conf} [9] can be expressed as:

$$\Delta S_{conf} = -R[x_1 \ln x_1 + x_2 \ln x_2 + \dots + x_n \ln x_n] \quad (4)$$

Where $x_1, x_2 \dots x_n$ are mole fractions of the respective elements. For an equiatomic system with number of elements, n , in liquid solution or its regular solid solution configurational entropy is defined by [8]:

$$\Delta S_{conf} = R \ln_n \quad (5)$$

So, the HEAs in its random solid solution, with single-phase or multiphase have a configurational entropy, $\Delta S_{(conf)} \geq 1.5R$. Mansoori et al. in their

study show that the total configurational entropy of a system with various atomic sizes of atoms not only depends on configurational entropy but also the size factor, atomic fraction, and packing density, and it is expressed as:

$$S_T = S_C(X_i) + S_E(X_i, R_i, \epsilon_i) \quad (6)$$

Where S_T = total configurational entropy of the system, S_C is configurational entropy, $S_C = -R \sum X_i \ln X_i$ and S_E generally has a negative sign and it is the entropy due to size factor R_i , atomic fraction X_i , and packing density. S_E generally decreases with a decrease in ϵ_i (packing density) and the packing density of an alloy decreases with an increase in temperature. So at high temperature, S_T depends only on S_C and not on the second term in the above equation. But at room temperature both the terms in the above equation are valid [10].

More is the negative value of the binary enthalpy of mixing between two elements, more is the chance of formation of intermetallic between the elements. Therefore, considering the phase selection rule for the HEAs the difference in entropy of mixing term should dominate over the difference in enthalpy of mixing.

5. Phase Evolution and Stability in HEAs

In conventional alloys, the minor element generally remains in a small percentage, and if we go on increasing the amount; they no longer remain in solid solution and form intermetallic compounds. The intermetallic compounds are basically hard and brittle phases and are not suitable for any structural applications. In the case of HEAs, there are no major or minor elements. All are principal elements, which are added in equiatomic proportions and the final phase formed is mainly a solid solution. A solid solution has properties almost like metals and behaves like metals. Again the formation of solid solution in the system increases the configurational entropy of the system

remarkably because of the fact that formation of solid solution is associated with the dominance of configurational entropy over enthalpy of formation.

As per Hume Rothery's rule, the size factor, crystal structure, electronegativity, and valence electrons contribute to the formation of solid solution in a binary system. But the rules are not completely applicable in case of HEAs. Many researchers have given some range of values for the above parameters and sets criteria for the formation of solid solutions in HEAs [11][12].

$$\delta = \sqrt{\sum_{i=1}^N X_i (1 - R_i/R_{avg})} \quad (7)$$

$$\Delta H_{mix} = \sum_{i=1, i \neq j}^N \Omega_{ij} X_i X_j, \text{ where } \Omega = 4 + \Delta H_{AB}^{mix} \quad (8)$$

$$VEC = \sum_{i=1}^N X_i (VEC)_i \quad (9)$$

$$\Delta\chi = \sqrt{\sum_{i=1}^N X_i (\chi^i - \chi^{avg})} \quad (10)$$

Where δ = size factor, X_i, X_j = atomic weight fraction of i^{th} and j^{th} element, respectively, Ω = interaction parameter, ΔH_{AB}^{mix} = mixing enthalpy of binary AB alloy, $\Delta\chi$ = change in Pauling electronegativity, X_i = mole fraction, R_i = atomic radius of i^{th} element, R_{avg} is the average radius of all the elements, χ^i = Pauling electronegativity of i^{th} element, and χ^{avg} = average of Pauling electronegativity of all elements.

The entropy of mixing, enthalpy of mixing, size factor, and valence electron concentration (VEC) for the formation of solid solution of HEAs have been studied and given by many authors. The $\Delta S_{mix} > 1.5R$, $-15 \leq \Delta H_{mix} \leq 5$, and $\delta < 0.06$ have been predicted for the formation of solid solution in HEAs. Though there is no direct relation between the VEC and the crystal structure, still the predictions by many of the HEAs researchers for the crystal structure in relation to the VEC value are worth considering. The predictions say when the $VEC < 6.8$, the HEAs have BCC phase, when $VEC > 8$, the phase is FCC, however both

A REVIEW ON EVOLUTION, STABILITY, AND TRANSFORMATION OF PHASES IN HIGH ENTROPY ALLOYS (HEAs)

BCC and FCC phases coexist when VEC lies between 6.8 and 8 [13][14]. These parametric values of different HEA systems are given in the table-1.

Table 1 shows the $\delta\%$, ΔS_{mix} , ΔH_{mix} , Ω , & phase structure of different HEAs.

HEAs	$\delta\%$	ΔS_{mix} (JK ⁻¹ mol ⁻¹)	ΔH_{mix} (kJmol ⁻¹)	Ω	T_m (in K)	Structure	Ref.
CoCrFeNiAl	5.25	13.38	-12.32	1.83	1675	BCC	[14]
CoCrFeNiCu	1.07	13.38	3.20	7.36	1760	FCC	[15]
MnCrFeNiCuAl	4.73	14.90	-5.11	4.62	1580	BCC	[16]
CoCrFeNiMn	0.92	13.38	-4.16	5.77	1792	FCC	
CoCrNiCuAl	5.19	13.38	-6.56	3.23	1584	BCC+FCC	[18]
CoCuNiAl	5.77	11.52	-8.00	2.08	1447	BCC+FCC	[18]
CoCrFeNi	1.06	11.53	-3.75	5.71	1860	FCC	[13]

Figure 5 shows VEC values of three HEA systems. System-1 in figure 5 has the VEC values lies within the range of 6.8 and hence, should have BCC structure denoted by the unfilled circle and square. System-3 has VEC 8 and more, hence, FCC structure, shown as filled circle and square in the figure. The system-2 having VEC value between 6.8 and 8 have both BCC and FCC coexisting together and is shown as half filled circle and square in the figure.

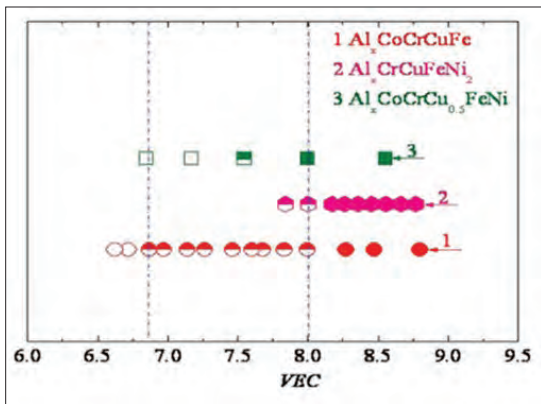


Fig.5. shows VEC value of some HEAs [13]

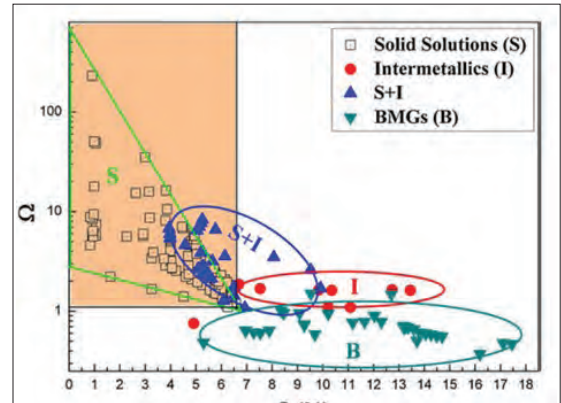


Fig.6. shows the relation between Ω and size factor $\delta\%$ [18]

A combined range of Ω and δ (%) has been shown by brown region in the figure 6 and solid solution forms in HEAs within that range. The contribution of ΔH_{mix} and $T\Delta S_{mix}$ for solid solution formation can be compared in terms of parameter Ω . Generally, ΔH_{mix} dominates over ΔS_{mix} , but at high temperature, both can be compared. And at a particular temperature, both would have the same value and after that temperature $T\Delta S_{mix}$ dominates over ΔH_{mix} and leads to the formation of a solid solution. Ω can be expressed as:

$$\Omega = T_m \Delta S_{mix} / |\Delta H_{mix}| \quad (11)$$

Ω generally has a positive value and $\Omega = 1$, is considered as a critical value for the formation of solid solution. When $\Omega > 1$ and $T\Delta S_{mix}$ value exceeds ΔH_{mix} then solid solution forms and when $\Omega < 1$ and ΔS_{mix} value exceeds $T\Delta S_{mix}$, then intermetallics form [11]. T_m is the melting temperature of the alloys system and can be calculated as:

$$T_m = \sum_{i=1}^N X_i (T_m)_i \quad (12)$$

Sheng Guo et al. in their study showed the effect of VEC on the structure of the final phase of

HEAs. VEC is defined as the number of valence electrons per atom or total number of electrons including d-orbital electrons present in valence band and can be expressed as [13]:

$$e/a = \sum_{i=1}^n X_i (e/a)_i \quad \& \quad VEC = \sum_{i=1}^n X_i (VEC)_i$$

where X_i = mole fraction, $(e/a)_i$ and $(VEC)_i$ are the e/a and VEC of individual element, respectively.

Many authors have recommended the VEC value for the phase stability of HEAs in terms of the structure of phase evolved in HEAs as described in figure 5. Figure 7 shows the combined range of ΔH_{mix} and $\delta\%$ for the formation of amorphous, solid solution and intermetallics in HEAs. A $\delta\%$ value less than 6 and ΔH_{mix} within -15 to 5, indicates formation of solid solution in the system. Hence, a parametric approach has been formulated so far for the determination of phases and stability of phases in HEAs.

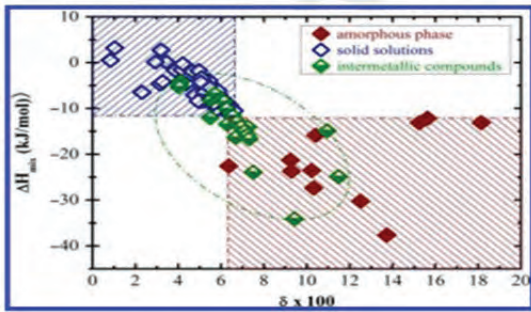


Fig.7. Relation between the enthalpy of mixing and size factor [11]

6. Phase Transformation in HEAs

Early studies have suggested about solid solution formation in the case of HEAs, which is not true and it has also been seen that many HEAs have many intermetallic compounds, many interdendritic segregations of elements. Secondly, it has also been suggested that HEAs should have only simple solid solutions like BCC

and FCC, but the HEAs with intermediate phases have also great potential. Rather the phase study of HEAs attains great importance [19].

Based on the type of phases, the HEAs can have simple ordered phase (SOP), simple disordered phase (SDP), and complex ordered phase (COP). If the microstructure of HEAs has BCC, FCC, HCP, or their derivative phase structures like B2, L12 it is said to be simple, and if it has complex phases like Laves phase, it is said to be complex [19].

The HEAs can be made either by powder metallurgical route or by melting casting route. In the case of cast state, the phases are not in the thermodynamic equilibrium, and phase transition can be seen at elevated temperatures. However, in the case of alloys with BCC or FCC phases, the phase transition is nearly insignificant. For example in Co-Cr-Fe-Mn-Ni (FCC) HEA system no phase transition is seen during its annealing [11]. But, for the HEAs with BCC + FCC, phase changes occur with temperature. For example: in the Al-Co-Cr-Cu-Fe-Ni alloy, the fraction of BCC phase increases with annealing at 800°C or even below temperature. Whereas annealing at a temperature above 800°C the fraction of FCC phase increases [20]. Similar type of approach and effect of aging temperature on the phase transition of AlCoCrCuFeNi HEA was also studied by L.H. Wen et al.

Vikas Shivam et al. in their work studied the metastability of mechanical alloyed AlCoCrFeNi HEA and studied the effect of dynamic heating on the phase stability of the above system. It has been seen that in AlCoCrFeNi system, upon heating decomposes to Ni₃Al with L12 phase, which, upon further heating transform to NiAl with B2 phase and heating above this leads to the formation of σ phase. The precipitation of these intermetallic compounds during heating is

associated with diffusion type transformation as observed by the author [21].

6.1. Effect of addition of elements in phase transition of HEAs

Tsai et al. showed the effect of VEC on the formation and stability of the σ phase in some HEAs. The experiments were conducted in Cr containing HEAs $\text{Al}_x\text{CrFe1.5MnNi0.5}$ with different compositions and with addition of some other elements and showed that formation of σ phase occurs in the systems after aging at 700° in those HEAs which have VEC lies between the range of 6.88 and 7.84 [22]. Again the element which has a positive enthalpy of mixing with other elements in the system generally tends to segregate during phase evolution. Like in the AlCoCrCuFeNi system, Cu has a positive enthalpy of mixing and hence segregates in the interdendritic region. So in the above HEA system BCC/B2, FCC, and a Cu rich phase can be observed and a Cu-rich segregation becomes clear when the Cu amount is greater than 10 atomic percent. Again the addition of Al in the HEA system causes transition of FCC to BCC phase. In AlCoCrCuFeNi system, when the Al amount is more than sufficient the BCC phase again decompose to a (Cr, Fe)-rich BCC phase and an (Al, Ni)-rich B2 phase [23].

The addition of Ti to the HEA system generally leads to the formation of intermetallic compounds as in the case of the Al-Co-Cr-Cu-Fe-Ni system. This happens due to the high negative value of enthalpy of mixing of Ti with other elements. Similarly, the addition of Mo in HEAs causes the formation of (Fe, Co, Ni, Cr) rich, hard and brittle σ phase. Mn addition also leads to the age-hardening effect in the $\text{Al}_x\text{CrFe1.5MnNi0.5}$ system due to the transformation of the BCC phase in the original matrix to the σ phase. This

transformation generally occurs near the surface and thus enhances the hardness value to a large extent [24].

Researchers did not limit their work by studying the effect of addition metallic elements to the HEAs, the effect of addition of nonmetallic elements has also been studied by many authors. It is noted that the addition of Boron (B) and Silicon (Si) in the HEA system leads to the formation of borides and silicides which are the valence compounds and hence, results in an increase in the hardness value considerably. But in many cases, localized distribution of these valence compounds decreases its effectiveness in enhancing the hardness value [24][25].

6.2. Pressure induced phase transformation in HEAs

It has been seen that not only temperature but also pressure has great importance in the phase transformation of HEAs. Fei Zhang et.al. used Diamond anvil cells (DAC) for high pressure study of HEAs and showed the effect of medium and the initial grain size during inducing pressure. The FCC HEAs eg. CoCrFeMnNi generally change to HCP structure by applying high pressure in helium medium and the transition starts at a pressure of about 29 GPa. The transition here is irreversible in nature. When the medium is silicon oil, then transformation starts at about 7GPa and for amorphous boron medium, the transformation pressure is 6 GPa. This transformation is observed to be a martensitic type transformation from FCC to HCP [26]. Similarly, the effect of grain size on onset pressure for nano grain CoCrFeMnNi HEA has been studied by Zhang et al. The onset pressure was observed as 12.3 GPa and for larger grain, it was found to be 6.9 GPa [27].

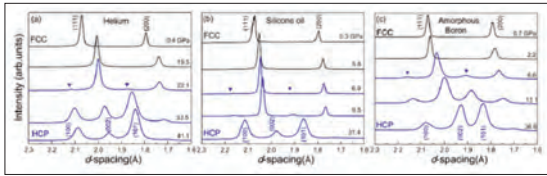


Fig.8. shows in situ high-pressure XRD patterns and unset pressure of the CoCrFeMnNi HEA in (a) helium, (b) silicone oil, and (c) amorphous boron [26][27]

The disordered BCC HEAs are generally stable and don't undergo pressure-induced phase transformation up to very high pressure. But the transformation can be seen with ordered BCC HEAs at a temperature of 17.6 GPa as studied by Cheng et al. in equimolar AlCoCrFeNi HEA system [28]. For HCP type HEAs, the pressure induced phase transformation occurs in a series of steps. From HCP to disordered FCC i.e. HCP→Sm-TYPE→dHCP→dFCC [27][29][30]. The HCP structure changes to Sm type at around 4.4 GPa, which changes to dHCP at nearly 26.7 GPa, then transition to dFCC phase occurs at around 40.2 GPa which is shown in the figure 9.

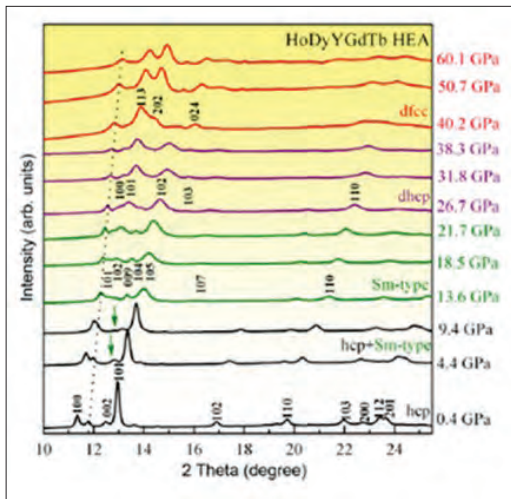


Fig.9. shows the in-situ high-pressure XRD patterns of the HoDyYGdTb HEA [29]

6.3. Elemental segregation in HEAs.

Y.F. Ye et al. studied the elemental segregation in as cast FeNiCoCrCu alloy system. Experimental observation showed Cu rich and Cu lean regions. This Cu rich interdendritic region is basically due to the positive enthalpy of mixing of Cu with the other four elements of the system, which can be seen from the figure 10. The number between any of the two elements here indicates the enthalpy of mixing between those two.

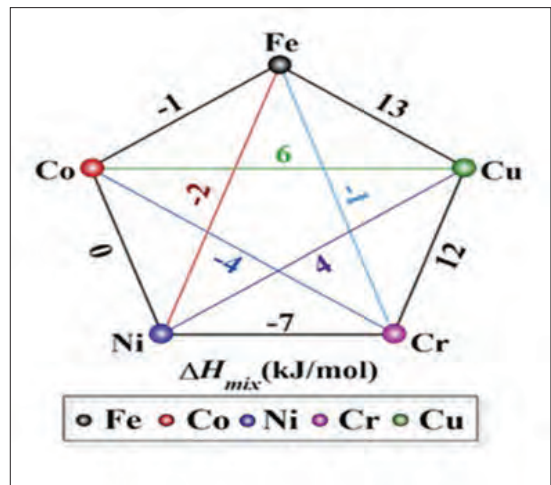


Fig.10. shows the binary mixing enthalpy value of different elements in the considered HEA system [23]

One of the benefits of this elemental segregation is that it can stabilise the random solid solution in HEAs by converting from high-temperature equiatomic to low-temperature non-equiatomic composition [23]. Again the author suggested a parametric value for the likeliness of occurring of elemental segregation in HEAs [23][24].

$$\lambda = \sqrt{\frac{\sum_{i=1}^n (c_i^{eq} - c_i)^2}{\sum_{i=1}^n (c_i)^2}}$$

A REVIEW ON EVOLUTION, STABILITY, AND TRANSFORMATION OF PHASES IN HIGH ENTROPY ALLOYS (HEAs)

Here, C_i and C_i^{eq} are the equiatomic and optimum composition, respectively.

The author suggested that the larger is the λ value more is the likeliness of the elemental segregation [23].

7. Present Status in the Field of HEAs

One of the significant research of today is combining concept of high entropy alloy to the steel, that has been studied by Dierk Raabe et al. in their research. The non equiatomic proportion formula for high entropy alloy applied to make high entropy steel with the additional idea of adding interstitial element like C into the solid solution matrix. The final product is a single phase FCC solid solution showing some extraordinary mechanical properties than the conventional austenitic or other steel. This new steel possesses ultimate tensile strength upto 1000 MPa, tensile elongation of 100% in many cases, and up to 70% elongation to the fracture point in quasi-static tensile tests in cryogenic temperature i.e. at -50° [31]. The ultimate tensile strength vs total elongation (ductility) of the different steel is well compared with the high entropy steel which is represented in figure 11.

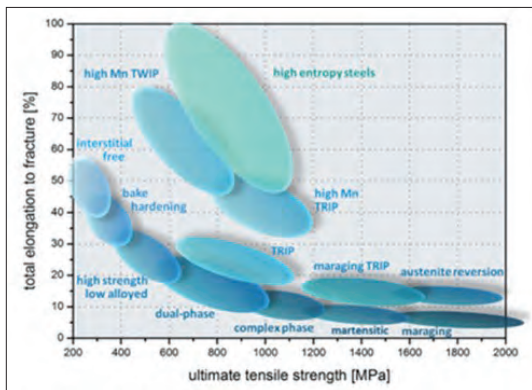


Fig.11. shows the a comparison between the UTS and total elongation of different steels and high entropy steel [31].

Hydrogen is being an ideal carrier of energy for the present and future era, where its storage is still a promising task in the realm of research today. HEAs are providing an encouraging field for the study of its hydrogen storage capacity. Fundamentally HEAs, in the form of metallic hydride can store a large amount of hydrogen. The research demonstrates that the hydrogen to metallic (H/M) ratio which indicates the hydrogen storage capacity of any materials, is 2.5 for transition high entropy alloys. The alloy composition and design are the deciding factors whether the HEAs will provide room temperature storage or high-temperature storage [32][33]. High lattice distortion which is a special characteristic in HEA is the reason for making such absorption possible. Special structural phase such as the Laves phase is also making this possible in some HEAs. The criteria need to be satisfied by HEAs for room temperature hydrogen storage is VEC equals 6.4, thermodynamic stability of single-phase structure and AB_2H_3 hydride formation. The dehydrogenation can also be possible by applying some special conditions [34][35].

HEAs are now being studied for their irradiation tolerance and for their utilisation as nuclear material. Zinkle et al. cited three points for an irradiation tolerance material at high temperature, 1. a matrix with irradiation tolerance capability, 2. A material in which vacancies remain immobile at high operating temperature, 3. a material which has high density and sink strength for point defects recombination [36]. Using HEAs for nuclear application could be supported by point 1 and 3 and the freedom associated with compositional design of HEAs also provides a great opportunity to obtain material with suitable characteristics for irradiation tolerance [37]. HEAs are proving

themselves as a potential material for cryogenic application along with its high temperature stability [38]. Still some HEAs are identified for absorption of microwave [39]. Some studies are going on utilising HEAs as coating in different substrates for protection against corrosion, wear, and abrasion where conventional alloys fail [40].

8. Summary

High entropy alloys are the material of the future having great potential to beat the base element concept of conventional alloys. But its characteristics and properties are yet to be explored. Lots of research works are yet to be done. While considering the properties of a material, how the structure-properties correlation concept can be ignored and for that, the microstructure and phases, the transition of phases have to be understood. We are trying to put some light on understanding the phase evolution, phase stability, and transformation of phases in HEAs. It has been observed that despite the sluggish diffusion, a distorted lattice of HEAs, many parameters under special conditions lead to the transition of phases and hence properties. The presence of different elements affects the evolution and stability of different phases. While some elements like Cu and Ge leads to elemental segregation. Though single-phase solid solution is the uniqueness of HEAs, under certain conditions some intermetallic compounds like sigma phase and Laves phases are seen in the microstructure. In some HEAs, martensitic type transformation is also observed. Some HEAs shows pressure induced transformation with different onset pressure value. Hence, this paper is a basic review of the phase game in HEAs.

Acknowledgement

The authors would like to express gratitude to the department of Metallurgical and Materials

Engineering, VSSUT, Burla, Odisha for all support during the study of this topic. The authors are very much thankful to Dr. Madhusmita Behera, IMMT, Bhubaneswar, Odisha for her scholarly guidance and time to time valuable discussions regarding the topic.

References

- [1] Y. Zhang, *High-Entropy Materials-A Brief Introduction*, vol. 113, no. 9. 2019.
- [2] P. P. B. B.S. Murty, J.W. Yeh, S. Ranganathan, *High-Entropy alloys*, vol. 71, no. 3. 2015.
- [3] E. P. George, D. Raabe, and R. O. Ritchie, "High-entropy alloys," *Nat. Rev. Mater.*, vol. 4, no. 8, pp. 515–534, 2019, doi: 10.1038/s41578-019-0121-4.
- [4] J. W. Y. B.S. Murty and S. Ranganathan, *High-Entropy Alloys*, vol. 93, no. 4. 1999.
- [5] J.-W. Y. K. L. Z. Michael C. Gao, *High-Entropy Alloys Fundamentals and Applications*. 2016.
- [6] Y. J. Zhou, Y. Zhang, Y. L. Wang, and G. L. Chen, "Solid solution alloys of AlCoCrFeNi Tix with excellent room-temperature mechanical properties," *Appl. Phys. Lett.*, vol. 90, no. 18, 2007, doi: 10.1063/1.2734517.
- [7] X. Yan and Y. Zhang, "Functional properties and promising applications of high entropy alloys," *Scr. Mater.*, vol. 187, pp. 188–193, 2020, doi: 10.1016/j.scriptamat.2020.06.017.
- [8] W. Zhang, P. K. Liaw, and Y. Zhang, "Science and technology in high-entropy alloys," vol. 61, no. 1, pp. 2–22, 2018.
- [9] W. Zhang, P. K. Liaw, and Y. Zhang, "Science and technology in high-entropy alloys," *Science China Materials*, vol. 61, no. 1. Science China Press, pp. 2–22, Jan. 01, 2018, doi: 10.1007/s40843-017-9195-8.
- [10] Y. F. Ye, Q. Wang, J. Lu, C. T. Liu, and Y. Yang, "High-entropy alloy: challenges and prospects," *Materials Today*, vol. 19, no. 6. Elsevier B.V., pp. 349–362, Jul. 01, 2016, doi: 10.1016/j.mattod.2015.11.026.
- [11] S. Guo, "Phase selection rules for cast high entropy alloys: An overview,"

A REVIEW ON EVOLUTION, STABILITY, AND TRANSFORMATION OF PHASES IN HIGH ENTROPY ALLOYS (HEAs)

- Mater. Sci. Technol. (United Kingdom)*, vol. 31, no. 10, pp. 1223–1230, 2015, doi: 10.1179/1743284715Y.0000000018.
- [12] Y. Zhang, Y. J. Zhou, J. P. Lin, G. L. Chen, and P. K. Liaw, "Solid-solution phase formation rules for multi-component alloys," *Adv. Eng. Mater.*, vol. 10, no. 6, pp. 534–538, 2008, doi: 10.1002/adem.200700240.
- [13] S. Guo, C. Ng, J. Lu, and C. T. Liu, "Effect of valence electron concentration on stability of fcc or bcc phase in high entropy alloys," *J. Appl. Phys.*, vol. 109, no. 10, 2011, doi: 10.1063/1.3587228.
- [14] S. Guo and C. T. Liu, "Phase stability in high entropy alloys: Formation of solid-solution phase or amorphous phase," *Prog. Nat. Sci. Mater. Int.*, vol. 21, no. 6, pp. 433–446, 2011, doi: 10.1016/S1002-0071(12)60080-X.
- [15] J. W. Yeh et al., "Nanostructured high-entropy alloys with multiple principal elements: Novel alloy design concepts and outcomes," *Adv. Eng. Mater.*, vol. 6, no. 5, pp. 299–303, 2004, doi: 10.1002/adem.200300567.
- [16] J. W. Yeh, S. Y. Chang, Y. Der Hong, S. K. Chen, and S. J. Lin, "Anomalous decrease in X-ray diffraction intensities of Cu-Ni-Al-Co-Cr-Fe-Si alloy systems with multi-principal elements," *Mater. Chem. Phys.*, vol. 103, no. 1, pp. 41–46, 2007, doi: 10.1016/j.matchemphys.2007.01.003.
- [17] Y. J. Hsu, W. C. Chiang, and J. K. Wu, "Corrosion behavior of FeCoNiCrCux high-entropy alloys in 3.5% sodium chloride solution," *Mater. Chem. Phys.*, vol. 92, no. 1, pp. 112–117, 2005, doi: 10.1016/j.matchemphys.2005.01.001.
- [18] X. Yang and Y. Zhang, "Prediction of high-entropy stabilized solid-solution in multi-component alloys," *Mater. Chem. Phys.*, vol. 132, no. 2–3, pp. 233–238, 2012, doi: 10.1016/j.matchemphys.2011.11.021.
- [19] M. H. Tsai and J. W. Yeh, "High-entropy alloys: A critical review," *Mater. Res. Lett.*, vol. 2, no. 3, pp. 107–123, 2014, doi: 10.1080/21663831.2014.912690.
- [20] L. H. Wen, H. C. Kou, J. S. Li, H. Chang, X. Y. Xue, and L. Zhou, "Effect of aging temperature on microstructure and properties of AlCoCrCuFeNi high-entropy alloy," *Intermetallics*, vol. 17, no. 4, pp. 266–269, 2009, doi: 10.1016/j.intermet.2008.08.012.
- [21] V. Shivam, J. Basu, V. K. Pandey, Y. Shadangi, and N. K. Mukhopadhyay, "Alloying behaviour, thermal stability and phase evolution in quinary AlCoCrFeNi high entropy alloy," *Adv. Powder Technol.*, vol. 29, no. 9, pp. 2221–2230, 2018, doi: 10.1016/j.apt.2018.06.006.
- [22] M. H. Tsai, K. Y. Tsai, C. W. Tsai, C. Lee, C. C. Juan, and J. W. Yeh, "Criterion for sigma phase formation in Cr- and V-Containing high-entropy alloys," *Mater. Res. Lett.*, vol. 1, no. 4, pp. 207–212, 2013, doi: 10.1080/21663831.2013.831382.
- [23] Y. F. Ye, Q. Wang, Y. L. Zhao, Q. F. He, J. Lu, and Y. Yang, "Elemental segregation in solid-solution high-entropy alloys: Experiments and modeling," *J. Alloys Compd.*, vol. 681, pp. 167–174, 2016, doi: 10.1016/j.jallcom.2016.04.239.
- [24] Y. X. Zhuang, W. J. Liu, Z. Y. Chen, H. D. Xue, and J. C. He, "Effect of elemental interaction on microstructure and mechanical properties of FeCoNiCuAl alloys," *Mater. Sci. Eng. A*, vol. 556, pp. 395–399, 2012, doi: 10.1016/j.msea.2012.07.003.
- [25] C. C. Tung, J. W. Yeh, T. tsung Shun, S. K. Chen, Y. S. Huang, and H. C. Chen, "On the elemental effect of AlCoCrCuFeNi high-entropy alloy system," *Mater. Lett.*, vol. 61, no. 1, pp. 1–5, Jan. 2007, doi: 10.1016/J.MATLET.2006.03.140.
- [26] F. Zhang and Z. Z. and Q. Z. , Hongbo Lou, Benyuan Cheng, "High-Pressure Induced Phase Transitions in High-Entropy Alloys: A Review," *Entropy*, vol. 21, no. 3, 2019, doi: 10.3390/e21030239.
- [27] C. L. Tracy et al., "High pressure synthesis of a hexagonal close-packed phase of the high-entropy alloy CrMnFeCoNi," *Nat. Commun.*, vol. 8, no. May, pp. 1–6, 2017, doi: 10.1038/ncomms15634.
- [28] B. Cheng et al., "Pressure-induced phase transition in the AlCoCrFeNi high-entropy alloy," *Scr. Mater.*, vol. 161, pp. 88–92, 2019, doi: 10.1016/j.scriptamat.2018.10.020.

A REVIEW ON EVOLUTION, STABILITY, AND TRANSFORMATION OF PHASES IN HIGH ENTROPY ALLOYS (HEAs)

- [29] P. F. Yu et al., "Pressure-induced phase transitions in HoDyYGdTb high-entropy alloy," *Mater. Lett.*, vol. 196, pp. 137-140, 2017, doi: 10.1016/j.matlet.2017.02.136.
- [30] F. Zhang et al., "Effects of non-hydrostaticity and grain size on the pressure-induced phase transition of the CoCrFeMnNi high-entropy alloy," *J. Appl. Phys.*, vol. 124, no. 11, 2018, doi: 10.1063/1.5046180.
- [31] D. Raabe, C. C. Tasan, H. Springer, and M. Bausch, "From high-entropy alloys to high-entropy steels," *Steel Res. Int.*, vol. 86, no. 10, pp. 1127-1138, 2015, doi: 10.1002/srin.201500133.
- [32] P. Edalati et al., "Reversible room temperature hydrogen storage in high-entropy alloy TiZrCrMnFeNi," *Scr. Mater.*, vol. 178, pp. 387-390, Mar. 2020, doi: 10.1016/j.scriptamat.2019.12.009.
- [33] M. M. Nygård, G. Ek, D. Karlsson, M. Sahlberg, M. H. Sørby, and B. C. Hauback, "Hydrogen storage in high-entropy alloys with varying degree of local lattice strain," *Int. J. Hydrogen Energy*, vol. 44, no. 55, pp. 29140-29149, Nov. 2019, doi: 10.1016/j.ijhydene.2019.03.223.
- [34] M. Sahlberg, D. Karlsson, C. Zlotea, and U. Jansson, "Superior hydrogen storage in high entropy alloys," *Sci. Rep.*, vol. 6, Nov. 2016, doi: 10.1038/srep36770.
- [35] B. Sakintuna, F. Lamari-Darkrim, and M. Hirscher, "Metal hydride materials for solid hydrogen storage: A review," *Int. J. Hydrogen Energy*, vol. 32, no. 9, pp. 1121-1140, 2007, doi: 10.1016/j.ijhydene.2006.11.022.
- [36] S. J. Zinkle and L. L. Snead, "Designing radiation resistance in materials for fusion energy," *Annu. Rev. Mater. Res.*, vol. 44, no. March, pp. 241-267, 2014, doi: 10.1146/annurev-matsci-070813-113627.
- [37] E. J. Pickering, A. W. Carruthers, P. J. Barron, S. C. Middleburgh, D. E. J. Armstrong, and A. S. Gandy, "High-entropy alloys for advanced nuclear applications," *Entropy*, vol. 23, no. 1, pp. 1-28, 2021, doi: 10.3390/e23010098.
- [38] B. Gludovatz, A. Hohenwarter, D. Catoor, E. H. Chang, E. P. George, and R. O. Ritchie, "A fracture-resistant high-entropy alloy for cryogenic applications," *Science (80-.)*, vol. 345, no. 6201, pp. 1153-1158, 2014, doi: 10.1126/science.1254581.
- [39] J. W. Yeh, "Recent progress in high-entropy alloys," *Ann. Chim. Sci. des Mater.*, vol. 31, no. 6, pp. 633-648, 2006, doi: 10.3166/acsm.31.633-648.
- [40] R. K. Duchaniya, U. Pandel, and P. Rao, "Coatings based on high entropy alloys: An overview," *Mater. Today Proc.*, vol. 44, no. xxxx, pp. 4467-4473, 2020, doi: 10.1016/j.matpr.2020.10.720.

SYNTHESIS AND CHARACTERIZATION OF MAGNESIUM ALUMINATE ($MgAl_2O_4$) SPINEL THROUGH SOLID STATE PRESSURELESS SINTERING

Abdur Rouf^a, Krishna Priya Yagati^a and Manab Mallik^{a1}

^aDepartment of Metallurgy & Materials Engineering, National Institute of Technology, Durgapur, West Bengal.
rouf.gagan@gmail.com

Abstract: This study has attempted to synthesize stoichiometric $MgAl_2O_4$ spinel from commercially available micro fines powder of sintered MgO and calcined Al_2O_3 through single-stage sintering route. The effect of compaction pressure and sintering temperature on density, densification parameter, volume shrinkage, pore characteristics and microstructure development studied. Oxide powders were mixed with appropriate binder and pellet samples were prepared at uniaxial compaction pressures between 120 MPa to 150 MPa. The compacted samples sintered in conventional solid state sintering in the temperature of 1550°C, 1600°C, and 1650°C. Phase analysis of the sintered samples in XRD was carried out to check the $MgAl_2O_4$ formation at various compaction pressures and temperatures. Evaluation and co-relation of density, densification parameter, volume shrinkage, pore characteristics and microstructure in terms of processing parameters performed. Results show that bulk density, densification parameter and volume shrinkage percentage increased with increasing sintering temperature from 1550°C to 1650°C. Analysis of porosity shows that apparent porosity is inversely proportional with the sintering temperature. Microstructure and XRD analyses reveal that MgO and Al_2O_3 have transformed into $MgAl_2O_4$ spinel.

Keywords: Solid-state sintering; densification; spinel; refractory.

1. Introduction

Magnesium Aluminate spinel is an interesting material for its unique combination of chemical as well as physical properties such as chemical inertness, excellent mechanical properties, low thermal expansion coefficient, high melting temperature, and high spalling resistance. This material has wide application as refractory, including cement rotary kilns and steel ladles. The use of $MgAl_2O_4$ spinel in steel ladle has increased daily due to its excellent slag corrosion and erosion resistance.

Gradual improvement in slag corrosion resistance, high temperature mechanical behavior and thermal shock resistance with nano $MgAl_2O_4$ spinel formation, and improved slag corrosion resistance in RH degasser furnace for producing rail steel due to addition of $MgAl_2O_4$ spinel or formation of in-situ $MgAl_2O_4$

in the matrix of refractory were investigated by several authors [1-5]. Jeon et al. evaluated the corrosion and erosion properties of $MgAl_2O_4$ spinel refractory of different compressive strengths with steelmaking slag [1]. Tong et al. [2] analyzed the corrosion mechanism of $Al-MgO-MgAl_2O_4$ refractories used at the bottom of a Ruhrstahl Heraeus (RH) degasser-refining furnace for producing rail steel. Musante et al. studied two types of commercial $Al_2O_3-MgO-C$ (AMC) refractories, and found advantages of AMC refractory due to the formation of $MgAl_2O_4$ spinel by solid-state reaction of MgO and reactive Al_2O_3 [3]. A stoichiometric dense $MgAl_2O_4$ spinel was prepared [4] through conventional double stage sintering. The slag erosion and penetration performance were studied after incorporating 20% of the spinel in Al_2O_3 and $MgO-C$ refractories separately. Results indicate that the presence of $MgAl_2O_4$ improves

SYNTHESIS AND CHARACTERIZATION OF MAGNESIUM ALUMINATE ($MgAl_2O_4$) SPINEL THROUGH SOLID STATE PRESSURELESS SINTERING

slag corrosion behavior of Al_2O_3 - MgO - C (AMC) [1,2,4]. The effects of $MgAl_2O_4$ spinel produced from nanoscale Al_2O_3 powder and MgO powder on the physical properties and thermal shock resistance of MgO - C slide plate refractory were investigated by Gu et al. [5].

The synthesis method influences the production of pure and dense $MgAl_2O_4$ spinel. The conventional synthesis methods are mechanical oxides and salt mixtures calcinations. Many unconventional methods like precipitation and calcination [6], co-precipitation followed by densification through double stage sintering [7], low-temperature sol-gel synthesis [8], gel combustion [9], hot isostatic pressing [10-11], shock compression [12], and chemical synthesis [18] are available. Most of the above mentioned process requires expensive precursors, solvent, and double stage sintering techniques, which are not suitable for mass production like refractory materials. However, Ganesh [13] reviewed various synthesis methods, processing routes, and properties of $MgAl_2O_4$ spinel. Ghosh et al. [14] studied the formation, densification, mechanical properties, and microstructural properties of $MgAl_2O_4$ spinel from Indian magnesite and calcined alumina. The $MgAl_2O_4$ spinel was produced through solid-state sintering with different additives and studied formation and densification [15]. An investigative study on spinel formation at different ratios of Al_2O_3 and MgO powders after calcining at different temperatures and subsequent high-temperature sintering was carried out [16]. In another study, the effect of particle size of the reactant oxides on the formation of $MgAl_2O_4$ spinel and properties was analyzed [17].

In most previous studies, double stage sintering or pre-calcination followed by sintering was required due to the volume expansion of spinel about 5-8% during solid-state sintering [13, 25]. This study has attempted to synthesize stoichiometric spinel from commercial grades of

MgO and Al_2O_3 powders without any additive or sintering aid through a conventional solid-state sintering route. Further, the present study focuses on the effects of compaction pressure on density, volume shrinkage, and densification parameters.

2. Experimental:

Dead burnt magnesia (DBM) and calcined alumina powder were obtained from Refractory Unit, Steel Authority of India Ltd., Ramgarh, Jharkhand. The chemical composition for both the powders is in the as-received condition from SAIL refractory unit. The chemical composition is mentioned in Table 1. XRD analysis was carried out for the magnesia and alumina powders in XRD, PANalytical. Particle size distribution for the raw powders performed in a laser particle size fraction analyzer, Microtrac S3500. Raw powders were investigated under field emission scanning electron microscopy (FESEM) outfitted with energy dispersive X-ray (EDX) analysis.

Dry mixed powder (28% DBM & 72% calcined alumina) and 5% aqueous polyvinyl alcohol (PVA) were mixed in a mixer grinder. Mixed powders were compacted into 30 mm diameter and 6 mm height pellet sample with varying uniaxial pressure at 120 MPa, 135 MPa, and 150 MPa in 100 Ton Carver Press, Model: CMV100-15-X. Each of the sample sintered in laboratory furnace (model: HT0627QNCAG/1750) from 1550°C to 1650°C for holding of 2 hours. Temperature increased at rate of 4°C/min. till 1400°C and 2.5°C/min. till 1550°C / 1600°C / 1650°C as required. Using Archimedes' principle, the apparent porosity (AP) and bulk density (BD) were analyzed with the water displacement method. Densification parameter, as well as shrinkage of the sintered samples, was calculated. Sintered samples were paper polished followed by cloth polishing. Polished samples were thermally etched [19] at 1200°C in a high-temperature furnace.

SYNTHESIS AND CHARACTERIZATION OF MAGNESIUM ALUMINATE ($MgAl_2O_4$) SPINEL THROUGH SOLID STATE PRESSURELESS SINTERING

Thermally etched samples were gold coated, and microstructure analysis was carried out under FESEM.

3. Result & Discussion:

3.1 Raw material characterization

The chemical composition of DBM and calcined alumina is mentioned in Table 1. Similar raw materials were used for the synthesis of spinel by previous authors [15, 20-22, 27]. Except periclase and corundum, no other major phases

were found in the XRD plots of the magnesia and alumina powders as shown in Fig.2. Particle size distribution of magnesia and alumina powders is shown in Fig.1. D50 values were 2.13 μm and 17.53 μm for Al_2O_3 and MgO powders, respectively. The size and morphology of the raw powders observed under FESEM (Fig.3). Raw powder characterization indicates that DBM is coarser than alumina [15]. Crystal structures of DBM and calcined alumina are cubic and hexagonal, respectively.

Table 1. Chemical compositions of DBM and calcined alumina

Raw materials	MgO	Fe ₂ O ₃	Al ₂ O ₃	SiO ₂	CaO	Cr ₂ O ₃	B ₂ O ₃	Na ₂ O
DBM	96.00	0.50	0.20	0.80	2.70	0.20	0.002	
Calcined Alumina		0.011	99.50	0.011				0.31

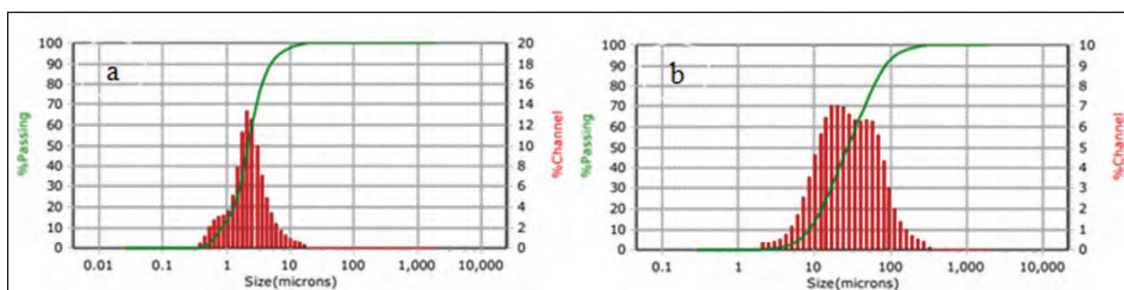


Figure 1: Particle size distribution (a) Al_2O_3 powder and (b) DBM powder

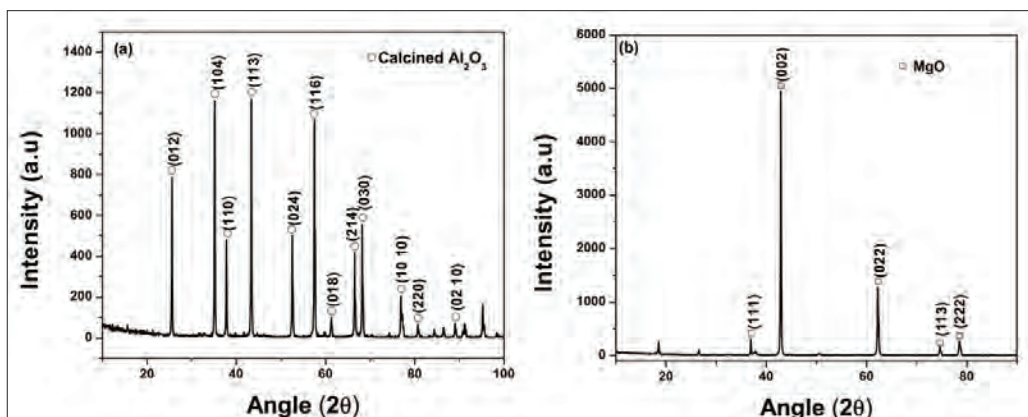


Figure 2: XRD plot of (a) Al_2O_3 powder and (b) DBM powder

SYNTHESIS AND CHARACTERIZATION OF MAGNESIUM ALUMINATE ($MgAl_2O_4$) SPINEL THROUGH SOLID STATE PRESSURELESS SINTERING

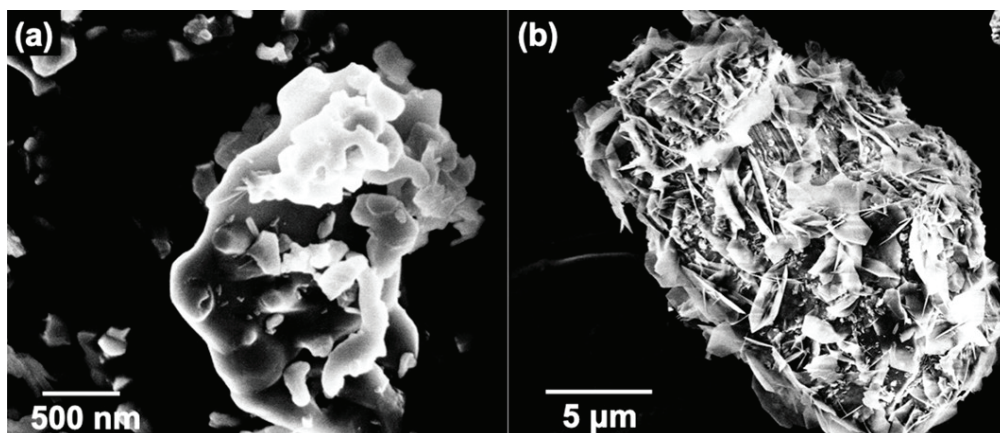


Figure3: Raw powder under FESEM (a) Al_2O_3 and (b) DBM

3.2 Density and densification parameters

Bulk densities (BD) vary from 2.64 gm/cm^3 to 3.08 gm/cm^3 after sintering at 1550°C, 1600°C, and 1650°C and compacted at 150MPa pressure, shown in Fig.4a. The apparent porosities (AP) are in decreasing trend from 18.81% to 6.09% with sintering temperature from 1550°C to 1650°C, shown in Fig.4a. The apparent porosity of 18.81% after sintering at 1550°C is lower than the apparent porosity of a spinel batch without a ZnO additive [22]. After sintering at 1600°C, the density is 3.05 gm/cm^3 , which is in line

with the density of a spinel batch without ZrO_2 additive [20]. The density and apparent porosity after sintering at 1650°C without any sintering aid is similar to another study [15]. The AP decreases with increasing sintering temperature from 1550°C to 1650°C due to faster diffusion rate of ions at higher temperatures. Volume shrinkage was highest of 25.43% at 1650°C and lowest of 15.22% at 1550°C, shown in Fig.4b. Densification parameter was in increasing trend with increasing sintering temperature, shown in Fig.4b.

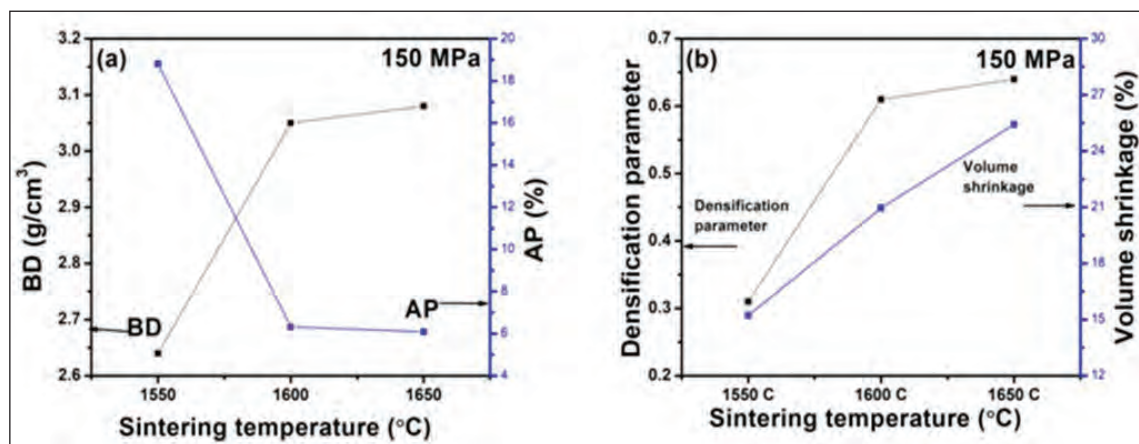


Figure4: (a) AP% and BD and (b) Densification parameter and % of volume shrinkage after sintering at 150MPa.

SYNTHESIS AND CHARACTERIZATION OF MAGNESIUM ALUMINATE ($MgAl_2O_4$) SPINEL THROUGH SOLID STATE PRESSURELESS SINTERING

Bulk density is in increasing trend and apparent porosity is in decreasing trend with the increase of compaction pressure at all sintering temperatures, as shown in Fig.5a, 5c, 5e. Volume shrinkage and densification parameter parameters are proportionally increased with increase of compaction pressure at all sintering temperatures except densification parameter at 1600°C, as shown in Fig.5b, 5d, 5f. Densification parameter in all compaction pressures after

sintering at 1600°C is almost same. The variation in AP, BD, and densification parameter and volume shrinkage% was minor with the variation of compaction pressure in a same sintering temperature. But the variation in AP, BD, and densification parameter and volume shrinkage % is prominent in case of different sintering temperature and in same compaction pressure. However, densification of spinel occurs at 1650°C [24].

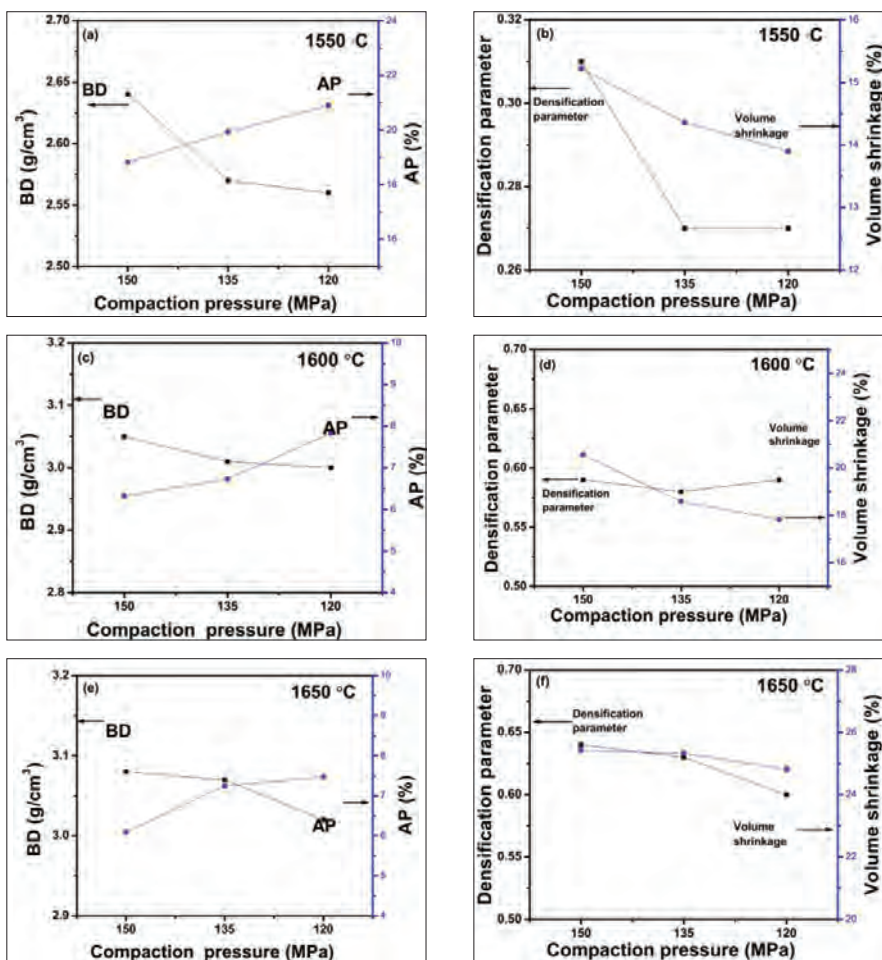


Figure 5: BD and AP% (a) 1550°C, (c) 1600°C, (e) 1650°C; and densification parameter and volume shrinkage% (b) 1550°C, (d) 1600°C, (f) 1650°C at compaction pressure of 150 MPa, 135 MPa, 120 MPa.

SYNTHESIS AND CHARACTERIZATION OF MAGNESIUM ALUMINATE ($MgAl_2O_4$) SPINEL THROUGH SOLID STATE PRESSURELESS SINTERING

3.3 Pore analysis

Analysis of pore size and sphericity of pore was carried out for a pellet sample sintered at $1600^\circ C$ and compacted at 150 MPa pressure. Fig. 6a indicates the 3-D picture of the pellet sample with pore distribution of different dimensions. The scale on the left edge of Fig.6a details the dimensions of the pores with color variations. Two large pores of diameters, 723 μm , and 647 μm , are visible in the 3-D picture. Most pores are below 200 μm , shown in Fig.6b, whereas most pores' sphericity is above 0.4, as shown in Fig.6c.

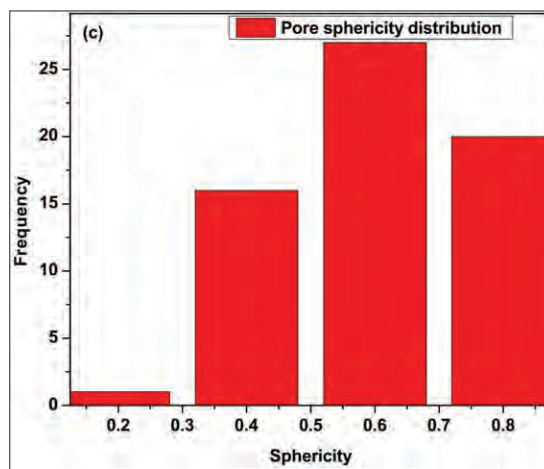
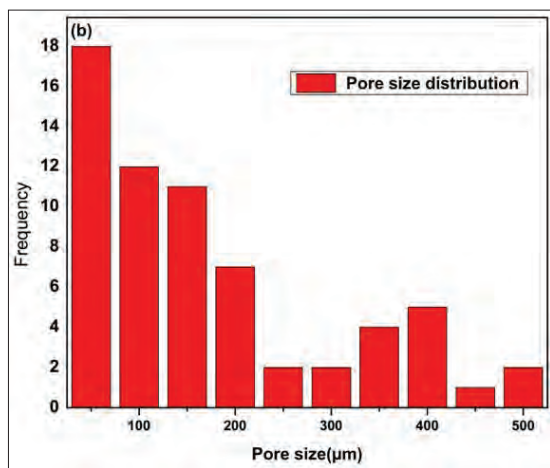
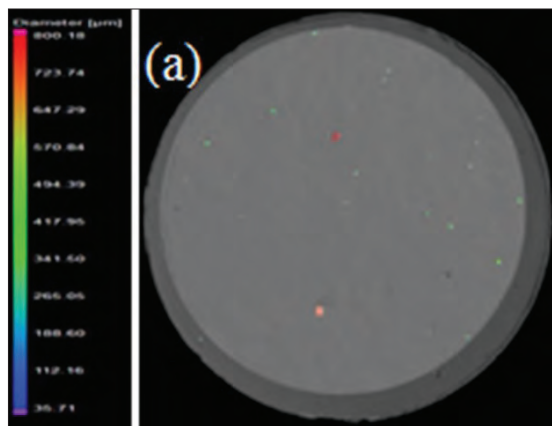


Figure6: X-ray computed tomography of sintered sample (a) 3-D picture with pores, (b) Pore size distribution and (c) Pore sphericity

3.4 Spinel formation

XRD plots of the sintered samples compacted from 120MPa to 150MPa pressure and sintered from $1550^\circ C$ to $1650^\circ C$ temperature is shown in Fig.7. All the samples showing major peaks of (111), (022), (113), (004), (115) and (044) which indicate the formation of $MgAl_2O_4$ [23] spinel. One minor peak (002) of MgO found in case of two samples: one is sintered at $1550^\circ C$ (Fig.7a) and other is sintered at $1600^\circ C$ (Fig.7b), and both samples compacted at 120MPa pressure. However, all the samples sintered from $1550^\circ C$ to $1650^\circ C$ temperature and compacted from 120MPa to 150MPa pressure were transformed into $MgAl_2O_4$ spinel.

SYNTHESIS AND CHARACTERIZATION OF MAGNESIUM ALUMINATE (MgAl_2O_4) SPINEL THROUGH SOLID STATE PRESSURELESS SINTERING

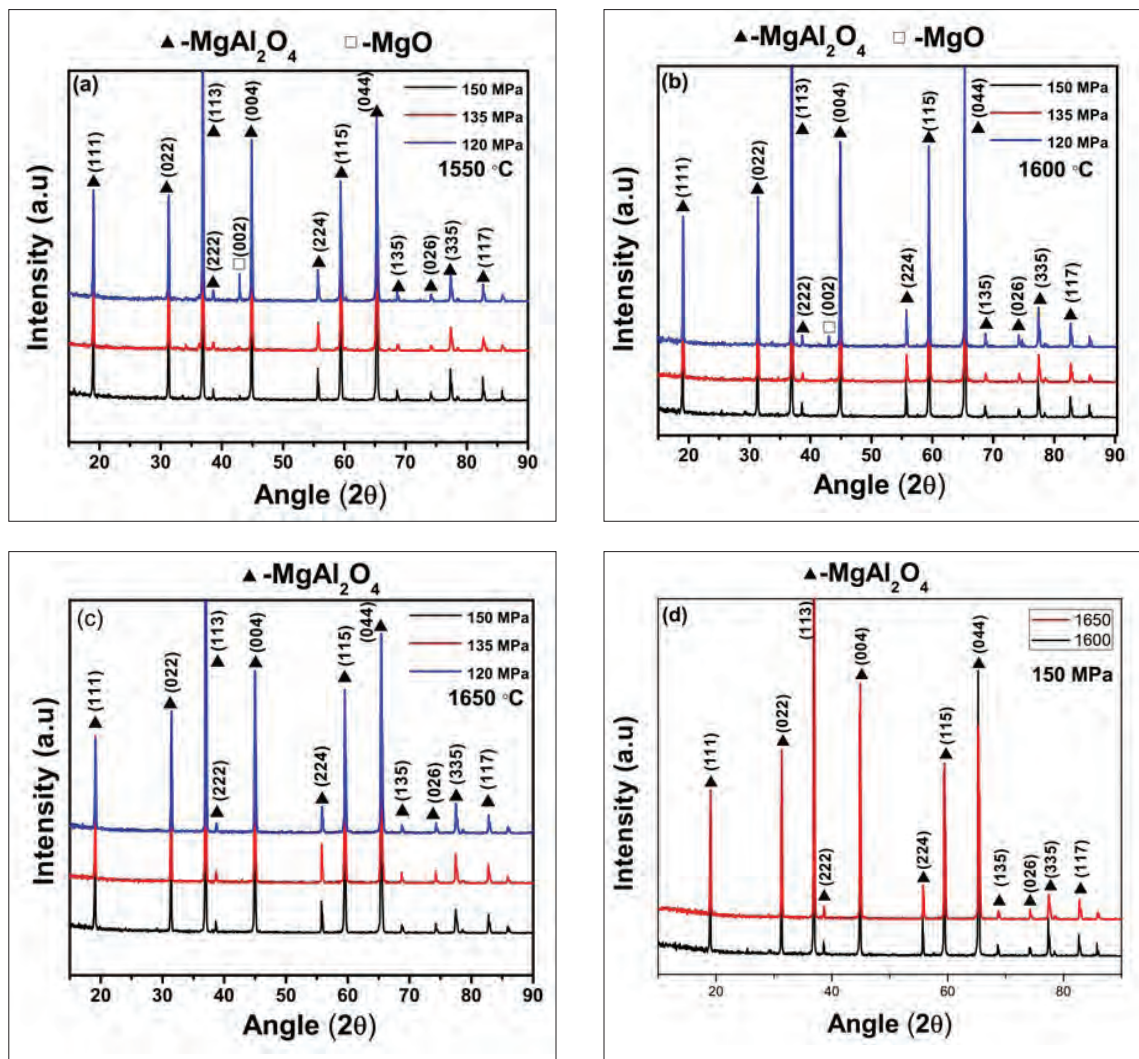


Figure 7: XRD plot of spinel formation (a) at 1550°C, (b) at 1600°, (c) at 1650°C and (d) at 150MPa pressure

3.5 Microstructure analysis

Mechanical properties depend on the microstructure of a material. Fig.8 indicates the microstructure of the sintered pellet at 1650°C. The polished and thermally etched samples observed under FESEM [19]. Some other authors

developed a similar microstructure in case of spinel formation from magnesia and alumina powders without any sintering aid or additive [14-15, 20, 26]. EDAX analysis reveals the presence of Al, Mg, and O in the polished sample (Fig.8c).

SYNTHESIS AND CHARACTERIZATION OF MAGNESIUM ALUMINATE ($MgAl_2O_4$) SPINEL THROUGH SOLID STATE PRESSURELESS SINTERING

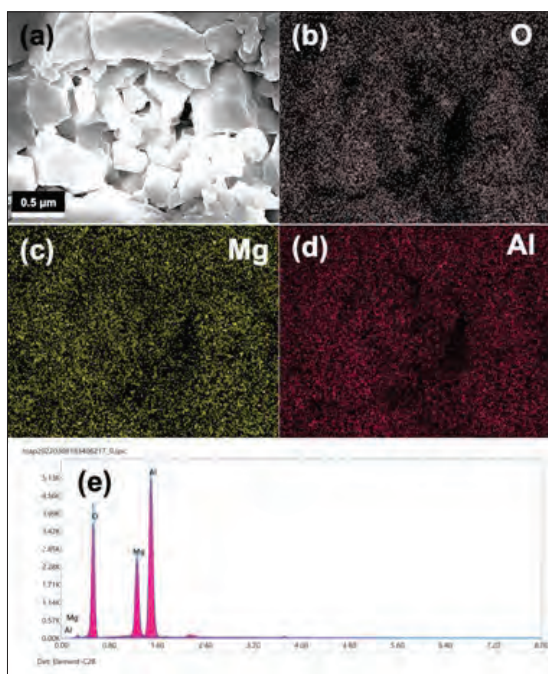


Figure 8: (a) FESEM Microstructure and elemental mapping of (b) O, (c) Mg, and (d) Al and (e) EDX spectrum of spinel ceramic sintered at 1650°C

4. Conclusion:

- Bulk density (BD), densification parameter and shrinkage increased and apparent porosity decreased by increasing the sintering temperature from 1550°C to 1650°C.
- Bulk density increased from 2.64 to 3.08 gm/cm³ by increasing the sintering temperature from 1550°C to 1650°C.
- The apparent porosity (AP) decreased from 18.81% to 6.09% by increasing the sintering temperature from 1550°C to 1650°C.
- Influence of compaction pressure on AP, BD, densification parameter and volume shrinkage is negligible compared to sintering temperature.
- XRD analyses reveal that MgO and Al₂O₃ have fully transformed into MgAl₂O₄ at

sintering temperature above 1550°C and compacted at above 135MPa.

Acknowledgements

The Field Emission Scanning Microscope (Ziss-Sigma) facility at the Center of Excellence in Advanced Materials of NIT Durgapur is duly acknowledged. The authors also express their sincere gratitude to technical personnel Mr. ShambhuSarkar at COE, NIT Durgapur. The authors are thankful to X-ray diffraction lab operator Mr. HiranmoyBairagya for capturing XRD data.

References

- [1] J Jeon, Y Kang, J H Park, Y Chung. Corrosion-erosion behaviour of $MgAl_2O_4$ spinel refractory in contact with high MnO slag, *Ceramics International*, 43(2017), 15074-15079.
- [2] S Tong, J Zhao, Y Zhang, Q Cui, R Wang, Y Lia. Corrosion mechanism of Al-MgO-MgAl₂O₄ refractories in RH refining furnace during production of rail steel, *Ceramics International*, 46(2020), 10089-10095.
- [3] L Musante, V Munoz, M H. Labadie, A G. T Martinez. High temperature mechanical behaviour of Al₂O₃-MgO-C refractories for steelmaking use, *Ceramics International*, 37(2011), 1473-1483.
- [4] I. Ganesh, S. Bhattacharjee, B.P. Saha, R. Johnson, K. Rajeshwari, R. Sengupta, M.V. R Rao, Y.R. Mahajana. An efficient $MgAl_2O_4$ spinel additive for improved slag erosion and penetration resistance of high-Al₂O₃ and MgO-C refractories, *Ceramics International* 28 (2002) 245-253.
- [5] Q Gu, F Zhao, X Liu, Q Jia. Preparation and thermal shock behaviour of nanoscale $MgAl_2O_4$ spinel toughened MgO-based refractory aggregates, *Ceramics International*, 45(2019), 12093-12100.
- [6] J G Li, T Ikegami, J H Lee, T Mori, Y Yajima. A wet chemical process yielding reactive magnesium aluminate spinel ($MgAl_2O_4$) powder, *Ceramics International* 27(2001) 481-489.
- [7] M.F. Zawrah, H. Hamaad, S. Meky. Synthesis and characterization of nano $MgAl_2O_4$ spinel by the

SYNTHESIS AND CHARACTERIZATION OF MAGNESIUM ALUMINATE (MgAl_2O_4) SPINEL THROUGH SOLID STATE PRESSURELESS SINTERING

- co-precipitated method, *Ceramics International* 33 (2007) 969-978.
- [8] H Zhang, X Jia, Z Liu, Zhenzh L. The low temperature preparation of nanocrystalline MgAl_2O_4 spinel by citrate sol-gel process, *Materials Letters* 58 (2004) 1625 - 1628.
- [9] K. Prabhakaran, D. S. Patil, R. Dayal, N. M. Gokhale, S. C. Sharma. Synthesis of nanocrystalline magnesium aluminate (MgAl_2O_4) spinel powder by the urea-formaldehyde polymer gel combustion route, *Materials Research Bulletin* 44 (2009) 613-618
- [10] Q Liu, Y Jing, S Su, X Li, X Liu, Y Feng, X Chen, J Li. Microstructure and properties of MgAl_2O_4 transparent ceramics fabricated by hot isostatic pressing, *Optical Materials*, 104(2020), 109938.
- [11] Y Liua, J Zhua, B Daia. Transparent MgAl_2O_4 ceramics prepared by microwave sintering and hot isostatic pressing, *Ceramics International*, 46(2020), 25738-25740.
- [12] Q.Y. Chen, C.M. Meng, T.C. Lu, X.H. Chang, G.F. Ji, L. Zhang, F. Zhao. Enhancement of sintering ability of magnesium aluminate spinel (MgAl_2O_4) ceramic nano-powder by shock compression, *Powder Technology* 200 (2010) 91-95.
- [13] I. Ganesh. A Review on Magnesium Aluminate (MgAl_2O_4) Spinel: Synthesis, Processing and Applications, *International Materials Reviews* 2013 VOL 58 NO 2.
- [14] C Ghosh, AGhosh, M K Haldar. Studies on densification, mechanical, micro-structural and structure-properties relationship of magnesium aluminate spinel refractory aggregates prepared from Indian magnesite, *Materials Characterization*, 99(2015) 84-91.
- [15] S K Mohan, R Sarkar. A comparative study on the effect of different additives on the formation and densification of magnesium aluminate spinel, *Ceramics International*, 42(2016), 13932-13943.
- [16] D. Mohapatra, D. Sarkar. Preparation of MgO - MgAl_2O_4 composite for refractory application, *Journal of Materials Processing Technology* 189 (2007) 279-283.
- [17] H.S. Tripathi, A. Ghosh. Spinelisation and properties of Al_2O_3 - MgAl_2O_4 -C refractory: Effect of MgO and Al_2O_3 reactants, *Ceramics International* 36 (2010) 1189-1192.
- [18] H. Reveron, D. Gutierrez-Camposa, R.M. Rodriguez, J.C. Bonassin. Chemical synthesis and thermal evolution of MgAl_2O_4 spinel precursor prepared from industrial gibbsite and magnesia powder, *Materials Letters* 56 (2002) 97 - 101.
- [19] Q Liu , Y Jing, S Su, X Li, X Liu, Y Feng, X Chen, J Li. Microstructure and properties of MgAl_2O_4 transparent ceramics fabricated by hot isostatic pressing, *Optical Materials* 104 (2020) 109938.
- [20] W Kim, F Saito. Effect of grinding on synthesis of MgAl_2O_4 spinel from a powder mixture of $\text{Mg}(\text{OH})_2$ and $\text{Al}(\text{OH})_3$, *Powder Technology* 113 2000 109-113.
- [21] S K Mohan, R Sarkar. Effect of ZrO_2 addition on MgAl_2O_4 spinel from commercial grade oxide reactants, *Ceramics International* 42 (2016) 10355-10365.
- [22] X Wang, Y Tian, J Hao, Y Wang, P Bai. Sintering mechanism and properties of MgAl_2O_4 - $\text{CaAl}_{12}\text{O}_{19}$ composites with ZnO addition, *Journal of the European Ceramic Society*, 40(2020), 6149-6154.
- [23] X Ren, B Ma, G Zhang, G Fu, J Yu, G Liu. Preparation and properties of MgAl_2O_4 spinel ceramics by double-doped Sm_2O_3 - $(\text{Y}_2\text{O}_3, \text{Nb}_2\text{O}_5$ and $\text{La}_2\text{O}_3)$, *Materials Chemistry and Physics*, 252(2020), 123309.
- [24] S Peddarasi, D Sarkar. Mechano-chemical effect on synthesis and sintering behaviour of MgAl_2O_4 spinel, *Materials Chemistry and Physics*, 262(2021), 124275.
- [25] I Ganesh, S M Olhero, AHRebello and J. M. F. Ferreiraw. Formation and Densification Behaviour of MgAl_2O_4 Spinel: The Influence of Processing Parameters, *J. Am. Ceram. Soc.*, 91 [6] 1905-1911 (2008)
- [26] A D Mazzoni, M A Sainz, A Caballero, E F Aglietti. Formation and sintering of spinels (MgAl_2O_4) in reducing atmospheres, *Materials Chemistry and Physics* 78 (2002) 30-37.
- [27] S Angappan, L J Berchmans, C O Augustin. Sintering behaviour of MgAl_2O_4 - a prospective anode material, *Materials Letters* 58 (2004) 2283 - 2289.

ASSESSMENT OF THE TRIBOLOGICAL BEHAVIOR OF A METALLIC TRIBOPAIR: LM25 ALLOY-Si₃N₄ COMPOSITES AGAINST EN 31 STEEL

Zeeshan Ahmad¹, Sabah Khan², Ronaldo Câmara Cozza³, Ramkumar Penchaliah⁴,
Vikas Verma^{*}

¹Research & Development Cell, R V Institute of Technology, Bijnor;
Dr. A.P.J. Abdul Kalam Technical University, Uttar Pradesh, India.

²Mechanical Engineering Department, Jamia Millia Islamia, New Delhi, India

³University Center of FEI – Educational Foundation of Ignatius “Priest Sabóia de Medeiros”
Department of Mechanical Engineering Av. Humberto de Alencar Castelo Branco,
São Bernardo do Campo, SP – Brazil

⁴Department of Mechanical Engineering, Indian Institute of Technology – IIT Madras, India.

*vikasverma.iitr@rediffmail.com

Abstract: In the present research work, tribological behavior of hard ceramic silicon nitride (Si₃N₄) reinforced aluminium alloy LM 25 based composites against EN 31 steel in ambient conditions at various loads (19.60-58.86 N) and sliding distances (1200-2400 m) on pin-on-disk test rig was investigated for commercial purpose of machine components. Three sets of composites were fabricated with 4 - 12% of silicon nitride by stir casting technique. SEM Micrographs revealed formation of a homogeneous α -aluminum dendrites network structure developed due to the super-cooling of casting during solidification. EDS showed increased content of hard silicon and nitrogen from 29.04-73.96% and 6.68-14.54% respectively with 4-12% reinforcement addition which led to high hardness. Increase in hardness from 58.02 to 63.70 BHN is observed with increase in reinforcement which led to reduction in wear by reducing the actual contact area during sliding whereas strength is reduced on addition of Si₃N₄. The wear resistance of composite is found greater with 12% Si₃N₄ reinforced composite with reduced wear at low sliding distance. Due to continuous sliding, wear debris embedded with the surface forming a layer which resulted in variation in coefficient of friction (COF). COF increased at a high rate up to 1800 m followed at a slow rate up to 2400m sliding distance with increase of normal load. SEM analysis of worn surfaces revealed removal of surface layer with generation of micro cracks with subsequent sliding in composites reinforced with 4% and 8% silicon nitride whereas ploughing mechanism is observed in composite with addition of 12% Si₃N₄. The linear increasing trend was observed in wear loss against the dissipated energy for the investigated composites.

Keywords: materials, alloy, composites, silicon nitride, wear

1. Introduction

The study of tribological behaviour has become increasingly important to enhance performance, efficiency, reliability, and reduce maintenance of interacting machine components in various industrial applications. Various tribological factors affect all mechanisms, machines, and equipment and it is estimated that approximately 70 % of mechanical failure occurs due to tribological aspects and about 23% of the world's

energy is consumed due to tribological contacts [1]. This reveals the necessity of tribological treatment in industry and saves a considerable amount of energy. So nowadays tribological research plays a key role in materials, energy, and environmental conservation. Tribological research development leads to the production of new lightweight materials, nano lubricants and coating to reduce friction and wear, thus enhancing the efficiency of interacting machine

ASSESSMENT OF THE TRIBOLOGICAL BEHAVIOR OF A METALLIC TRIBOPAIR: LM25 ALLOY-Si₃N₄ COMPOSITES AGAINST EN 31 STEEL

components. This emerges the necessity to develop new composite materials which have better properties. Last three decades, the demands of aluminium matrix composites (AMCs) increased in many industrial applications due to their improved overall properties. In aluminium matrix composites, Al-Si alloy plays an important role in automotive applications because of its good mechanical, thermal as well as tribological properties. These properties make Al-Si alloy proficient for its use in automotive applications such as piston, cylinder liner, wheel rims, etc. Among the materials of mechanical and tribological importance, hypoeutectic aluminium alloy LM 25 (Al-7Si- 0.35Mg) is also known as A356 from Al-Si-Mg system has received significant attention due to its good casting property, heat treatment, and mechanical properties [2-5]. The various studied have been revealed that properties of aluminium based composites significantly improved reinforced with hard ceramics particles [6-7]. Krishna et al. [8] investigated tribological properties of A356 alloy based composites reinforced with tungsten carbide up to weight percentage of 5% in step of 1%. Wear resistance of fabricated composites enhanced as compared to monolithic base alloy A356 upto weight percentage 4%, while there was no influence of tungsten carbide noted on the coefficient of friction. In another research, it was reported that coefficient of friction and wear resistance were much better in aluminium alloy A356 composites reinforced with silicon carbide as compared to composites reinforced with aluminium oxide [9]. The wear resistance of A356 based composites was significantly enhanced with the increase of hardness due to reinforcement of hard ceramic particles of silicon carbide. The wear resistance was greatly influenced by size as well as morphology transformation of eutectic silicon in fabricated composites. The presence of particle porosity clustering with the enrichment of silicon carbide played an important role in worsening the

wear behavior of fabricated composite [10]. Abbasipour et al. [11] examined the influence of fabrication techniques on tribological behavior of aluminium alloy A356 based composites. The tribological properties of fabricated composites were significantly improved as the fabrication techniques changed from fully liquid to semi-solid route. Shanmugaselvam et al. [12] reported tribological behaviour of LM 25 matrix alloy and hybrid composites reinforced with nanoparticles alumina and titanium bromide under no load and 10N loading condition. The results revealed that wear resistance greatly improved with the addition of nano hard particles and normal load influenced the wear resistance [12]. Suresh et al. [13] showed that the wear resistance of aluminium alloy LM 25 based composites was significantly enhanced with the hard ceramic reinforcement of boron carbide particles but with the addition of graphite in LM 25-boron carbide composite as hybrid reinforcement reduced the wear resistance of the composite. The addition of graphite particles offered solid lubrication to the composites and reduces the metal to metal contact. Yang et al. [14] studied the tribological properties of A356.2 composites reinforced with graphite as reinforcement percentage increased from 2% to 8% in step of 2%. In their study electroless copper coated on graphite particles incorporated in aluminium by compocasting method. The coefficient of friction, wear rate, wear debris and electrical resistance contact was evaluated with the variation of graphite content under different normal loads at 0.2, 0.3, and 0.4 Mpa and various sliding speeds as 0.13, 0.16, and 0.20 m/s. From the study, it was reported that aluminum-based composites reinforced with 4% and 6% graphite showed less friction and wear and were independent on the variation of normal load and sliding speed. As the graphite content increased the size of wear debris become smaller and lamellar graphite structure was found on the rest of the tribo layer. The tribological properties of aluminium alloy LM 25 significantly improved

ASSESSMENT OF THE TRIBOLOGICAL BEHAVIOR OF A METALLIC TRIBOPAIR: LM25 ALLOY-Si₃N₄ COMPOSITES AGAINST EN 31 STEEL

with the reinforcement of hard ceramic particles and these properties were affected by various factors such as fabrication technique, particles size, and weight percentage of reinforcement, particle porosity clustering, and microstructure of fabricated composites.

Silicon nitride is a non-oxide ceramic having a unique combination of material properties such as good chemical stability, excellent hardness and better resistance to wear [15], thus finding applications in roller and ball bearing [16]. Ahmad et al. [17] and Xiu et al.[18] showed an improved strength of aluminium-based composites incorporated by silicon nitride. The improvement in tribological properties of composites reinforcement with silicon nitride as compared to unreinforced matrix reported in many studies [19-22]. EN31 steel is a high carbon steel which offers high hardness and compressive strength and it is widely used in machine part application such as shaft, gears and bearings etc [23]. Various studies have been shown that tribological properties of LM 25 composites improved with the reinforcement of different hard ceramics particles but very little work found on the tribological properties of silicon nitride reinforcement aluminium based composites. This study focuses on tribological behaviour of aluminium alloy LM 25 based composites reinforced with silicon nitride and EN 31 tribopair at different normal load, sliding distances, and at constant velocity.

2. Research Methodology

The aluminium alloy LM 25 was used as base material and silicon nitride particles in the range of 100-150 μm were employed as reinforcement. The chemical composition of LM25 was evaluated by optical emission spectroscopy and presented in table 1 [24]. The composites were fabricated in three sets with reinforcement percentages as 4%, 8%, and 12% weight of silicon nitride particles by stir casting technique. The silicon nitride particles were preheated at 400°C in a muffle

furnace to remove moisture and increase surface reactivity. An electric resistance furnace with a stir mechanism is employed for the fabrication of composites. In starting, the furnace temperature was set up to 500°C and increased gradually up to 850°C, when LM 25 alloy was reached in a full molten state; it was stirred for 2 minutes to attain homogeneity. Further, the temperature of the heater was reduced to liquidus temperature as 620°C to bring LM 25 in a semi-solid state. The heat-treated silicon nitride and 1% magnesium as a wetting agent were mixed to semisolid LM 25 alloy. The reheating of the mixture was done until it reached in a molten state. The stirring was done at 300 rpm through a mechanical stir and the whole process of fabrication was carried out in a nitrogen environment to avoid oxidation. Finally, the molten mixture was poured into a cylindrical steel die and allowed to cool.

Table 1. Chemical composition of aluminium alloy LM 25

Chemical Composition (%)	Value	Chemical Composition (%)	Value
Si	6.49	Mn	0.32
Cu	0.18	V	13
Mg	0.072	Ti	0.143
Fe	0.432	Sn	0.046
Zn	0.056	Bi	0.005
Ni	0.073	Pb	0.103
Al	92.09		

The microstructural and tribological behavior of fabricated composites was evaluated. The microstructural studies were carried out on a scanning electron microscope (ZEISS Model), integrated with an EDS system to provide chemical analysis. The hardness of all developed composites was measured on Brinell hardness testing machine according to ASTM E10 standard. The pin on disc tribometer was used to investigate the effect of silicon nitride particles reinforced in LM 25 alloy on wear and friction characteristic of tribopair. The tribopair formed as LM 25 alloy and its based composites were used as a cylindrical pin of 12mm diameter and

ASSESSMENT OF THE TRIBOLOGICAL BEHAVIOR OF A METALLIC TRIBOPAIR: LM25 ALLOY-Si₃N₄ COMPOSITES AGAINST EN 31 STEEL

32 mm in length which was pressed against a disc made of EN 31 steel in size of 165 mm in diameter and 8 mm thick. ASTM G99 standard was used to evaluate wear properties under dry sliding conditions. The tests were performed at a constant sliding speed at 2.0 m/s and various normal loads as 19.6N, 38.24N, and 58.86 as well as at different sliding distances as 1200m, 1800m, and 2400m.

3. Results and Discussion

3.1. Scanning Electron Microscopy Results

SEM micrograph of casted LM 25 (Fig. 1(a)) observed the solution of aluminium and interdendritic network of aluminum-silicon eutectic. A homogeneous α -aluminium dendritic network structure is developed due to super-cooling of casting during solidification [17, 25]. Fig. 1(b)

shows SEM micrographs of LM25-4%wt. Si₃N₄ composite; light grey spots are observed as silicon nitride surrounded by dark grey as the matrix. The dispersion of silicon nitride particles is more uniform in a sample and no cluster of reinforcement is found. SEM micrograph (fig. 1(c)) of LM 25 composites reinforced with 8% silicon nitride exhibits dispersion of silicon nitride particles are more uniform in this sample and no cluster of reinforcement is observed. Fig. 1(d) shows SEM micrograph of LM 25 alloy reinforced with 12% silicon nitride indicating that the dispersion of Si₃N₄ particles is not uniform in this sample and a cluster of reinforcement can be observed. It is also seen that the concentration of reinforcement enhances as more grey spots can be noticed.

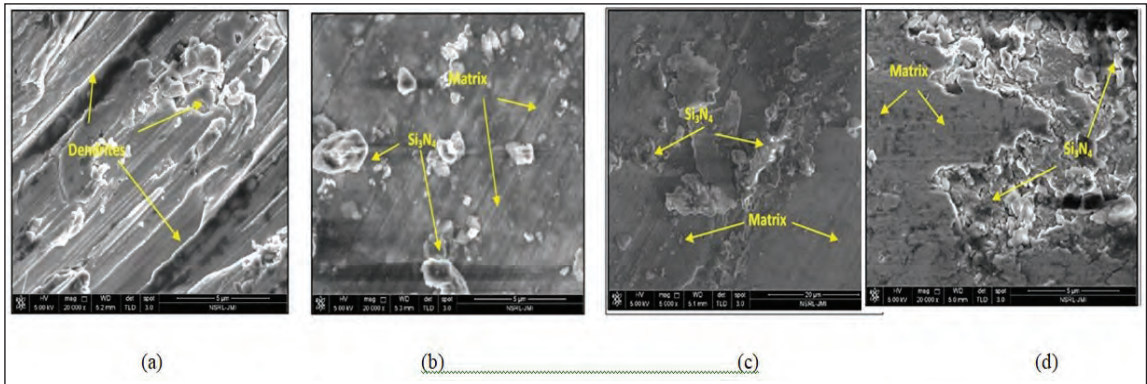


Fig. 1. SEM micrograph of casted LM 25 and developed composites

3.2. Energy dispersive spectroscopy results

The elemental peaks of aluminium and its based composites were identified by EDS (energy dispersive analysis) at various points, which reveal different peaks of various constituents. The study of the elemental peaks of various constituents showed the amount of different constituents present in the composites and their effect on mechanical and tribological properties. Fig. 2(a) showed the micrograph of

LM 25, which revealed various peaks of different constituents present in LM 25 and confirmed the presence of aluminium, copper, magnesium, and silicon. Fig. 2(b)-(c) showed the micrograph of aluminum-based composites reinforced with 4%, 8%, and 12% silicon nitride; which indicated that the concentration of hard silicon and nitrogen increased from 29.04-73.96 % and 6.68-14.54 respectively as the silicon nitride content increased 4-12%.

ASSESSMENT OF THE TRIBOLOGICAL BEHAVIOR OF A METALLIC TRIBOPAIR: LM25 ALLOY-Si₃N₄ COMPOSITES AGAINST EN 31 STEEL

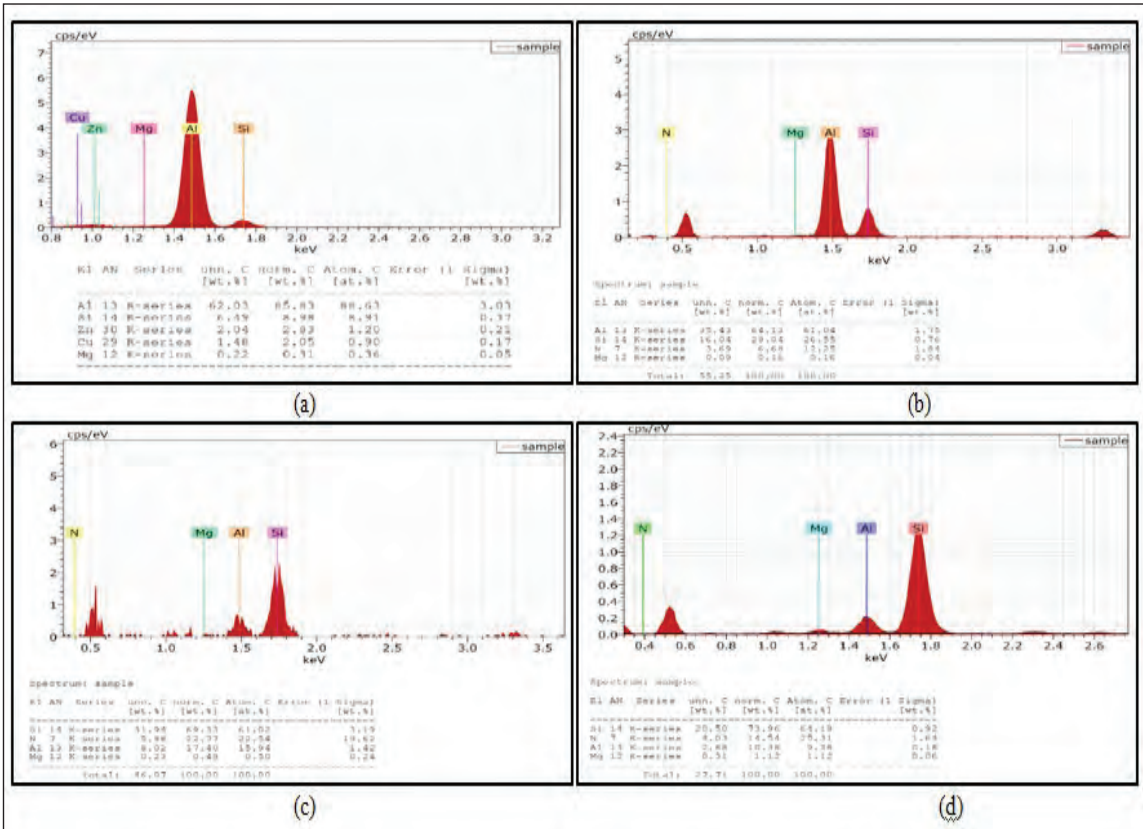


Fig. 2. EDS micrograph of casted LM 25 alloy and developed composites

3.3. Hardness results

The hardness test was performed at five different locations and the result shows in fig. 3 for LM 25 alloy and developed composites with various reinforcement of silicon nitride; the hardness of reinforced composite enhanced as the percentage concentration of reinforcement increased. The hardness for the composite reinforced with 4% increases as 5.55%, with 8% as 7.59%, and with 12% as 9.96%. The hardness of the developed composites enhanced as the percentage of reinforcement increased due to the existence of harder particles of silicon and nitrogen [26-27].

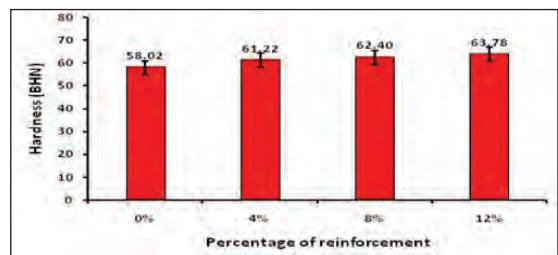


Fig. 3. Plot of the average hardness of casted LM 25 and all developed composites samples

3.4. Wear results

Fig. 4 (a-c) exhibited the variation of wear rate of unreinforced LM 25 alloy and developed composites with different sliding distances and

ASSESSMENT OF THE TRIBOLOGICAL BEHAVIOR OF A METALLIC TRIBOPAIR: LM25 ALLOY-Si₃N₄ COMPOSITES AGAINST EN 31 STEEL

under various loads with different reinforcement percentages. The wear results are plotted in terms of mass loss of the specimen with different sliding distances. From the graph it can be observed, that the wear rate rises for both alloy matrix as well as reinforced composite with the increase in sliding distance. It is also noticed that wear in the reinforced composite is much less than the matrix alloy and wear reduces as the reinforcement percentage increases, this can be due to the embedded silicon nitride that acts as a load-bearing element. The reduction in wear rate in composites may be due to the larger size and coarser particles of silicon nitride as it is tough to break down the longer dispersed particles. The wear rate of composites may be reduced due to the advantageous role of silicon nitride in increasing the hardness of composites as the hardness of materials mainly affected the wear rate. It is noticed that the variation of mass loss is high at a low sliding distance as wear debris got compacted with continuous sliding at higher sliding distance reducing wear loss. It is also observed that variation of mass loss for all composite samples is almost constant with the increases in sliding distance. Low percentage of Si₃N₄ addition (4%) has increased the hardness of the base alloy with negligible effect on wear. The mass loss of composites was reduced due to less contact area of the matrix as the increasing percentage of reinforcement reduced the contact of the area of matrix and hard particles of silicon nitride reduced the micro-cutting [28-33].

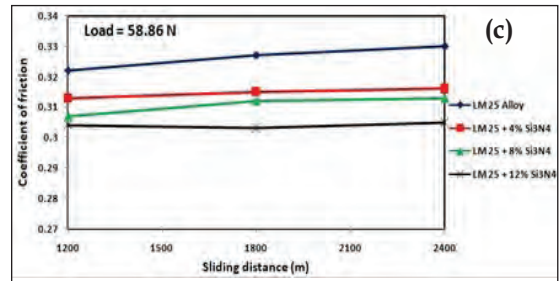
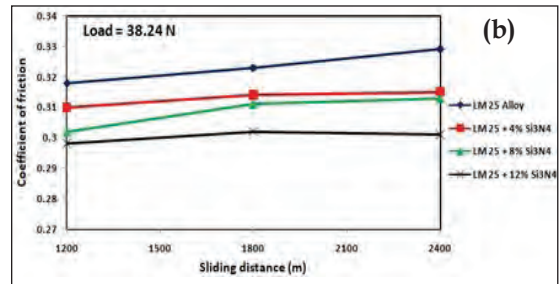
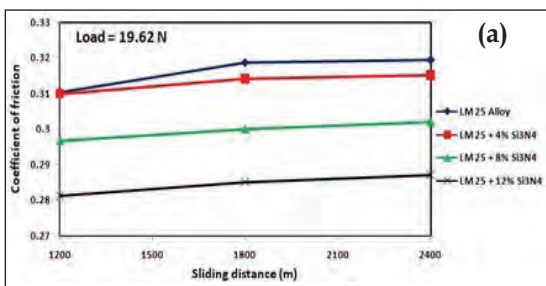


Fig. 5. Plots of coefficient of friction for casted LM 25 and developed composites vs sliding distance at constant sliding velocity and at different load (a); 19.62N, (b); 38.24N, (c); 58.84N

Fig. 5(a-c) shows the variation of coefficient of friction of casted LM 25 and developed composites with sliding distance under various loads with different reinforcement percentages. It is revealed in the graph that the coefficient of friction increases for both alloy LM 25 as well as reinforced composite with the increase in sliding distance. It is also observed that the coefficient of friction in the reinforced composite is less than the base alloy and the coefficient of friction reduces with the increase of reinforcement. It is noticed from the graphs that the variation in coefficient of friction increases in starting but becomes constant as the sliding distance increases. It is clear from the figure that the coefficient of friction increases with the sliding distance and attains a stable condition with further increases in sliding distance. The fact of the stable condition is that ridges and valleys are

ASSESSMENT OF THE TRIBOLOGICAL BEHAVIOR OF A METALLIC TRIBOPAIR: LM25 ALLOY-Si₃N₄ COMPOSITES AGAINST EN 31 STEEL

formed on the surface of the composite during the conducting of the wear test. These ridges and valleys are formed due to interface bonds between matrix and reinforcement particles but these ridges disappear and are annihilated by the wear debris within the sliding distance value. We can also observe that the coefficient of friction also decreases as the reinforcement percentage increases.

3.5. Scanning electron microscopy results of worn-out surface

Fig. 6(a) shows the worn-out surface of aluminum alloy LM25. The micrograph indicated abrasive wear as grooves formed parallel to the sliding direction. The wear mechanism can be observed as delamination in the cast aluminum alloy matrix, which may be because due to the presence of plate-like debris and surface fatigue. Fig. 6(b) shows the worn-out surface of aluminium alloy LM 25+4%wt. Si₃N₄ composites; delaminating

mechanism dominates along with the presence of narrow grooves; but fewer number grooves observed as compared to casted LM 25 sample. Fig. 6(c) shows worn-out surface of aluminium alloy LM 25+8%wt. Si₃N₄ composite also indicated micro cracks mechanism due to the presence of brittle silicon nitride particles with the occurrence of long narrow grooves in this aluminium alloy composite. Fig. 6(d) shows worn-out surface of aluminium alloy LM 25+12%wt. Si₃N₄; ploughing mechanism formed parallel to the sliding direction. It is revealed in the micrograph that delamination and ploughing mechanisms are predominant along with the presence of long narrow grooves in the aluminium alloy composites. However, the hard Si₃N₄ particulates improve the resistance of composite against plastic deformation and material flow thereby increasing the load-bearing capacity.

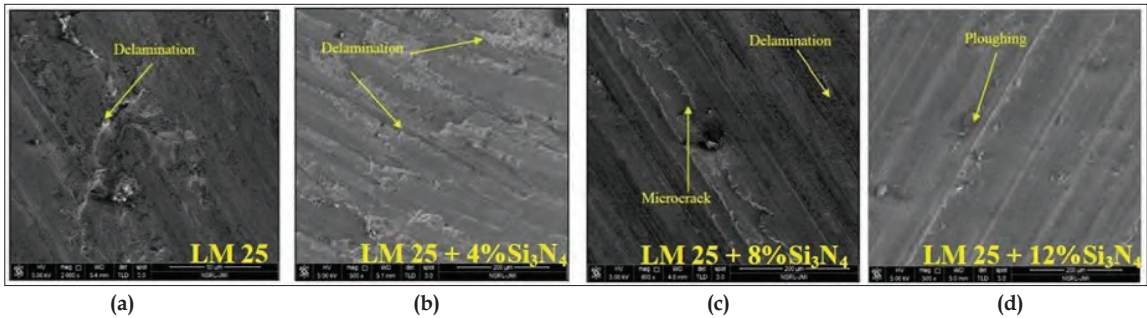


Fig. 6. SEM micrograph of worn surface of casted LM 25 and developed composites

3.6. Relationship between wear mass loss and energy dissipated

There is an increase in temperature at the mating surface of bodies when two bodies are move relative to each other and loss in generated energy in the form of deformation and wear. A study was done on the relation of wear and dissipated energy at different loading conditions

for all developed composites samples. The calculation of dissipated energy was done by using this relation as [34-37]:

$$E_d = \mu \times W \times v \times t$$

Where: E_d = Energy dissipated (J); μ = Avg. coefficient of friction; W = Normal load (N); v = sliding velocity (m/s); t = Time duration (s).

ASSESSMENT OF THE TRIBOLOGICAL BEHAVIOR OF A METALLIC TRIBOPAIR: LM25 ALLOY-Si₃N₄ COMPOSITES AGAINST EN 31 STEEL

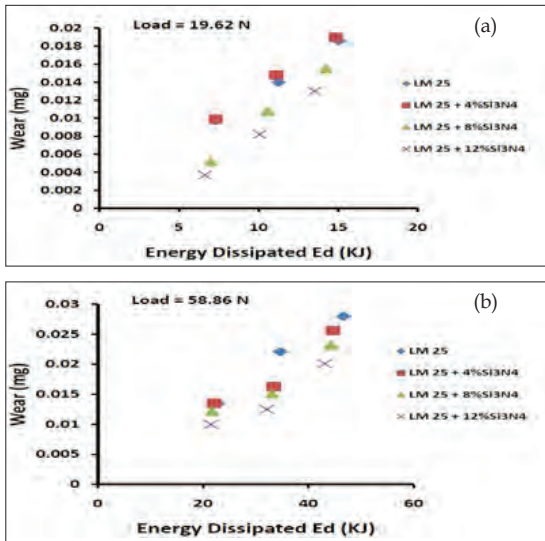


Fig. 7. Plot between wear and dissipated energy at different loads

Fig. 7 (a) & (b) demonstrated the linear correlation between the mass loss and energy dissipated for base alloy and all developed composites during sliding against EN 31 steel at different loads and change in dissipated energy enhanced with the increase in loads.

4. Conclusions

This present study investigated the wear behavior of silicon nitride reinforced aluminium alloy composites against EN 31 steel at the unlubricated condition and varying loads (19.6-58.86N load) and sliding distances (1200-2400m). Following are the major findings:

- Micro-structural analysis of LM 25 through scanning electron microscopy indicated homogeneous α -aluminum dendrites network structure developed due to the super-cooling of casting during solidification. Energy dispersive spectroscopy results revealed that the amount of hard silicon and nitrogen increased from 29.04-73.96 % and 6.68-14.54 respectively as the silicon nitride

content increased 4-12% which enhanced their wear resistance due to their hardness.

- The hardness of investigated composites enhanced from 5.55% to 9.96 % as the reinforcement increased as 4-12% as compared to the base alloy. This is attributed due to the existence of harder particles of silicon and nitrogen.
- The wear rate for both base alloy and investigated composites increased with the increase in sliding speed and normal loads. The wear resistance is observed less at low sliding distance as 1200 m and high at higher sliding as 2400 m. Best wear resistance showed with the 12% of silicon nitride reinforcement which may be due to hard particles of silicon nitride that act as load-bearing element.
- The Coefficient of friction for all composites reduced with the increase in reinforcement and the highest reduction was observed in composites reinforced with 12% silicon nitride. COF increased with the increase in sliding at the starting and become constant as the sliding distance increased for both alloy and investigated composites. This trend is observed in all loading conditions and the value of COF enhanced as the load increased. The stable value of COF may be ridges and valleys are formed due to interface bond between matrix and reinforcement particles but these ridges disappear are annihilated by the wear debris within the sliding distance value.
- The micrograph of worn-out surface indicated delamination mechanism with some microcracks in LM 25 alloy and composites reinforced with 4%, 8% and ploughing mechanism in composite reinforced with 12% silicon nitride.
- The study of dissipated energy related to wear showed an increasing trend for all

ASSESSMENT OF THE TRIBOLOGICAL BEHAVIOR OF A METALLIC TRIBOPAIR: LM25 ALLOY-Si₃N₄ COMPOSITES AGAINST EN 31 STEEL

composites at various loads and increased with increase in loads but the change in the amount of dissipated energy was very small for all composites siding against EN 31 steel.

References

- [1] Holmberg H, Erdemir A. Influence of tribology on global energy consumption, costs and emissions. *Friction*. 2017; 5(3):263-284. <https://doi.org/10.1007/s40544-017-0183-5>
- [2] Khan S, Ahmad Z. Comparative analysis for coefficient of friction of LM 25 alloy and Im 25 granite composite at different sliding speeds and applied pressure. *Int. J. Mech. Prod. Eng. Res. Dev.* 2018; 8(3):291-300.
- [3] Conley JG, Huang J, Asada J, Akiba, K. Modeling the effects of cooling rate, hydrogen content, grain modifier on microporosity formation in Al A356 alloys. *Mater. Sci. Eng. A*. 2000;285: 49-55. [https://doi.org/10.1016/S0921-5093\(00\)00665-1](https://doi.org/10.1016/S0921-5093(00)00665-1)
- [4] Dahle AK, Nogita K, Mcdonald SD, Dinnis C, Lu L. Eutectic modification and microstructure development in Al-Si alloys. *Mater. Sci. Eng. A*. 2005; 413-414:243-48. [https://doi.org/10.1016/S0921-5093\(00\)00665-1](https://doi.org/10.1016/S0921-5093(00)00665-1)
- [5] Ahmad Z, Khan S. A review paper on tribological and mechanical properties of aluminium matrix composites manufacture by different route. *Int. J. Sci. Eng. Res.* 2014; 1(4):1-8.
- [6] Macedo MM, Luna-Domínguez JH, Verma V, Schön CG, and Cozza, RC. Assessment of micro-abrasive wear tribological properties of H10 tool-steel under conditions of “constant normal force - variable pressure” and “constant pressure - variable normal force”. *Wear*, 2021; 476: 1-16. doi: 10.1016/j.wear.2021.203664
- [7] Verma V, Cheverikin V, Cozza, RC, Review: Effect on physical, mechanical, and wear performance of ZrB₂-based composites processed with or without additives, *Int. J. Appl. Ceram. Technol.* 2020; 17: 2509-32. <https://10.1111/ijac.13567>
- [8] Krishna AR, Aruna A, Unnikrishnana D, Shankarb KV. An investigation on the mechanical and tribological properties of alloy A356 on the addition of WC. *Mater. Today: Proc.* 2018; 5: 12349-55. <https://doi.org/10.1016/j.matpr.2018.02.213>
- [9] Vencla A, Bobicb I, Arosteguic S, Bobicb B, Marinkovi`Ca A, Babi`Ce M. Structural, mechanical and tribological properties of A356 aluminium alloy reinforced with Al₂O₃, SiC and SiC + graphite particles. *J. Alloys compd.* 2010; 506: 631-39. <https://doi.org/10.1016/j.jallcom.2010.07.028>
- [10] Ghandvar H, Idris MH, Ahmad N, Moslemi N. Microstructure development, mechanical and tribological properties of a semisolid A356/xSiCp composite. *J. Appl. Res. Technol.* 2017; 1-12. <https://doi.org/10.1016/j.jart.2017.06.002>
- [11] Abbasipour1 B, Niroumand B, Vaghefi1 SMM, Abedi M. Tribological behavior of A356-CNT nanocomposites fabricated by various casting techniques. *Trans. Nonferrous Met. Soc. China* 2019; 29: 1993-04. [https://doi.org/10.1016/S1003-6326\(19\)65107-1](https://doi.org/10.1016/S1003-6326(19)65107-1)
- [12] Shanmugaselvam P, Sivaraj S, Subash P. Investigating the Wear and Hardness of Aluminium LM25 Alloy Reinforced With Nano Al₂O₃ and Nano TiB₂. *Mater. Today: Proc* 2019; 16: 1130-36. <https://doi.org/10.1016/j.matpr.2019.05.205>
- [13] Suresha V, Vikrama P, Palanivelb R, Laubscherb RF. Mechanical and wear behavior of LM25 Aluminium matrix hybrid composite reinforced with Boron carbide, Graphite and Iron oxide. *Mater. Today: Proc* 2018; 5: 27852-60. <https://doi.org/10.1016/j.matpr.2018.10.023>
- [14] Yang JB, Lin CB, Wang TC, Chub HY. The tribological characteristics of A356.2Al alloy/Gr(p) composites. *Wear* 2004; 257: 941-52. <https://doi.org/10.1016/j.wear.2004.05.015>
- [15] Riley FL. Silicon nitride and related materials. *J. Am. Ceram. Soc.* 2000; 83: 245-65. doi. [org/10.1111/j.1151-2916.2000.tb01182.x](https://doi.org/10.1111/j.1151-2916.2000.tb01182.x)
- [16] Wang L, Snidle R, Gu L. Rolling contact silicon nitride bearing technology: a review of recent research. *Wear* 2000; 246: 159-73. [https://doi.org/10.1016/S0043-1648\(00\)00504-4](https://doi.org/10.1016/S0043-1648(00)00504-4)
- [17] Ahmad Z, Khan S, Hasan S. Microstructural characterization and evaluation of mechanical properties of silicon nitride reinforced LM 25 composite. *J. Mater. Res. Technol.* 2020; 9(4): 9129-35. <https://doi.org/10.1016/j.jmrt.2020.06.037>
- [18] Xiu ZY, Chen GQ, Wu GH, Yang WS, Liu YM. Effect of volume fraction on microstructure and

ASSESSMENT OF THE TRIBOLOGICAL BEHAVIOR OF A METALLIC TRIBOPAIR: LM25 ALLOY-Si₃N₄ COMPOSITES AGAINST EN 31 STEEL

- mechanical properties of Si₃N₄/Al composites. *Trans. Nonferrous Met. Soc. China* 2011; 21: 285-89. [https://doi.org/10.1016/S1003-6326\(11\)61592-6](https://doi.org/10.1016/S1003-6326(11)61592-6)
- [19] Sharma N, Khanna R, Singh G, Kumar V. Fabrication of 6061 aluminum alloy reinforced with Si₃N₄/n-Gr and its wear performance optimization using integrated RSM-GA. *Part. Sci. Technol.* 2016; 1-11. <https://doi.org/10.1080/02726351.2016.1196276>
- [20] Suryanarayana RC, Khan S, Koppad PG, Khan Z. Tribological behaviour of hot extruded Al6061-Si₃N₄ composite. Conference: ASME 2013 International Mechanical Engineering Congress and Exposition: San Diego, California, USA, 2013.
- [21] Arik H. Effect of mechanical alloying process on mechanical properties of a-Si₃N₄ reinforced aluminum-based composite materials. *Mater. Des.* 2008; 29: 1856-61. <http://dx.doi.org/10.1016/j.matdes.2008.03.010>
- [22] Cambronero LEG, Sanchez E, Ruiz-Roman J, Ruiz-Prieto JM. Mechanical characterisation of AA7015 aluminium alloy reinforced with ceramics. *J. Mater. Process. Technol.* 2003;143-144:378-83. [https://doi.org/10.1016/S0924-0136\(03\)00424-2](https://doi.org/10.1016/S0924-0136(03)00424-2)
- [23] Baburaj A, Chaudhary KBSS, Khatirkar K, Sapate SG. Abrasive Wear Behaviour of Heat Treated EN31 Steel. *ISIJ International.* 2013;53(8):1471-78.
- [24] Ahmad Z, Jafri HZ, Basha RH. Characterization technique for composites using AI and machine learning techniques. In: Tayal S, Nandi P, Nandil A, Davim JP, editors. *Computational Technologies in Material Science*, Boca Raton: CRC Press; 2021, p. 139-68. <http://dx.doi.org/10.1201/9781003121954-7>
- [25] Ahmad Z, Khan S. Mechanical characterization of LM25 alloy matrix composite reinforced with boron carbide. *J Compos Mater.* 2021; 55(22): 3151-58. DOI: 10.1177/00219983211005513
- [26] Hamid AA, Ghosh PK, Jain SC, Roy S. The influence of porosity and particles content on dry sliding wear of cast in situ Al (Ti)-Al₂O₃ (TiO₂) composite. *Wear* 2008; 265: 14-26. <http://dx.doi.org/10.1016/j.wear.2007.08.018>
- [27] Hamid AA, Ghosh PK, Jain SC, Roy S. Influence of particle content and porosity on the wear behaviour of cast in situ Al (Mn)-Al₂O₃(MnO₂) composite. *Wear* 2006; 260: 368-78. <https://doi.org/10.1016/j.wear.2005.02.120>
- [28] Kok M. Abrasive wear of Al₂O₃ particle reinforced 2024 aluminium alloy composites fabricated by vortex method. *Compos. - A: Appl. Sci. Manuf.* 2006; 37: 457-64. <https://doi.org/10.1016/j.compositesa.2005.05.038>
- [29] Alpas AT, Hu H, Zhang J. Plastic deformation and damage accumulation below the worn surfaces. *Wear*1993; 162: 188-95. [https://doi.org/10.1016/0043-1648\(93\)90500-L](https://doi.org/10.1016/0043-1648(93)90500-L)
- [30] Suresh KR, Niranjana HB, Jebaraj PM. Tensile and wear properties of aluminium composites. *Wear* 2003; 255: 638-42. [http://dx.doi.org/10.1016/S0043-1648\(03\)00292-8](http://dx.doi.org/10.1016/S0043-1648(03)00292-8)
- [31] Das S, Das S, Das K. Abrasive wear of zircon sand and alumina reinforced Al 4.5 wt% Cu alloy matrix composites—a comparative study. *Compos Sci Technol* 2007; 67:651-46. <http://dx.doi.org/10.1016/j.compscitech.2006.05.001>
- [32] Tjong SC, Lau KC. Abrasive wear behavior of TiB₂particle-reinforced copper matrix composites. *Mater. Sci. Eng. C* 2000; 282: 183-86. [https://doi.org/10.1016/S0921-5093\(99\)00752-2](https://doi.org/10.1016/S0921-5093(99)00752-2)
- [33] Canakci A, Arslan F. Abrasive wear behaviour of B₄C particle reinforced Al2024 MMCs. *Int. J. Adv. Manuf. Technol* 2013; 63: 785-95. <https://doi.org/10.1007/s00170-012-3931-8>
- [34] Verma V, Cozza RC, Cheverikin V, Kondratiev A, Penchaliah R. Mechanical and tribological behavior of Al composites containing varying beryllium aluminum silicate and constant CeO₂. *SN Appl. Sci.* 2021; 3: 821. <https://doi.org/10.1007/s42452-021-04790-3>
- [35] Marui E, Hashimoto M, Kato S, Kojima W. Dissipation of kinematic energy by slip at the interface of mating surfaces. *Wear* 1992; 159(1): 141-150. [https://doi.org/10.1016/0043-1648\(92\)90296-K](https://doi.org/10.1016/0043-1648(92)90296-K)
- [36] Huq, MZ Celis JP. Reproducibility of friction and wear results in ball-on-disc unidirectional sliding tests of TiN-alumina pairings. *Wear* 1997; 212(2): 151-159. [https://doi.org/10.1016/S0043-1648\(97\)00167-1](https://doi.org/10.1016/S0043-1648(97)00167-1)
- [37] Czichos H, Klaffke D, Santner, Woydt M. Advances in tribology: the materials point of view. *Wear* 1995; 190(2): 155-161. [https://doi.org/10.1016/0043-1648\(96\)80016-7](https://doi.org/10.1016/0043-1648(96)80016-7)

SYNTHESIS OF NANOSTRUCTURED EQUIATOMIC TiCrFeCoNi HIGH-ENTROPY ALLOY BY MECHANICAL ALLOYING AND CONVENTIONAL SINTERING

Vikas Shivam ^{a*}, Vadapalli Sanjana ^b, Yagnesh Shadangi ^b, V.C. Srivastava ^a and N.K. Mukhopadhyay ^b

^aMaterials Engineering Division, CSIR-National Metallurgical Laboratory, Jamshedpur, India
^bDepartment of Metallurgical Engineering, Indian Institute of Technology (BHU), Varanasi, India
*E-mail: vikas.rs.met13@itbhu.ac.in

Abstract: An equiatomic TiCrFeCoNi high-entropy alloy (HEA) was synthesized by mechanical alloying (MA) of elemental powders. The alloying behaviour of the milled powder, in terms of phase constitution, was analysed by X-ray diffraction studies. The powder obtained after 30 h of milling shows the formation of a BCC matrix phase ($a = 2.88 \pm 0.01 \text{ \AA}$) co-existing with CoTi_2 intermetallic phase ($a = 11.297 \text{ \AA}$, Pearson symbol- cF96). The powder morphology and size distribution of 30 h milled powder was investigated by scanning electron microscopy (SEM). The milled powder of nanostructured nature was confirmed through transmission electron microscopy (TEM). The conventional sintering of the powder at 1473 K for 24 h showed the transformation of the metastable BCC phase into the FCC ($a = 3.58 \pm 0.01 \text{ \AA}$) phase along with the CoTi_2 ($a = 11.297 \text{ \AA}$, Pearson symbol- cF96) and Co-Cr type sigma phase. The proposed phase selection rules i.e., valance electron concentration and high mixing entropy does not follow the experimental results for selected composition.

Keywords: Mechanical alloying; High-entropy alloys; Conventional sintering; Solid solution;

1. Introduction

The last two decades have witnessed significant scientific activities in developing high entropy alloys (HEAs) with promising applications. These alloys are stated to have a minimum of 5 elements in equiatomic or non-equiatomic proportion with the composition range of 5-35 at % [1-3]. The high configurational entropy of these alloys is the crucial factor that stabilizes the alloys to form a simple solid solutions structures of body-centered cubic (BCC), face-centered cubic (FCC), and hexagonal closed packed (HCP) rather than complex phases[4]. HEAs have shown exciting properties, like high strength and hardness, enhanced thermal stability, superior oxidation and corrosion resistance, etc. [5,6]. These attributes of HEAs have led to a fundamental curiosity to explore the possible discovery of new alloys / alloy systems in the ensued high dimensional compositional space. HEAs have been synthesized by different

processing routes, i.e., melting/casting, powder metallurgy, rapid solidification and deposition techniques [7-9]. So far, the majority of the HEAs have been synthesized by melting/ casting route compared to the powder metallurgy [10-12]. Materials synthesis by mechanical alloying (MA) is an established technique to produce homogenous nanostructured powder with the virtue of extended solid solubility for immiscible systems [13-15]. However, the major challenge involved with the mechanical alloying route is the consolidation of the milled powder. The spark plasma sintering (SPS) as well as various hot pressing processes have been utilized to consolidate these powders into bulk nano-crystalline materials. Although, SPS offers better mechanical properties [16,17], the commercial viability and economics associated with the process are still limiting the widespread application of SPS [18]. The pressureless and cost-effective sintering approach is less explored

SYNTHESIS OF NANOSTRUCTURED EQUIATOMIC TiCrFeCoNi HIGH-ENTROPY ALLOY BY MECHANICAL ALLOYING AND CONVENTIONAL SINTERING

for the HEAs. Kumar et al.[19] synthesized $Al_xFe_{1.5}CrMnNi_{0.5}$ HEA through mechanical alloying followed by conventional sintering at 800° C for 2 h, in vacuum and air for two different compositions of Al ($x=0.3$, and 0.5) . They reported increased in mechanical properties, i.e., hardness and yield strength with improved density. Varalakshmi et al. [20] investigated the hot consolidation effect on mechanical properties of equiatomic AlFeTiCrZnCu HEA synthesized by mechanical alloying. The consolidation of the milled powder was done by following three techniques, i.e., conventional sintering, vacuum hot pressing and hot isostatic pressing. Their results showed the presence of similar phases, i.e., two BCC and FCC in all the differently consolidated samples. However, hot isostatic pressed samples showed increased hardness and compressive strength compared to the hot-pressed samples. In the present investigation, therefore, an equiatomic TiCrFeCoNi HEA, with two BCC, two HCP and one FCC element, was synthesized by mechanical alloying and sintered through the pressureless conventional sintering. The alloy gives rise to high hardness due to presence of intermetallic phases and better corrosion and wear resistance. This makes the alloy system an excellent coating material for critical applications e.g. high temperature and corrosive environment. CoCrFeNi is the most commonly used and well-studied composition with the effect of other alloying elements likes Al, Mn, Si, Cu etc. The addition of Ti, having a higher atomic radius has not been explored much through mechanical alloying. The work mainly emphasizes the systematic study of phase evolution during milling and sintering of the elemental powders with varied crystal structures and enthalpy of solution formation. The evolved phases are correlated with the thermodynamic phase prediction. This study on the non-equilibrium nano-crystallization and high temperature sintering behavior would help to understand the phase evolution through

the processes and pave the way for further developments on applications front.

2. Experimental details

The elemental powders of Ti, Cr, Fe, Co and Ni of average particle sizes of 45 μ m (purity, \geq 99%) were used for the synthesis of an alloy. The powder mixture in the equiatomic proportion of all the constituent elements was prepared and milled in a high-energy planetary ball mill (Retsch PM400). The vials and balls (dia. 10 mm) made of tungsten carbide were utilized by marinating the ball to powder ratio of 10:1. Milling was performed in the wet atmosphere, using toluene (C_7H_8) as a process control agent (PCA), to prevent overheating and oxidation of the powder. Initially, the powder was collected after 10 min of milling to verify the constituent elements and then extracted at a regular interval of 5h. The machine was stopped for 10-15 minutes after every hour of milling for safety of operation. The analysis of phase constitution as well as structural and microstructural characterizations were conducted by X-ray diffraction (XRD), (Rigaku Mini flex-600 (40 kV-15 mA)), with Cu-K α radiation ($\lambda= 0.154$ nm), scanning electron microscopy (SEM), (Zeiss EVO 18) operating at 30 kV, and transmission electron microscopy (TEM TECNAI G² T20) operated at 200 kV. The average crystallite size and lattice strain of the milled TiCrFeCoNi HEA powder was determined by voigt fitting of the major peaks, using the Williamson-Hall method. The milled powder was further consolidated through conventional sintering by encapsulating the green pellet in the vacuum quartz tube. The green pellets of 30 h milled powder were made using the steel die of 10 mm diameter under the normal load of 5 tonne, using a uniaxial hydraulic press of 30-tonne capacity. The quartz tube was kept inside the furnace at 1200°C (1273 K) with a holding time of 24 h. The phase evolution study in sintered samples was carried out through XRD analysis.

SYNTHESIS OF NANOSTRUCTURED EQUIATOMIC TiCrFeCoNi HIGH-ENTROPY ALLOY BY MECHANICAL ALLOYING AND CONVENTIONAL SINTERING

3. Results and discussion

The X-ray diffraction (XRD) patterns of the milled TiCrFeCoNi HEA powder for different durations are displayed in figure 1. The diffraction pattern of the powder collected after 10 min of milling shows the peaks corresponding to all the constituent elements. Even as milling proceeded up to 5 h, the diffraction peaks corresponding to all the elements could be observed though with a decrease in intensity and increase in peak broadening. Similar observations were made in the next 5 h of milling. The diffraction pattern of the sample milled for 15 h indicates the disappearance of the few peaks of elements Ti and Co, which suggested commencement of alloying. With increase in milling time for further upto 20 h, the formation of a major BCC along with the CoTi_2 type Laves phase could be observed. Milling was continued up to 30h to understand if any further phase transformation would happen. However, no change in the phase constitution was observed. The final hour milled sample shows the formation of the major BCC phase ($a = 2.88 \pm 0.01 \text{ \AA}$) along with the CoTi_2 ($a = 11.297 \text{ \AA}$, Pearson symbol- cF96) intermetallic phase. The intermetallic phase formation is related to the high negative mixing enthalpy of the Co-Ti binary pair. Table 1 shows the binary mixing enthalpy of equiatomic pairs by following the Miedema's approach [21]. The variation of crystallite size and lattice strain with milling time is given in figure 1(b). As the milling time increases, crystallite size decreases with an increase in the lattice strain. The crystallite size of $\sim 13 \text{ nm}$ was observed in the sample milled for 30 h. Figure 2a depicts the representative SEM micrograph of the 30 h milled powder sample. The flaky natures of the particles are due to the heavy deformation, fracturing and cold working induced during the milling operation. The remanence of the river like patterns could also be observed in some of the particle's surfaces (marked with an arrow), indicating the heavy deformation. The

powder particles in the size range of $\sim 1\text{-}3 \mu\text{m}$ could be observed. The bigger particles are due to the agglomeration of the particles. Figure 2 (b) showed the comparative elemental plots of atomic percentages of nominal and experimental values. The experimental values are taken from the SEM-EDS analysis. The high values of Fe and Ti corroborates the formation of BCC and CoTi_2 phases in the as-milled condition. The nano-crystalline nature of the milled powder was confirmed through TEM analysis. Bright field image (BF) and corresponding selected area diffraction (SAD) pattern of 30 h milled powder is given in figure 3. The formation of rings in the SAD pattern illustrates that the crystallites are randomly orientated and having the nano-crystalline nature. Particles of varying sizes ($\sim 10\text{-}50 \mu\text{m}$) could be observed in the bright field image. The dark field image shows the diffracted crystal of sizes $\sim 15 \text{ nm}$, which further corroborates the XRD data.

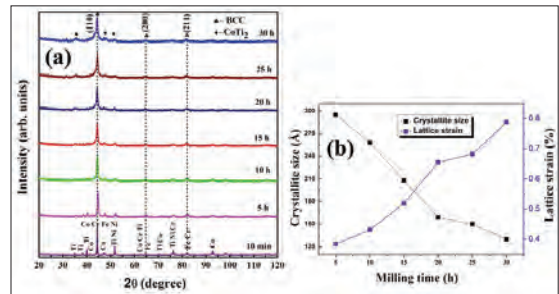


Figure 1. (a) XRD patterns of TiCrFeCoNi HEA powder milled for 30h. The formation of the major BCC phase along with the CoTi_2 phase could be discerned (b) variation of crystallite size and lattice strain as a function of milling time.

Elements	Ti	Cr	Fe	Co	Ni
Ti	-	-8	-17	-28	-35
Cr	-8	-	-2	-5	-7
Fe	-17	-2	-	-1	-2
Co	-28	-5	-1	-	0
Ni	-35	-7	-2	0	-

Table 1: The binary mixing enthalpy (ΔH_{mix}) of equiatomic alloys calculated using Miedema's approach.

SYNTHESIS OF NANOSTRUCTURED EQUIATOMIC TiCrFeCoNi HIGH-ENTROPY ALLOY BY MECHANICAL ALLOYING AND CONVENTIONAL SINTERING

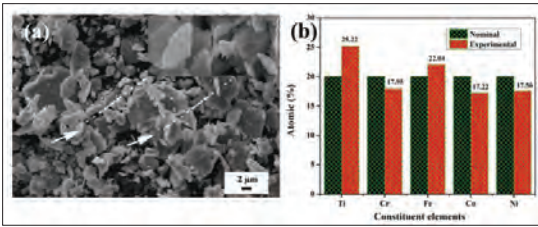


Figure 2:- (a) The representative SEM micrograph of 30h milled TiCrFeCoNi HEA powder showing powders in the size range of 1-3 μm . (b) comparative elemental plots of atomic concentration of constituent elements in nominal and experimental form.

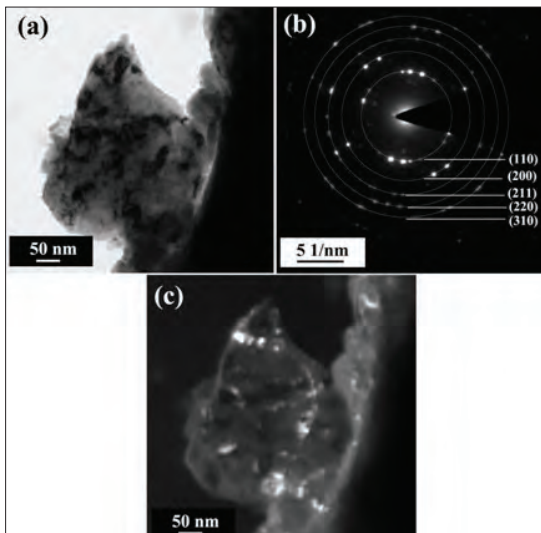


Figure 3:- (a) TEM bright-field electron micrograph of 30 h milled powder (b) corresponding selected area diffraction pattern (c) dark-field image.

Table 2: The calculated values of parameters ΔS^{mix} , ΔH^{mix} , δ and VEC of TiCrFeCoNi HEA.

Mixing entropy (ΔS_{mix}) (J/mol-K)	Mixing enthalpy (ΔH_{mix}) (kJ/mol)	Atomic size difference (%) (δ)	Valence electron concentration (VEC)
13.38	-16.32	6.68	7.4

The green pellet of powder, milled for 30 h, was encapsulated in the quartz tube backfilled with argon and conventionally sintered at 1200°C for 24 h in the muffle furnace. Figure 4 shows the

X-ray diffraction pattern of the sintered pellet. The transformation of the metastable BCC phase into the FCC phase was observed, along with the evolution of Co-Cr sigma ($a=b= 8.753\text{\AA}$, $c= 4.531\text{\AA}$, PDF no-01-080-8334) and CoTi_2 ($a= 11.297 \text{\AA}$, Pearson symbol- cF96) phases. The formation of the CoTi_2 intermetallic phase could be related to the high negative mixing enthalpy of Co and Ni with Ti and promotes the intermetallic formation. Shun et al.[22] have investigated the effect of Ti addition in CoCrFeNi HEA on microstructural evolution. On varying the concentration of Ti from 0, 0.3, and 0.5 molar volume, the alloy has shown the change in phase evolution from single-phase FCC structure to mixed phases. The formation of FCC, sigma and Laves phases were observed in $\text{CoCrFeNiTi}_{0.5}$ HEA. The changes in structure from FCC to mixed phases were ascribed to the larger atomic radius of Ti (1.47\AA) among other alloying elements. The addition of elements with large atomic radius (e.g. Ti) creates more lattice distortion and may improve the mechanical properties. Zhang et al. [23] have reported a similar observation of forming FCC, BCC and CoTi_2 phases in the as-cast structure.

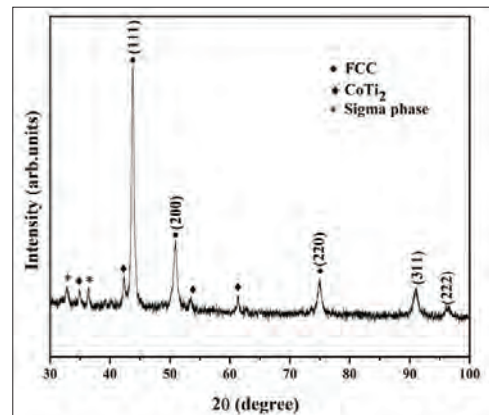


Figure 4:- X-ray diffraction pattern of TiCrFeCoNi HEA conventionally sintered at 1200°C (1473 K) for 24 in the controlled atmosphere. The evolution of the major FCC phase along with CoTi_2 and Co-Cr intermetallic phases could be discerned.

SYNTHESIS OF NANOSTRUCTURED EQUIATOMIC TiCrFeCoNi HIGH-ENTROPY ALLOY BY MECHANICAL ALLOYING AND CONVENTIONAL SINTERING

To establish a better correlation of the evolved phase in the as-milled and sintered conditions, thermodynamic parameters, i.e., mixing entropy (ΔS_{conf}), atomic size difference (δ), mixing enthalpy (ΔH_{mix}) and valence electron concentration [24,25], were calculated for the experimentally observed alloy composition. The calculated values are shown in Table 2. The alloy fulfils the requisite criteria required for the solid solution formation, i.e., mixing entropy of 1.61R, where R is the universal gas constant and atomic size difference (%) of 6.68. It has been reported that the VEC parameter could be used to predict the type of phases formed [26]. If $VEC > 8$, the formation of FCC phase is favored, and if $VEC < 6.87$, the BCC phase is dominant. If $6.87 < VEC < 8$, the formation of a mixture of FCC and BCC phases is favored [27]. The calculated VEC value of the studied TiCrFeCoNi HEA is 7.4, indicating the possible formation of a mixed FCC + BCC phase. The prediction based on VEC parameter is in contradiction with experimental results and requires further investigation. Based on the microstructural evolution, as compared with other studies on the similar alloy, it seems that as-milled nanocrystalline powder may find applications in the development high temperature corrosion resistant coatings with high hardness.

4. Conclusions

The equiatomic TiCrFeCoNi HEA was successfully synthesized by mechanical alloying. The alloy showed the formation of a major BCC phase ($a = 2.88 \pm 0.01 \text{ \AA}$) along with a CoTi₂ type intermetallic phase in the as-milled condition. The nano-crystalline nature of the milled powder was confirmed through the TEM analysis. The sintered sample (at 1200°C for 24 h) showed a phase transformation from metastable BCC phase into the FCC ($a = 3.58 \pm 0.01 \text{ \AA}$), sigma ($a = b = 8.753 \text{ \AA}$, $c = 4.531 \text{ \AA}$) and CoTi₂ ($a = 11.297 \text{ \AA}$, Pearson symbol- cF96) phases. The formation of multiphase structure in the as-milled and

sintered product deviates the alloy from the concept of high entropy alloy which leads to the formation simple structures. The proposed VEC criterion of phase selection does not obey the experimental findings and needs to be investigated in more details.

Acknowledgements: - The authors are grateful to Professor R.K. Mandal and Dr Joysurya Basu for many useful discussions during this investigation. One of the authors (VS) would like to acknowledge Science and Engineering Research Board (SERB), Department of Science and Technology (DST), the Government of India, for providing financial support through a National Post-Doctoral Fellowship (PDF/2021/001657).

References

- [1] J.W. Yeh, S.K. Chen, S.J. Lin, J.Y. Gan, T.S. Chin, T.T. Shun, C.H. Tsau, S.Y. Chang, Nanostructured high-entropy alloys with multiple principal elements: Novel alloy design concepts and outcomes, *Adv. Eng. Mater.* 6 (2004) 299–303. <https://doi.org/10.1002/adem.200300567>.
- [2] B. Cantor, I.T.H. Chang, P. Knight, A.J.B. Vincent, Microstructural development in equiatomic multicomponent alloys, *Mater. Sci. Eng. A.* 375–377 (2004) 213–218. <https://doi.org/10.1016/j.msea.2003.10.257>.
- [3] B. S. Murty, J.W. Yeh, S. Ranganathan, High Entropy Alloy, 2014. <https://doi.org/10.1016/B978-0-08-043152-9.02274-0>.
- [4] E.J. Pickering, N.G. Jones, High-entropy alloys: a critical assessment of their founding principles and future prospects, *Int. Mater. Rev.* 61 (2016) 183–202. <https://doi.org/10.1080/09506608.2016.1180020>.
- [5] Y. Zou, J.M. Wheeler, H. Ma, P. Okle, R. Spolenak, Nanocrystalline High-Entropy Alloys: A New Paradigm in High-Temperature Strength and Stability, *Nano Lett.* 17 (2017) 1569–1574. <https://doi.org/10.1021/acs.nanolett.6b04716>.
- [6] Y. Zhang, T. Ting, Z. Tang, M.C. Gao, K.A. Dahmen, P.K. Liaw, Z. Ping, Progress in Materials Science Microstructures and properties of high-entropy alloys, 61 (2014) 1–93.

SYNTHESIS OF NANOSTRUCTURED EQUIATOMIC TiCrFeCoNi HIGH-ENTROPY ALLOY BY MECHANICAL ALLOYING AND CONVENTIONAL SINTERING

- [7] V.C. Srivastava, G.K. Mandal, N. Ciftci, V. Uhlenwinkel, L. Mädler, Processing of High-Entropy AlCoCr_{0.75}Cu_{0.5}FeNi Alloy by Spray Forming, *J. Mater. Eng. Perform.* 26 (2017) 5906–5920. <https://doi.org/10.1007/s11665-017-3071-2>.
- [8] T.P. Yadav, S. Mukhopadhyay, S.S. Mishra, N.K. Mukhopadhyay, O.N. Srivastava, Synthesis of a single phase of high-entropy Laves intermetallics in the Ti-Zr-V-Cr-Ni equiatomic alloy, *Philos. Mag. Lett.* 97 (2017) 494–503. <https://doi.org/10.1080/09500839.2017.1418539>.
- [9] V. Shivam, J. Basu, R. Manna, N.K. Mukhopadhyay, Local Composition Migration Induced Microstructural Evolution and Mechanical Properties Medium-Entropy Alloy, *Metall. Mater. Trans. A.* 52 (2021) 1777–1789. <https://doi.org/10.1007/s11661-021-06188-7>.
- [10] G.K. Bansal, V.C. Chandan, Avanish Kumar, Mandal, Gopi Kishor Srivastava, High Entropy Alloys An Overview on Current, in: 2020: pp. 1–68.
- [11] J.M. Torralba, P. Alvarado, A. García-junceda, High-entropy alloys fabricated via powder metallurgy . A critical review, *Powder Metall.* 62 (2019) 1–31. <https://doi.org/10.1080/00325899.2019.1584454>.
- [12] N.J. Peter, M.J. Duarte, C.H. Liebscher, V.C. Srivastava, E.A. Jäggle, G. Dehm, Early stage phase separation of AlCoCr_{0.75}Cu_{0.5}FeNi high-entropy powder at the nanoscale, *J. Alloys Compd.* (2019) 153149. <https://doi.org/10.1016/j.jallcom.2019.153149>.
- [13] C. Suryanarayana, Mechanical Alloying: A Novel Technique to Synthesize Advanced Materials, *Research.* 2019 (2019) 1–17. <https://doi.org/10.34133/2019/4219812>.
- [14] M. Vaidya, G.M. Muralikrishna, B.S. Murty, High-entropy alloys by mechanical alloying : A review, *J. Mater. Res.* 34 (2019) 664–686. <https://doi.org/10.1557/jmr.2019.37>.
- [15] N. Singh, Y. Shadangi, V. Shivam, N.K. Mukhopadhyay, MgAlSiCrFeNi low-density high entropy alloy processed by mechanical alloying and spark plasma sintering: Effect on phase evolution and thermal stability, *J. Alloys Compd.* 875 (2021) 159923. <https://doi.org/10.1016/j.jallcom.2021.159923>.
- [16] V.K. Pandey, Y. Shadangi, V. Shivam, J. Basu, K. Chattopadhyay, B. Majumdar, B.N. Sarma, N.K. Mukhopadhyay, Synthesis, Characterization and Thermal Stability of Nanocrystalline MgAlMnFeCu Low-Density High-Entropy Alloy, *Trans. Indian Inst. Met.* 74 (2021) 33–44. <https://doi.org/10.1007/s12666-020-02114-4>.
- [17] V. Shivam, J. Basu, V.K. Pandey, Y. Shadangi, N.K. Mukhopadhyay, Alloying behaviour, thermal stability and phase evolution in quinary AlCoCrFeNi high entropy alloy, *Adv. Powder Technol.* 29 (2018) 2221–2230. <https://doi.org/10.1016/j.apt.2018.06.006>.
- [18] S. Rohila, R.B. Mane, G. Ummethala, B.B. Panigrahi, Nearly full-density pressureless sintering of AlCoCrFeNi- based high-entropy alloy powders, *J. Mater. Res.* (2019) 1–10. <https://doi.org/10.1557/jmr.2019.9>.
- [19] S. Kumar, D. Kumar, O. Maulik, Synthesis and Air Jet Erosion Study Al₁Fe_{1.5}CrMnNi_{0.5} (x = 0.3, 0.5) High-Entropy Alloys, *Metall. Mater. Trans. A.* 49 (2018) 5607–5618.
- [20] S. Varalakshmi, G. Appa Rao, M. Kamaraj, B.S. Murty, Hot consolidation and mechanical properties of nanocrystalline equiatomic AlFeTiCrZnCu high entropy alloy after mechanical alloying, *J. Mater. Sci.* 45 (2010) 5158–5163. <https://doi.org/10.1007/s10853-010-4246-5>.
- [21] A.R. Miedema, P.F. de Châtel, F.R. de Boer, Cohesion in alloys—fundamentals of a semi-empirical model, *Phys. B.* 100 (1980) 1–28. [https://doi.org/http://dx.doi.org/10.1016/0378-4363\(80\)90054-6](https://doi.org/http://dx.doi.org/10.1016/0378-4363(80)90054-6).
- [22] T.T. Shun, Y.C. Du, Microstructure and tensile behaviors of FCC Al_{10.3}CoCrFeNi high entropy alloy, *J. Alloys Compd.* 479 (2009) 157–160. <https://doi.org/10.1016/j.jallcom.2008.12.088>.
- [23] L. Jiang, Y. Lu, Y. Dong, T. Wang, Z. Cao, T. Li, Annealing effects on the microstructure and properties of bulk high-entropy CoCrFeNiTi_{0.5} alloy casting ingot, *Intermetallics.* 44 (2014) 37–43. <https://doi.org/10.1016/j.intermet.2013.08.016>.
- [24] X. Yang, Y. Zhang, Prediction of high-entropy stabilized solid-solution in multi-component alloys, *Mater. Chem. Phys.* 132 (2012) 233–238. <https://doi.org/10.1016/j.matchemphys.2011.11.021>.

SYNTHESIS OF NANOSTRUCTURED EQUIATOMIC TiCrFeCoNi HIGH-ENTROPY ALLOY BY MECHANICAL ALLOYING AND CONVENTIONAL SINTERING

- [25] S. Guo, Q. Hu, C. Ng, C.T.Liu, More than enthalpy in high entropy alloys: Forming solid solution or amorphous phase, *Intermetallics*. 41 (2013) 96-103.
- [26] S. Guo, C. Ng, J. Lu, C.T. Liu, Effect of valence electron concentration on stability of fcc or bcc phase in high entropy alloys, *J. Appl. Phys.* 109 (2011). <https://doi.org/10.1063/1.3587228>.
- [27] S. Guo, C.T. Liu, Phase stability in high entropy alloys: Formation of solid-solution phase or amorphous phase, *Prog. Nat. Sci. Mater. Int.* 21 (2011) 433-446.

OPTIMIZING METAL POWDERS FOR COLD ISOSTATIC PRESSING

^{a*}Anand Tadas, ^bNicholas Norberg, ^cJohn Duffy

^aMalvern Panalytical, Bangalore, Karnataka, India.

^bMalvern Panalytical B.V, Almelo7602 EA, Netherlands

^cMalvern Panalytical Ltd, Malvern WR14 1XZ, United Kingdom

*anand.tadas@malvernpanalytical.com

Abstract: *Isostatic pressing has several benefits over the commonly used press and sinter method, including equal compaction in all directions and a more uniform final component density. Nevertheless, as with other powder metallurgy processes, manufacturers must carefully characterize the metal powder's properties for the process to be successful. Commonly characterized physical properties include powder flow, density, hardness, particle size, and particle shape of the respective powders.*

Other key characteristics include chemistry and microstructure. Chemistry is paramount as the powder needs to comply with the alloy composition of the material specified, while phase composition and grain size can affect powder hardness and melt behaviour which can affect the forming and sintering process.

In this study we are focusing on the complementary use of X-ray powder diffraction (XRPD), X-ray fluorescence (XRF), and Automated Imaging to evaluate the performance of various iron-based alloys for use in a Cold Isostatic Pressing (CIP) manufacturing process.

Keywords: *Isostatic Pressing, X-ray Diffraction, Particle Size, Particle Shape, Hardness*

1. Introduction

Isostatic pressing is a component-forming process where pressure is applied uniformly (using gas or liquid) to a hermetically sealed container filled with compacted metal powder. Isostatic pressing can be performed at elevated temperatures, known as hot isostatic pressing (HIP), or at ambient temperatures, known as cold isostatic pressing (CIP) [1].

Isostatic pressing has several benefits over the commonly used press and sinter method, including equal compaction in all directions and a more uniform final component density. Nevertheless, as with other powder metallurgy processes, manufacturers must carefully characterize the metal powder's properties for the process to be successful. Commonly characterized physical properties include

powder flow, density, hardness, particle size and particle shape of the respective powders [2].

Other key characteristics include chemistry and microstructure. Chemistry is paramount as the powder needs to comply with the alloy composition of the material specified, while phase composition and grain size can affect powder hardness and melt behaviour which can affect the forming and sintering process [2,3].

In this study we are focusing on the complementary use of X-ray powder diffraction (XRPD), X-ray fluorescence (XRF) and Automated Imaging to evaluate the performance of various iron-based alloys for a use in a CIP manufacturing process.

2. Materials and Methods

Metal powders were produced from three iron-

OPTIMIZING METAL POWDERS FOR COLD ISOSTATIC PRESSING

based alloys: A, B and C. Some of these powders were formed using gas atomization (AGN) – as indicated by ‘G’, whilst others were formed using water atomization processes (AWN, AWY, BWN and CWN) – as indicated by ‘W’. The Y and N coding in the sample ID indicates if the powder was ‘CIPable’ in its as received form, or if annealing was required to facilitate compaction e.g., BWN-Anneal, CWN Anneal.

Particle size and shape analysis were performed on a Morphologi 4 Automated Imaging system (Malvern Panalytical). X-ray diffraction

measurements were performed on an Empyrean Multicore with the PIXcel3D detector and a Co source (Malvern Panalytical). X-ray fluorescence measurements were performed on an Epsilon 3 Spectrometer (Malvern Panalytical).

3. Results and Discussion

Table 1 shows the elemental composition of the various powders as measured with XRF. The Chemistry within the different sample series is consistent, but they also show significant differences in chemical composition between the various types of alloys

Table 1. Elemental composition for the different alloy samples measured using XRF

Sample ID	Fe [Wt %]	Cr [Wt %]	Ni [Wt %]	Mnb [Wt %]	Mo [Wt %]	Si [Wt %]
AGN	73.6	13.3	9.5	0.2	2.5	0.4
AWY	73.5	13.2	9.4	0.2	2.5	0.4
BWN	93.5	1.3	4.3	0.2	0.3	0.3
BWN-Anneal	93.1	1.4	4.5	0.3	0.3	0.4
CWN	97.8	1.1	0.2	0.6	0.0	0.2
CWN-Anneal	97.7	1.1	0.1	0.6	0.0	0.2

Table 2 summarises the XRD results along with particle size, particle shape and hardness for each alloy including whether that powder formed a CIP part successfully. Alloy A formed a successful part when it was water-atomized

but not when it was gas-atomized. For these two materials the phase composition and crystallite size are similar, and they also exhibit similar hardness values, with the gas atomized material being a little softer than water atomized.

Table 2. Summary of XRD results along with morphology and hardness for each alloy including whether that powder formed a successful CIP part

Material	CE Diameter / μm	Circularity D50	% Vol ferrite (bcc)	% Vol austenite (fcc)	% Vol total carbides	Ferrite crystallite size / nm	Hardness	CIPable
AGN	21.8	0.985	94.8	5.2	-	62	356	no
AWY	17.50	0.815	94.7	5.3	-	49	377	yes
BWN	23.46	0.984	97	3.0	-	96	470	no
BWN Anneal	15.67	0.959	99	-	0.8	214	261	yes
CWN	14.00	0.928	99.8	-	-	159	370	no
CWN Anneal	14.90	0.921	99.0	-	0.7	265	209	yes

OPTIMIZING METAL POWDERS FOR COLD ISOSTATIC PRESSING

The particle size of the two materials is also similar but the particle morphology is found to be very different, as Figure 1 illustrates, with the water atomized material having a much lower circularity than the gas atomized one. Spherical powders such as those produced by gas atomisation give higher packing density than irregular particles as particles can rearrange more easily due to lower interparticle friction [4].

But this reduced friction also makes it difficult for particle interlocking to occur during the CIP process, resulting in an unstable green body with low strength. For more irregular particles with higher surface area (such as those produced by water atomization), interparticle friction is higher, and interlocking during compaction is more likely to form a stable green body with higher strength[1,2].



Fig.1. Schematic of a Cold Isostatic Pressing (CIP) process

For samples B and C which were both water atomised, the as-atomised powder did not form stable green parts although the annealed powders did. As particle shape size and shape were similar between annealed and as atomized powders it could not be attributed to morphology but can instead be attributed to significant reduction in hardness on annealing.

The effect of annealing on the microstructures of alloy A and alloy B are shown by the respective XRD patterns in Figure 2. For alloy A there is little change in the phase composition and crystallite size on annealing, corresponding to similar Hardness. For alloy B, annealing results in some minor changes in phase composition, which may be expected to increase hardness, but the major change is in the broadening of the Ferrite peak.

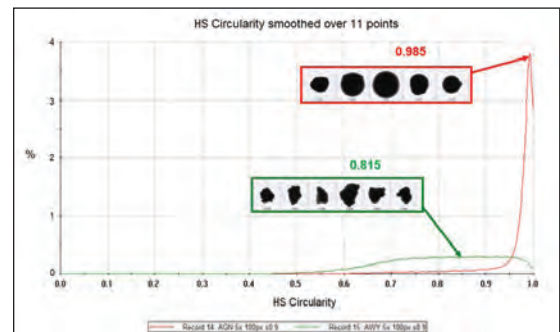


Fig. 2. Comparing High Sensitivity (HS) circularity for the water and gas-atomized Alloy A. Inset: representative particle images, from the mean circularity, for the two samples

This broadening corresponds to an increase in crystallite size and is likely the main reason for the decrease in Hardness [5]. Increasing Hardness with decreasing crystallite (or grain) size is

well known and can be described by the Hall-Petch relation[6]. It is attributed to an increased number of grain boundaries which impedes the relative movement of adjacent grains by two main mechanisms; change in direction of motion due to differing grain orientation, and discontinuity of slip planes between grains [7].

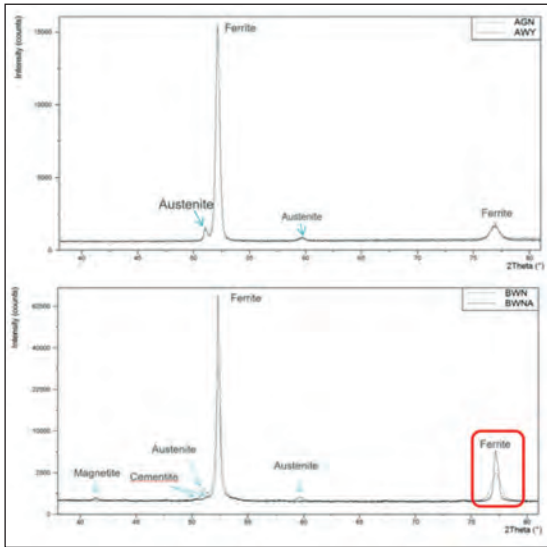


Fig. 3. X-ray diffraction patterns for alloys AGN and AGY (top) and alloy BWN and BWNA (bottom): Alloy B shows broadening of Ferrite peak at 2Theta ~ 77° corresponding to an increase in grain size.

4. Conclusions

In order to ensure good quality consistent manufacture of metal parts during Cold Isostatic Pressing (CIP) a thorough understanding of raw the metal powders is required including particle size distribution, particle shape, elemental composition and microstructure of the material. A tool kit of analytical techniques including Image Analysis, X-ray diffraction and X-ray fluorescence enables such parameters to be assessed and correlated with final product performance.

Acknowledgements

The authors acknowledge the Manufacturing Technology Center (Coventry, United Kingdom)

who provided the samples used in this study including Hardness data and cold isostatic pressing performance.

References

- [1] Attia, U.M., 2021. Cold-isostatic pressing of metal powders: a review of the technology and recent developments. *Critical Reviews in Solid State and Materials Sciences*, 46(6), pp.587-610.
- [2] James, P.J., 1977. Particle deformation during cold isostatic pressing of metal powders. *Powder Metallurgy*, 20(4), pp.199-204.
- [3] Livne, Z., Munitz, A., Rawers, J.C. and Fields, R.J., 1998. Consolidation of nanoscale iron powders. *Nanostructured materials*, 10(4), pp.503-522.
- [4] Heaney. DF, *Handbook of metal injection molding*, Woodhead Publishing, 2012
- [5] Speakman, S.A., 2014. Estimating crystallite size using XRD. *MIT Center for Materials Science and Engineering*, pp.03-08.
- [6] Weertman, J.R., 1993. Hall-Petch strengthening in nanocrystalline metals. *Materials Science and Engineering: A*, 166(1-2), pp.161-167.
- [7] HANDBOOK, D.F., 1993. *MECHANICAL SCIENCE* (Vol. 1, p. 2). DOE-HDBK-1018/1-93.

USE OF METAL INJECTION MOULDING (MIM)- OFF HIGHWAY INDUSTRY PERSPECTIVE

Manish Gokhale

Senior Materials Engineer, Enterprise Technology & Engineering Center
John Deere India Pvt Limited, Pune, India
gokhalemanish@johndeere.com

Abstract: The off-highway industry comprises the machineries and equipment used for agricultural, construction and forestry applications. Tractors, combine harvesters, backhoe loader etc. are the few examples which falls under off-highway industry. Conventionally, the components made for off-highway industry are manufactured using forging, casting, machined from bar stock and sheet metal fabrication.

This paper will showcase the potential applications, challenges, and consideration of MIM in view of off-highway industries with some examples. The constraints and challenges came across the way and few potential design considerations has been discussed in detail. As compared to automotive applications the off-highway vehicles are dealing with uncertain loading, higher torques & loading condition which make it more difficult for design optimization. The MIM limitations in terms of annual volume, size and mass must be reviewed. Another aspect on less adoption of this technology is that the lack of awareness of this manufacturing technology in the design community not leveraging it to its full potential. Apart from this, there are several other challenges in exploring MIM like the raw material cost (impacting final product), higher tooling cost makes it more challenging for higher penetration of MIM in case of off-road vehicles.

Keywords: MIM, off-highway industry

1. Introduction

The powder injection moulding (PIM) which is commonly known as metal injection molding since predominant use of metal powders has been in the production since 1970 [1]. The Metal Injection Molding (MIM) can be considered as a combination of powder metallurgy and plastic injection molding in layman language. The molded part is oversized and has shrinkage allowance which is sintered at high temperature like conventional sintering process where final shape & size is achieved to produce near net shaped component. The main advantage of MIM over typical PM part is higher precision and accuracy along with capability of producing to full density of material (almost 99.5%).

According to latest market research [2], the metal injection molding industry has a global turnover of around \$ 2.4 billion in 2016 and projected to grow up to \$ 3.8 billion by 2022. The MIM process has multiple benefits on small

and precision components used in the medical, electronics, watch industries along with handful of uses in automobile and other industries for complex and small parts.

1.1. MIM Process Flow:

The MIM process consist of mainly four components in the overall manufacturing which is illustrated in the Fig.1.

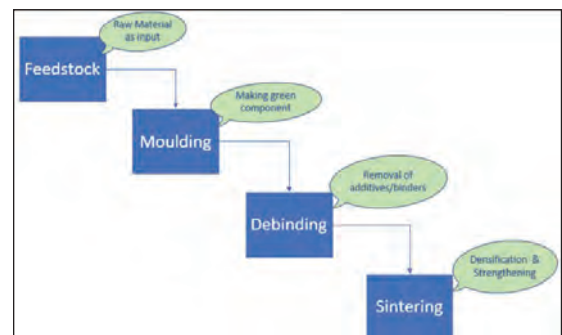


Fig.1. Schematic of typical MIM process

USE OF METAL INJECTION MOULDING (MIM)- OFF HIGHWAY INDUSTRY PERSPECTIVE

The feedstock is basically consisting of the metallic alloy made as a feedstock by mixing various metal powders bonded together with resins and additives. The typically granular feedstock is the raw material for the process which is further heated and inserted into the molding machine where it takes the shape of the final components. Once the molding is completed the green components are further processed in de-binding operation to remove the additives and binders. The components are further put in the sintering furnaces like powder metal processing to form metallic bond and achieve final density. The as molded is near to net shape and typically no further processing is required except deburring or removing some flashes.

1.2. MIM Advantages:

MIM Advantages are listed as below:

- Ability to manufacture complex geometries with high precision and accuracy
- Near net shape manufacturing with no or very less finishing required by machining
- Near full density with higher mechanical properties
- Wide ranges of alloys and materials available
- High volume parts with good repeatability
- Highest material utilization (less energy and scrap generation)

1.3. Off-Highway Industry and its challenges

The off-highway industry comprises the machineries and equipment used for agricultural, construction and forestry applications. Tractors, combine harvesters, backhoe loader etc. are the few examples which falls under off-highway industry. Fig. 2a, 2b and 2c represents the magnitude & large scale of off-highway equipment. The fig. 2c shows the scale of the machines where the tire height is more than height of a person. Conventionally, the

components made for off-highway industry are manufactured using forging, casting, machined from bar stock and sheet metal fabrication.



Fig.2. a. Tracked wheeled tractor



Fig.2. b. Cotton Harvester



Fig.2. c. Agriculture Tractor rvester

USE OF METAL INJECTION MOULDING (MIM)- OFF HIGHWAY INDUSTRY PERSPECTIVE

Another factor is the variety of components used in an off-highway vehicle. A typical combine harvester would be having more than 10000 of parts in a machine and selection of right manufacturing process for a part could be a challenge. It was also difficult to cover different sub-systems within a product family.

We hereby studied the potential applications, challenges, and consideration of MIM in view of off-highway industries with some examples. The constraints and challenges came across the way and few potential design considerations has been discussed in detail.

2. Approach

In this study, we have developed a structured approach to identify the right candidate for MIM process. The decision matrix comprising of various parameter as given in Fig.3 which has helped to select the correct components. Each parameter has been given specific weight and all the components are ranked accordingly. The ranking is given from a scale of 1 to 5 where 1 being low scored and 5 as highest. After the assessment of various components, the final selection is made for the parts which has highest score.

Parameters	Weightage	Part A	Part B	Part C	Part D	Part E
Cost	5	4	3	4	5	2
Complexity	3	3	1	3	5	4
Weight	4	4	3	3	1	4
Annual usage	3	3	1	4	2	2
Material	1	2	3	4	3	4
Total Score		56	36	40	58	50

Fig.3 Decision Matrix for MIM

In the Fig.3, using the decision matrix, out of 5 different parts, the top 3 parts (A, D &E) were selected for MIM conversion and further shared to manufacturer for technical feasibility and quoting purpose.

Using this, below are some of examples of the components which were identified for potential

MIM parts are shown in the figure 4. The parts showcased here includes small actuators, relief valves etc. having significant machining & complex manufacturing process.

Based on the discussions with MIM supplier and quotations received, final decision to go head for MIM was taken.



Fig.4. Identified parts for MIM conversion

3. Discussions and Results

As compared to automotive or other industries like electronics or consumer appliances, the off-highway vehicles are dealing with uncertain loading, higher torques & loading condition which make it more difficult for design optimization. The MIM limitations in terms size and part weight must be reviewed.

Another aspect on less adoption of this technology is that the lack of awareness of this manufacturing technology in the design community not leveraging it to its full potential. The small components which can be designed with complex and 3D features should be considered to get full benefits of MIM.

Some of the critical learning or takeaways from this study is detailed out as below:

- Raw Material cost and availability: Though there are multiple materials and alloys available for MIM, the manufactures may not use all the available options. This could limit in selecting the optimum material for a given

USE OF METAL INJECTION MOULDING (MIM)- OFF HIGHWAY INDUSTRY PERSPECTIVE

application. Often the annual usage of the parts does not justify or influence adopting. MIM manufacturers may be depending on imported feedstock which increases the material cost.

- Economies of scale: Unless there is sufficient annual usage, it may not become viable to use MIM process
- Initial investment: The tooling cost involved are too high as compared to conventional processes. Getting experimental parts could be a challenge.
- Weight constraint: Typically, MIM process is suitable and economical for parts weights ranging for 5 - 50 gm though parts up to 200 gm can produced (at higher cost)
- Complexity of parts: Parts with less complex features can be made in MIM but may not come with optimum cost as full benefits of MIM are not explored. Adding multiple features in single component would help to reduce overall cost of the sub-system.

4. Conclusion

MIM can be fully leveraged if we critically select right components & integrate MIM at early phase of design concepting. Applying this to off-highway industry could be a challenge considering higher loads, dynamic conditions, and bigger geometries. The benefit of this technology to get better quality products at optimum price and at less power consumption is still under utilized in the off-highway industry. The material availability at right cost could be a challenge in case MIM.

Acknowledgements

As an author, I would like to thank PMAI for giving this opportunity to present my work in this forum.

References

- [1] R. M. German Metal Powder Injection Molding (MIM) key trends and markets Metal powder

injection molding (MIM): key trends and markets - ScienceDirect

- [2] Marketsandmarkets - Metal injection molding market (Metal Injection Molding Market Size & Share | Analysis Report 2022 | MarketsandMarkets)

FROM RESEARCH TO INDUSTRY - APPLICATIONS AND LATEST DEVELOPMENTS IN THE FIELD OF FAST/SPS SINTERING

Jens Huber

Dr. Fritsch SondermaFellbach, 10Baden-W11uerttemberg, Germany, 70736.
arthur.becker@dr-fritsch.de

I. Introduction

The FAST/SPS sintering process is experiencing strong growth rates and is increasingly replacing conventional hot pressing, especially in new applications. To date, Dr. Fritsch alone has installed well over 1,000 FAST/SPS sintering presses worldwide - about 98% of them at production companies.

It is estimated that there are currently about 2,000 operational sintering presses worldwide that work according to the FAST/SPS principle. The majority of these are used in the industry for development and production, and only a relatively small number in university related research.

Originating in the diamond tool industry, FAST/SPS has spread to many other industrial sectors. Probably even the company founder and engineer Dr. Fritsch, the developer of the first industrially usable FAST/SPS system, could not have imagined the diverse applications of this sintering technology in 1953. Today, this technology is used in fields as diverse as the diamond tool and friction lining industries, in the manufacture of sputter targets, in the production of heat sinks, in the carbide and ceramics industries, in the production of solid-state batteries and fuel cells, as well as in development departments, universities and R&D institutes. The list of new applications is getting longer every year.

Most users are already familiar with traditional hot pressing methods before they get into contact with FAST/SPS sintering. Traditional hot pressing is one of the most widely used methods for consolidating cold-pressed or loose powders.

However, hot pressing is often associated with long sintering cycles and low flexibility.

FAST/SPS sintering follows a different approach. FAST stands for "Field Assisted Sintering Technique", SPS for "Spark Plasma Sintering". The terms are used synonymously and refer to sintering by means of joule heating. Current is passed directly through the mold. The resistance of the mold material and the powder part or green compact generate the heat directly in the powder or mold. Unlike the conventional furnace, neither the sintering chamber nor the atmosphere inside the chamber is actively heated. The heat is generated directly where it is needed - in the sintered material or in the mold surrounding the sintered material.

This leads to very high heating rates and additionally to a significant increase in the sintering activity of fine metal powder aggregates. Depending on the part size, sintering cycles of only a few minutes can be achieved. Furthermore, this process lowers the sintering temperature and the sintering pressure compared to conventional sintering processes.

The diamond tooling industry was one of the first industrial adopters of the FAST/SPS process because it solved a problem the industry was struggling with. When diamonds embedded in a metal matrix are sintered for too long, they carbonize. As a result, the diamond tool can no longer cut into hard materials. The idea was therefore to develop a sintering process that is so fast ("FAST") that the diamonds do not carbonize. In addition, the new sintering process allowed the sintering temperatures to be lowered, which further reduced the risk

of carbonization and shortened the sintering cycle time compared to conventional sintering techniques.



Figure 1: Typical diamond tool segment consisting of a metal matrix in which diamonds are embedded in defined positions and several layers by means of a technique developed by Dr. Fritsch ("DiaSet"). These segments are, for example welded onto cut-off wheels or drill bits, used for cutting asphalt, granite, marble or concrete.

II. Field Assisted Sintering

The basic idea of sintering with electric current is relatively old. The resistance heating of hard metal powders was patented as early as 1933 by the American inventor George F. Taylor []. Since then, the technique has evolved and is known by many different names. SPS, Spark Plasma Sintering, is the most commonly used name, but from a technical point of view it is not correct. There is no proof of the existence of a spark or a plasma. Therefore, for some years now, the term FAST has often been prefixed, which is technically a more appropriate description of how it works. Other terms found in the literature are "Rapid Hot-Pressing", "Direct Current Sintering" and many others. Due to the high cost associated with generating a pulsed current and its unproven effectiveness, optional pulsing is much less common in industrial applications.

Scientific studies show that there is no discernible difference between sintering with pulsed and unpulsed current. The same improved sintering results (compared to conventional sintering) can be achieved with all FAST/SPS sintering techniques [].

III. Existing industrial applications

Typical materials and applications of FAST/SPS are:

- Metals and hard metals
- Technical ceramics
- Multilayer composites
- Functionally graded materials (FGMs)

For industrial series production of e.g.:

- Sputtering targets for surface coatings
- Abrasion resistant parts for agricultural machinery
- Friction materials for brakes and clutches
- Diamond tools (metal-diamond alloys)
- Thermoelectric materials for the use of waste heat
- Ballistic protection plates
- Hydraulic cylinders e.g. for industrial trucks
- neutron absorber
- Wear-resistant components for agricultural and forestry equipment
- Ceramic components for the semiconductor industry to name just a few of the most common applications.

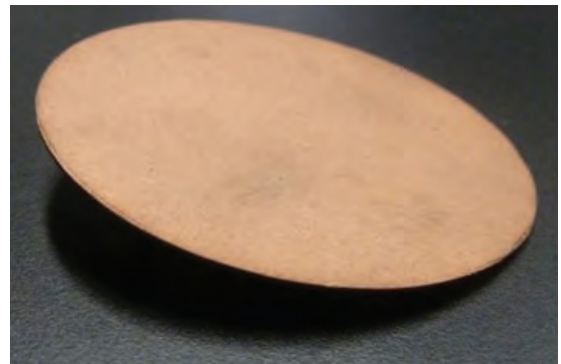


Figure 2: Heat Sink for industrial lasers. A thin Cu-based metal matrix with embedded homogeneously distributed diamonds.

All types of materials can be sintered, whether they are conductive, non-conductive or semi-

conductive, or whether they change their conductivity during heat treatment. In all these cases, the advantages of a FAST/SPS process come into play, especially:

- Reduction of grain growth thanks to high heating rates
- Effective use of energy, as heat is generated where it is needed.

In some industries, a good result is defined as the full densification of the material, often in the sputter target industry, for example. In other applications, the material must have a well-defined porosity, for example in stainless steel filters. Precise control of all process parameters is an important reason why both researchers and manufacturers are switching from rather imprecisely controllable traditional furnaces to modern FAST/SPS sintering presses.

Typical applications are, besides (hard) metals and steel, the sintering of technical ceramics such as B_4C , AlN , TiB_2 , Al_2O_3 and others. For sputter target applications, dense ceramics with a diameter of 400mm have already been sintered with Dr. Fritsch FAST/SPS sintering presses, which proves that the technology is not only suitable for sintering large dimensions of metals, but also of ceramic materials.



Figure 3: A FAST/SPS-sintered sputter target made of a technical ceramic with a 2-Euro coin lying on it for size comparison.

Functionally graded materials (FGMs)

Especially in wear-relevant applications, industry demands materials that increase the performance and service life of a product. The combination of seemingly contradictory properties cannot be achieved by one material alone. Innovative applications are therefore increasingly based on combinations of materials, so-called functionally graded materials (FGM). A product can have the properties and advantages of material A on the one hand and those of material B on the other. There is a material gradient between these two sides.

To make this gradient homogeneous, a sintering technique is required that allows precise control of all sintering parameters and is fast enough to avoid unwanted grain growth. FAST/SPS sintering creates a controlled soft phase between the different materials so that they can bond together. In addition, the layers of solidified loose powder can be sintered onto a support. All this can be done in a single sintering cycle, eliminating the cost of additional production steps.

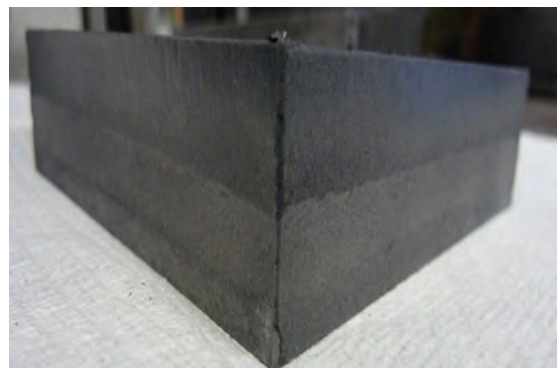


Figure 4: Functionally graded material (so-called FGM). Multilayer material structure for industrial series production of weldable tungsten carbide components.

IV. Development of a new industrial application using the example of graded ceramic solid-state electrolytes

Dr. Fritsch and the Fraunhofer Institute IPA in Stuttgart are partners in a research project to develop new mixing and sintering techniques for research into graded ceramic solid-state electrolytes. The program is funded by the German state of Baden-Wuerttemberg ("InvestBW").

This development project is not only a good example of successful cooperation between research institutes and industry, but also sheds light on the need to adapt machine concepts to different applications.

While established industries need to adapt or expand from time to time, it is rare that a "breakthrough technology" emerges that greatly changes the entire industry. However, it does happen from time to time, and this presents both risks and opportunities.

At the moment, the automotive industry is experiencing what it means when a disruptive technology changes the market. The switch from combustion engines to battery-powered vehicles is a major challenge for almost all players in this market. For many companies in this industry, it is a matter of survival to adopt the new technologies and drastically increase their R&D activities.

Today's lithium-ion cells, although widely used, have significant drawbacks that are not accepted by most consumers. For example, the limited storage capacity, which leads to a low range of the vehicle, the risk of explosion and the continuous decrease of the charging capacity of the battery, which further reduces the range and also the value of the vehicle after a few years [iii].

However, a technology that is not accepted by consumers cannot prevail in the long run.

The breakthrough could succeed if so-called "all solid state lithium-ion batteries" deliver what they promise. Like any battery, they consist of an anode, a cathode and the electrolyte [iv]. However, the electrolyte is not in a liquid state, which allows the use of lithium metal as the anode material. Lithium metal has a much higher energy density than the graphite or graphite-silicon composite anodes used today [v].

There are mainly three types of solid electrolytes: polymer-based, sulfur-based and oxide-based (oxide and phosphate ceramics). They are characterized by good conductivity (up to 1 mS/cm) and high electrochemical stability when in contact with the cathode material [vi]. Compared to lithium, these ceramic materials have a potential of more than 5 V. Thus, both high voltage cathodes and lithium metal anodes can be used, which significantly increases the energy density. Another advantage is that the materials are not very temperature sensitive, i.e. they do not need to be heated (like polymer electrolytes) or cooled when exposed to high temperatures [vii].

Ceramic powders are usually hot pressed. The disadvantages of conventional hot pressing are the long sintering cycle times of several hours, the energy-intensive operation of the hot presses [viii] and the negative effects of the long heat exposure on the material properties such as grain growth, which reduces homogeneity and density. FAST/SPS reduces grain growth to a minimum by shortening the sintering cycle time thanks to high heating rates and comparatively short heat exposure. Another advantage of developing battery cells with FAST/SPS is that it is less likely that lithium will evaporate, creating unwanted by-products. At the same time, the higher densities achieved by the FAST/SPS process improve the conductivity of the ions [ix] [x].

FROM RESEARCH TO INDUSTRY - APPLICATIONS AND LATEST DEVELOPMENTS IN THE FIELD OF FAST/SPS SINTERING

Another challenge is the development of a thermomechanically stable and safe connection of solid-state electrolyte and electrochemically active material. This is necessary because current solid-state electrodes cannot withstand the thermomechanical stresses caused by the constant volume changes during charge and discharge cycles^[ix] [x]. The gradation should be achieved by interconnecting electrolyte layers with different proportions of solid electrolyte and active material. The need to join graded layers is another reason for preferring FAST/SPS over other sintering techniques. FAST/SPS allows precise control and almost instantaneous adjustment of sintering parameters, unlike a conventional hot press, which is comparatively sluggish and slow.

Scaling

The solid-state battery market is expected to grow at an average annual CAGR of 8.53%, according to a market study by Canadian/Indian market analysis firm Precedence Research (dated February 1, 2021) [xi].

This growth rate shows that any process used in research must be suitable for mass production. While a large number of FAST/SPS machines are available for basic research with small geometries, there are not many manufacturers of large production machines.

In order to bring an economically successful product to market, the FAST/SPS machines used for production must be able to achieve sufficient production output (economy of scale), reproducibility, reduction of manpower requirements through a high degree of automation and high energy efficiency. In addition, the machines must be compact, easy to transport and install, and easy to operate. All these aspects must be taken into account when developing a FAST/SPS production machine for industrial mass production.

Furthermore, the production of graded solid state electrodes includes not only FAST/SPS sintering, but also the development of mixing techniques, powder handling solutions and automation. Dr. Fritsch combines all necessary disciplines and has been developing FAST/SPS sintering presses, mixers, automation systems and powders for industrial applications since 1953.



Figure 5: FAST/SPS sintering press with integrated cooling chamber (right) for cycle time optimized (mass) production (Dr. Fritsch MSP-5 with MSC-5)

Future production machines for all solid-state battery materials will be based on concepts similar to industrial production machines such as the MSP-5 and the connectable MSC-5 cooling station. This FAST/SPS sintering press, which already exists and is successfully used in production today, enables automated and continuous FAST/SPS sintering with high output rates. The machine concept includes the transfer of the mold or stack from the sintering chamber to the cooling chamber in the hot state under vacuum and inert gas. This separates the cooling cycle from the sintering process so that the sintering chamber is available again for the next sintering cycle. Future machine concepts may include preheating, automation solutions and post-cooling processes in modular combinations.

An important and often underestimated aspect of scaling FAST/SPS sintering is that the mold design and sintering parameters can change significantly when the output quantity changes so that the sintering process must be adjusted to a great extent. It is true that there are also differences in all other heat treatment techniques, whether single pieces or large molds with several cavities and/or layers are sintered. However, in a conventional hot press, mainly the already long sintering process becomes even longer, simply because the sintering press is larger and it takes even longer for the heat to penetrate a large mold from the outside to the inside. Consequently, users of traditional hot presses often have to deal with cycle times of 24 hours or more.

However, the main purpose of the FAST/SPS process is to achieve short sintering cycles with all the advantages in terms of material properties, energy savings and productivity. Therefore, when scaling up production quantities in FAST/SPS sintering, the aim is to keep the sintering cycle as short as possible. This requires special attention in terms of mold layout and the design of the sintering cycle.

Until now, this process of cycle and mold optimization has been based mainly on user experience. Through trial and error, best practice, etc., procedures have developed which should enable the achievement of a satisfactory result. One such result could be, for example, the achievement of certain desired material properties or unit costs. As soon as this goal is reached, the optimization process is often terminated in industrial practice - even though better results could possibly be achieved with other approaches.

These optimization reserves are usually not found without corresponding pressure, for example due to the need to reduce unit costs.

In the meantime, however, so much data is available on FAST/SPS sintering that these

processes can be modeled quite well. With the help of this data, a fairly good prediction of the sintering result can already be made today for many applications using appropriate simulation software. In this way, molds can be designed, optimized and sintering cycles adapted in order to save development time and to be able to exploit the full optimization potential. Such software is, for example, "Engemini" from the French company Norimat.

V. Specific advantages of the FAST/PLC process in industrial applications

In industrial applications, guided by economic principles, the relatively short cycle time compared to conventional hot pressing is in the foreground when using the FAST/SPS process. This results in the frequently and extensively investigated advantages in terms of material properties. Ideally, these advantages should ultimately lead to a better performing product compared to the competition.

Another obvious aspect is that a significantly shorter sintering cycle can lead to higher productivity compared to conventional hot pressing. This in turn usually helps to reduce the sintering cost per piece.

From the point of view of many industrial users, this combination alone, better product performance with often lower unit costs, is an enticing prospect and reason enough to take a closer look at FAST/SPS.

Other important factors for industrial users of FAST/SPS systems are:

1. Energy saving

Conventional hot pressing, just like conventional ovens, has the serious disadvantage of indirect heating. In addition to the well-known effects on cycle time, productivity and material properties, a cost and resource problem also arises due to the high energy consumption. Unlike FAST/SPS, hot pressing uses much of the introduced energy

FROM RESEARCH TO INDUSTRY - APPLICATIONS AND LATEST DEVELOPMENTS IN THE FIELD OF FAST/SPS SINTERING

to heat the oven chamber, the atmosphere in the chamber, and the mold. The heat generated in this way does not contribute anything effectively to sintering, but only creates the prerequisite for the material to be sintered in the mold in the first place. However, since this considerable amount of energy is not used for sintering in the actual sense, it represents a loss.

Worse still, much of the energy introduced into the system must also be removed from the system during and at the end of the sintering cycle. This is usually done with the help of cooling water, which is passed through the heated components of the hot press. Since the entire chamber is heated, there is a significantly higher cooling water requirement compared to FAST/SPS sintering presses and, as a result, the energy input for cooling is also usually much higher. Although the size and thus the power consumption of the cooling unit can be reduced somewhat by using a larger cooling water tank, this option quickly reaches its limits if production is carried out in shifts without interruptions and several hot presses are operated simultaneously.

Case Study:

A sputter target manufacturer compares the pure energy input of a conventional hot press with the Dr. Fritsch DSP-535 FAST/SPS sintering press. He comes to the following result for the production of an identical sputter target:

Table 1: Comparison of consumption. Source: KfW funding application from a customer of FAST/SPS manufacturer Dr. Fritsch.

Designation	Hot press (medium frequency induction plant)	Dr. Fritsch DSP- 535 FAST/SPS system
Connected load (kVA)	480	420
Required power (kVA)	390	280
Process time in hours	12,5	4,5

The example shows the comparison with an induction-heated hot press. In the field of conventional hot presses, this is even a relatively energy-saving process, since the heat is generated close to the mold. The comparison would have been even more in favor of FAST/SPS if a hot press heated by heating elements had been used. The energy saving in this case can be up to 40%. Other influencing factors, for example the energy required to reduce the cooling water temperature, are not taken into account in this representation.

The above calculation resulted in a subsidy application and in the specific case the investment in a Dr. Fritsch DSP-535 was subsidized by the KfW (Kreditanstalt für Wiederaufbau in Germany) as a green technology with a non-repayable amount of 26% of the acquisition costs. This also includes, in part, a subsidy which is granted when the heated cooling water is used to heat the company building [].

Compared to heat treatment methods which apply temperature and pressure separately (e.g. furnace with downstream calibration process), sintering by means of FAST/SPS can be carried out at reduced temperatures and pressures. Above all, the lower sintering temperature also contributes to the fact that the total energy consumption for FAST/SPS sintering is significantly lower compared to hot pressing.

The energy savings outlined above are given a much higher priority, not least because of the unresolved issues of availability, security and costs of energy supply with gas and oil. It can be assumed that political steering and also steering by the market will in future be more restrictive in handling, limiting, sanctioning or possibly even prohibiting the use of energy-inefficient production technologies, provided that more energy-efficient alternatives such as FAST/SPS are available. Even if there is no political control,

the market will prefer products with lower unit costs and thus lower selling prices, which will lead to an indirect steering towards energy-saving production technologies such as FAST/SPS.

2. Safety

Compared to conventional hot presses, FAST/SPS systems are able to heat materials so precisely that dangerous vapor phases can be greatly reduced or avoided. By design, conventional hot presses have exposed cooling plates to protect the furnace chamber structure from the very high internal temperature. Some commonly used materials, such as copper or silver, have high vapor pressures. If the sintered material evaporates onto these hot cooling plates, very serious damage to the hot presses can sometimes occur. This not only costs money directly, but also indirectly. Directly, because the repair is extremely expensive - on average about EUR 100,000 for a production plant. And indirectly, because the production machine may not be available for production for several weeks after such an incident. The indirect damages can be significantly higher than the directly caused costs. The financial damage caused by conventional hot pressing can exceed the purchase price of a FAST/SPS system many times over.

3. Flexibility

Both in research and in industrial production, the most flexible machine utilization possible is an essential argument for the use of FAST/SPS sintering systems.

The relatively short sintering cycles compared to conventional hot presses make it obvious to use FAST/SPS sintering presses for the manufacture of products that are in demand at short notice and must be available quickly. This is the case, for example, in the area of customized products,

such as sputter targets for surface coating. In industry, there is therefore often a division between production that can be planned in the long term, which is controlled by call-off plans, and short-term production, which is to be carried out as soon as possible after receipt of the order. There can be several reasons why a company requires quick deliveries. Besides unexpected incoming orders, a common (and all too human) reason is that the required products were simply forgotten to be ordered.

Since long-term demand is easy to plan, production can be carried out using slow production methods at low-cost locations. By their nature, these often standardized products have a relatively low profit margin.

Manufacturers in rather high-priced locations have therefore often specialized in supplying customer- and application-specific products with short delivery times. Since these manufacturers often meet an acute need of their customers, they can work with much higher margins. These very attractive market niches would be impossible to develop with conventional sintering methods.

Case Study:

A major European manufacturer of sintered motorcycle brake pads equips racing teams with pads that are sometimes developed only for individual riders, specific race tracks, weather conditions and, of course, motorcycle types. In the preparation races, different pads are tested on the track. If the race team is not satisfied with any of the prepared pads, or if general conditions suddenly change, the brake pad manufacturer has to adjust the pad compound on demand - sometimes literally overnight - and produce new brake pads. Without FAST/SPS, this would only be possible with considerably more time, since sintering alone would take much longer. The pads are then shipped by express, sometimes the night before the race, to be mounted and driven the next day.

A new motivation for the use of FAST/SPS arose from the worldwide shortage of transport capacities that persists for several years. Due to the hardly predictable delays in the delivery of goods by sea, there was a strong need to locate production closer to the end customer. This was accompanied by the expectation that proximity would significantly reduce the time needed for advance planning and that customer-specific requirements could be met more quickly. FAST/SPS is ideally suited to meet these changing customer requirements.

4. Elimination of upstream or downstream production steps

If two or more materials are to be joined, there are several possibilities. On the one hand mechanical methods, on the other hand materials can be joined using techniques such as soldering or welding. These techniques naturally reach their limits when loose powder layers are to be connected. But even in the case of two solids, soldering or welding always have the disadvantage that they represent a work step that cannot be integrated into the sintering process and must be carried out separately using suitable technical equipment. In addition, soldering only works with the aid of a connection agent, the solder. Solder, however, is expensive. In addition, the soldering process is very slow, even slower than the welding process.

If a sintering technology makes it possible to bond materials firmly at the same time during sintering process itself, this naturally arouses great interest in industry. Because this not only saves additional work steps and the acquisition of expensive equipment, but above all saves time and thus a great deal of money. In contrast to conventional heat treatment methods, FAST/SPS can actually eliminate these additional work steps and integrate them into the sintering process.



Figure 6: Motorcycle brake lining. Copper-plated carrier (bottom) and two sintered friction linings. The two materials are bonded during sintering without the use of auxiliary materials, and the sintering of the friction lining does not require any subsequent calibration.

Case Study:

Brake linings have traditionally been sintered in a pressure less process for decades, for example in belt furnaces or bell furnaces. After sintering, the friction lining was calibrated, i.e. compacted to the required final height with a cold press while still warm. This brake lining was then brazed onto a steel carrier using solder. Since this connection is extremely important for the safety of the vehicle being braked with the lining, dangerous sources of error lay here in the event of an inadequate connection.

The changeover from belt or bell ovens to FAST/SPS now not only brings the advantage of the often considerable gain in productivity (especially in comparison with bell ovens), but also the advantage that the work steps of calibration and soldering, as well as the use of the expensive solder, are no longer necessary. In addition, the connection between the brake pad and the carrier body is significantly improved, which in turn increases product safety.

The advantages of FAST/SPS are so outstanding in the friction lining industry that leading friction lining manufacturers worldwide are switching their production completely to FAST/SPS. This industry has therefore grown to become the

world's largest user of industrial FAST/SPS systems after the diamond tool industry.

Even when joining powder coatings, FAST/SPS generally delivers results that are significantly higher in quality than those achievable in conventional hot presses. The main reason for this is the very precise and reliably reproducible control of the sintering parameters temperature and pressure and the short exposure of the materials to both. As a result, soft phases can be achieved in the area of the powder transitions, which ensure a very strong bond between the materials.

The process steps mentioned so far that can be omitted with FAST/SPS all relate to work downstream of sintering. However, there are also process steps upstream of sintering that can be saved by converting to FAST/SPS.

When using loose powder, cold pressing can be dispensed in many cases. This makes sense especially when large geometries are to be sintered. Since heat is generated and pressure is applied simultaneously in FAST/SPS sintering, the temperatures and pressures required to achieve the target density are significantly lower compared to conventional sintering. Powder becomes sinter-active earlier in FAST/SPS sintering, which leads to energy savings, among other things. Whereas a belt furnace or bell furnace cannot process loose powder and must necessarily rely on cold-pressed green compacts as raw material, the FAST/SPS sintering press can process loose powder without any problems. This means that the entire upstream production step of cold pressing can be saved.

Particularly if the corresponding equipment is not yet available, dispensing with cold pressing saves acquisition costs of many hundreds of thousands or even millions of euros - plus, of course, the entire follow-up costs.

VI. Prospects

In the case of new applications, such as the production of solid-state electrolyte, there are always several competing manufacturing processes being tested at the beginning. Over time, individual ones crystallize as technically mature, reliable, scalable or cost-effective. Ideally, several of these attributes apply. Such a process will then presumably prevail.

In the field of solid-state batteries, it is unlikely that a single manufacturing process will be able to cover all industries and areas of application. It is quite conceivable, for example, that different manufacturing processes will prevail for automotive applications than for so-called "wearables" (e.g. mobile phones, watches, etc.) or power tools.

However, the essential properties of FAST/SPS suggest that several characteristics are certainly fulfilled to make this sintering technology an important or main production process for solid-state batteries. In addition to the particularly advantageous achievable material properties and the proven suitability as a mass production process, it is in particular the significantly reduced energy consumption compared to other sintering technologies that makes the process interesting, as these costs would otherwise flow directly into the price of the end product.

It can therefore be assumed that FAST/SPS will become one of the main manufacturing processes for the production of solid-state batteries or their electrolytes, as the process already is today in the diamond tool industry and is increasingly becoming in the friction lining industry.

References

- i *Taylor G.F.* U.S. Patent 1896854, "Apparatus for Making Hard Metal Compositions", granted February 7, 1933.
- ii *Schlieper, G.:* 2011 Hagen Symposium. A Review of Spark Plasma Sintering by Prof. Bernd Kieback.

FROM RESEARCH TO INDUSTRY - APPLICATIONS AND LATEST DEVELOPMENTS IN THE FIELD OF FAST/SPS SINTERING

- Website: International Powder Metallurgy Directory, accessed 04 January 2012.
- iii Electric Car Pros and Cons (Online).Source: <https://www.hpi.co.uk/content/electric-cars-the-electric-era/electric-car-pros-cons/> (accessed January 18, 2022).
- iv A new solid-state battery surprises the researchers who created it (Online). Source: https://ucsdnews.ucsd.edu/pressrelease/meng_science_2021 (accessed 18 January 2022)
- v Sun, C.; Liu, J.; Gong, Y; Wilkinson, D.P.; Zhang, J.: 'Recent advances in all-solid-state rechargeable lithium batteries', *Nano Energy*, vol. 33, pp. 363 - 386, 2017, doi: 10.1016/j.nanoen.2017.01.028
- vi Jackman, S.D.; Cutler, R.A.: "Effect of microcracking on ionic conductivity in LATP", *Journal of Power Sources*, issue 218, pages 65 - 75, 2012, doi: 10.1016/j.jpowsour.2012.06.081.
- vii Pasta, M. et al: "2020 roadmap on solid-state batteries," *J. Phys. Energy*, Aug. 2, no. 3, pp. 32008, 2020, doi: 10.1088/2515-7655/ab95f4
- viii Kerman, K.; Luntz, A.; Viswanathan, V.; Chiang, Y.-M.; Chen, Z.: 'Review - Practical Challenges Hindering the Development of Solid State Li Ion Batteries', *J. Electrochem. Soc.*, vol. 164, no. 7, A1731-A1744, 2017, doi: 10.1149/2.1571707jes.
- ix Wei, X.; Rehtin, J.; Olevsky, E.: "The Fabrication of All-Solid State Lithium-Ion Batteries via Spark Plasma Sintering", *Metals*, vol. 7, no. 9, pp. 372, 2017, doi: 10.3390/met7090372
- x Zhou, H., Liu, L.: "Emmerging applications of spark plasma sintering in all solid-state lithium-ion batteries and beyond", *Journal of Power Sources*, issue 391, pages 10-25, 21,doi: 10.1016/j.jpowsour.2018.04.054.
- xi Advanced Battery Market Size Worth Around US\$168.1 Bn by 2030 (Online). Source: www.precedenceresearch.com/advanced-battery-market (accessed 18 March 2022).
- xii Kreditanstalt für Wiederaufbau (KfW, Berlin). Source: [https://www.kfw.de/inlandsfoerderung/Unternehmen/Energie-Umwelt/Förderprodukte/Förderprodukte-\(S3\).html](https://www.kfw.de/inlandsfoerderung/Unternehmen/Energie-Umwelt/Förderprodukte/Förderprodukte-(S3).html)

DENSIFICATION AND CHARACTERIZATION OF PRESSURELESS SINTERED ZrB_2 -20 VOL% $MoSi_2$ ULTRA HIGH TEMPERATURE CERAMIC COMPOSITES

Manab Mallik¹, Mainak Saha^{1,2}, Sayantani Santra¹, Sushree Ananya Tanaya¹,
Sonam Kumari¹, and Divyadutta Behura¹

¹Department of Metallurgy & Materials Engineering, National Institute of Technology,
Durgapur, West Bengal, India

²Department of Metallurgical & Materials Engineering, Indian Institute of Technology,
Madras, Chennai, India.

mainaksaha1995@gmail.com

Abstract: Recently, there is an increasing interest towards fabricating complex-shaped boride based ceramic components with enhanced high-temperature properties for applications in extreme environments with temperatures exceeding 2000 °C. To this end, the current investigation reports on the pressure-less sintering of zirconium diboride based ceramic composites reinforced with 20 vol.% $MoSi_2$ particulate at 1700 °C for 2 h. The fabricated components are shown to exhibit ~74-98% of the theoretical density. The influence of compaction pressure on the mechanical properties and densification of ZrB_2 -20 vol.% $MoSi_2$ composites is investigated. Results highlight that an improvement in Young's modulus (by 142.10%), indentation fracture toughness (by ~95.65%) and hardness (by ~77.19%) may be achieved by increasing the compaction pressure from 127 to 381 MPa.

Keywords: Borides; Composites; pressureless sintering.

1. Introduction:

Zirconium diboride (ZrB_2) based ceramics find extensive applications as high-temperature structural components owing to a number of interesting properties which include enhanced strength at temperatures above 2000 °C combined with high melting temperature (~3250 °C), hardness (~14–23 GPa), and chemical inertness in acidic environments [1,2]. These properties render ZrB_2 -based ceramics an attractive option for application under extreme environments [3]. Besides, moderate electrical resistivity, high thermal conductivity and lower density as compared to the other ultra-high temperature ceramics (UHTCs) increases the potential of these ceramics for applications in sharp edges of hypersonic vehicles, various engine components, cladding of nuclear fuel, neutron absorbers, and concentrated solar thermal absorbers [1-6].

It is to be noted that poor oxidation resistance of monolithic ZrB_2 leads to unsatisfactory performances in extreme environments. Further, low self diffusivity arising due to a high level of covalent bonding makes it difficult to sinter monolithic ZrB_2 [3,4]. Full densification of this ceramic requires combination of high temperature and pressure [7]. However, addition of carbides, nitrides and silicides has been reported to enhance sinterability, mechanical, thermal, wear and creep properties [7-10]. However, enhancement of these properties is primarily dependent on the particle sizes of the reinforcements [9]. For instance, decreasing the particle size of SiC reinforcement from 9 to 6 μm has been reported to increase the four-point bending strength by ~125% in pressure-less sintered ZrB_2 -30 vol.% SiC composites [10]. Besides, both densification and vickers microhardness have been reported to increase by ~2.5% and 18.28% respectively with decreasing SiC particle size from 10 to 0.45

DENSIFICATION AND CHARACTERIZATION OF PRESSURELESS SINTERED ZrB_2 -20 VOL% $MoSi_2$ ULTRA HIGH TEMPERATURE CERAMIC COMPOSITES

μm in in pressure-less sintered ZrB_2 -30 vol.% SiC composites [10].

Molybdenum disilicide ($MoSi_2$) facilitates the sintering of ZrB_2 at temperatures at $1700^\circ C$ with or without application of pressure and improves oxidation behaviour of ZrB_2 above $1300^\circ C$ by formation of a borosilicate glassy layer. As a result, $MoSi_2$ is considered as a good additive to ZrB_2 based UHTCs [22]. Sintering of UHTCs are most commonly carried out by various hot pressing and sintering techniques such as, reactive hot pressing, spark plasma sintering, and pressure-less sintering. The comparatively high relative density obtained by hot pressing makes it the preferred route of processing of ZrB_2 based UHTCs although more complex shapes can be fabricated utilizing pressure-less sintering. The present study focuses the effect of compaction pressure on the density, microstructure and mechanical characteristics of ZrB_2 -20vol.% $MoSi_2$ composite. The rationale behind using 20 vol.% $MoSi_2$ as a reinforcement may be justified in terms of the optimised densification behaviour and high-temperature mechanical properties, as reported elsewhere [11-13]. For instance, increasing $MoSi_2$ content beyond 20 vol.% leads to degradation in high-temperature mechanical properties whereas decrease in the same below 20 vol.% leads to a decrease in sinterability [14-19].

2. Experimental:

High purity (99.5%) powders of ZrB_2 ($7.74 \pm 1.8 \mu m$) and $MoSi_2$ ($4 \pm 1.3 \mu m$) procured from Alfaaesar were selected as raw materials for the present study. Powders with composition of ZrB_2 -20 vol % $MoSi_2$ were blended in the Planetary Mono Mill at 250 rpm for 2h in acetone medium. After blending, powders were dried at $300^\circ C$ followed by crushing. This was followed by compaction under varying uniaxial pressure of 127, 254, and 381 MPa using hardened steel die and punch. Finally, green compacts were

densified by pressureless sintering at $1700^\circ C$ for 2 hrs. The aforementioned pressure values were obtained from the normalisation of applied compaction loads, viz. 1T, 2T and 3T with the specimen cross-sectional area ($\sim 7.87 mm^2$, in the present investigation). It needs to be mentioned that previous investigations on the pressure-less sintered ZrB_2 -20 vol % $MoSi_2$ composites have been performed with compaction pressures lesser than 350 MPa during cold isostatic pressing and with sintering temperatures between 1800 - $1850^\circ C$ [17, 18]. To this end, influence of compaction pressures less than and beyond 350 MPa at a relatively lower sintering temperature, viz. $1700^\circ C$ and the associated mechanical properties have been investigated in the present work to improve the understanding of the influence of compaction pressure at lower sintering temperatures on the mechanical properties of ZrB_2 -20 vol % $MoSi_2$ composites. Bulk density (BD) was analyzed with Archimedes principle, and densification parameters as well as shrinkage were calculated.

X-Ray Diffraction (XRD) (X' _Pert PRO, PANalytical, B. V. PW 3040/60 Netherlands) with Cu-K α radiation were utilized to carry out the analysis of phases in the as received powders, powder mixtures and sintered composites. Microstructural characterizations of as received powders and sintered pellets were done by FESEM (Zeiss-SIGMA) and EDS analyses.

Metallographic samples of sintered composites were prepared by polishing by abrasive silicon carbide papers (grit size 400 to 2000) followed by diamond discs. Finally, mirror polish was achieved using diamond paste. Ultrasonic cleaning of the polished specimens in acetone was carried out prior to examination under the microscope.

Elastic Modulus (E) of the ZM-20PS was calculated using Nielsen formula [2]

DENSIFICATION AND CHARACTERIZATION OF PRESSURELESS SINTERED ZrB₂-20 VOL% MoSi₂ ULTRA HIGH TEMPERATURE CERAMIC COMPOSITES

$$E = E_0 \frac{(1-P)^2}{1+(\rho^{-1}-1)P} \quad (1)$$

Here, E_0 = elastic modulus exclusive of porosity, $\rho = 0.4$ (Nielsen's factor) and P = porosity volume fraction. The E_0 has been calculated exercising the rule of the mixture (ROM) and modulus of elasticity of ZrB₂ and MoSi₂ as 500 GPa and 440 GPa, respectively. Vickers microhardness (using Matsuzawa-Hibiki) of the composites was obtained at 500gf for a dwell time of 15 seconds. On the other hand, indentation fracture toughness (K_{IC}) was obtained at 5 kgf (dwell time 15 s) using vickers microindenter. The value of K_{IC} was estimated by using the following relation [3]:

$$K_{IC} = 0.016 \left(\frac{E}{H} \right)^{1/2} \frac{F}{c^{3/2}} \quad (2)$$

Where E = modulus of elasticity, H = hardness, F = applied force, and $c = l + a$, where l = the crack length and a = half diagonal length of indentation, respectively.

3. Result & Discussion:

3.1 Powder characterization

The size, morphology and chemical composition of the as received ZrB₂ and MoSi₂ powders have been studied under FESEM and EDS (Fig.1). Raw powder characterization indicates that particle size of ZrB₂ powder is $7.74 \pm 1.8 \mu\text{m}$ and that of MoSi₂ powder is $4 \pm 1.3 \mu\text{m}$.

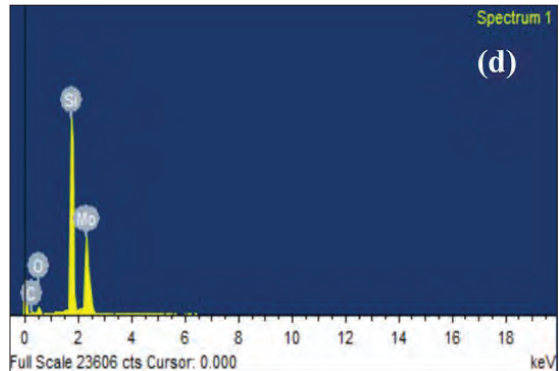
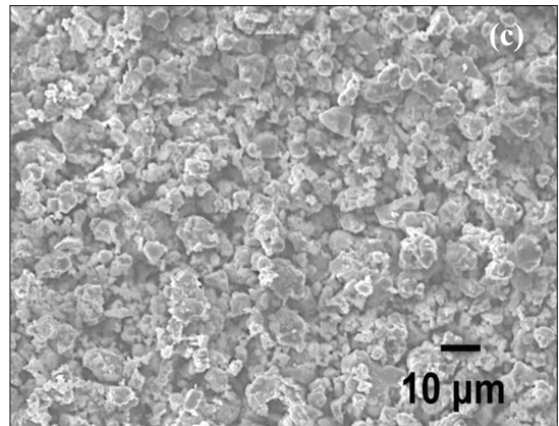
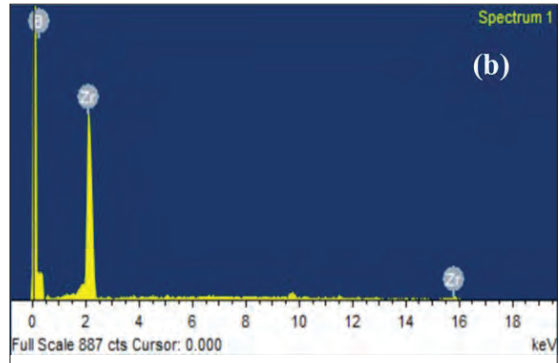
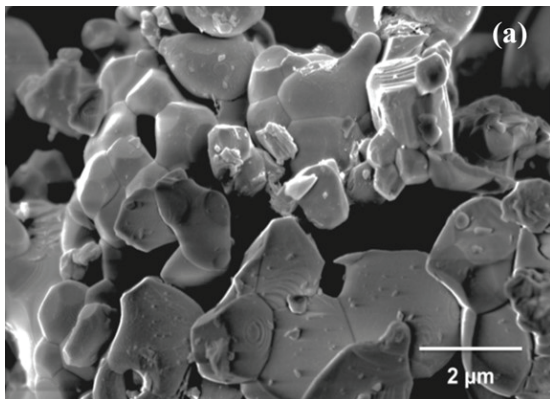


Figure 1: FESEM and EDS pattern of (a&b) ZrB₂ and (c&d) MoSi₂ powders

DENSIFICATION AND CHARACTERIZATION OF PRESSURELESS SINTERED ZrB_2 -20 VOL% $MoSi_2$ ULTRA HIGH TEMPERATURE CERAMIC COMPOSITES

3.2 Microstructure analysis

Results indicate that the relative density of the composites increases with increasing compaction pressure. Further more, Volume shrinkage and densification parameters increased with increasing compaction pressure. XRD analyses show peaks of ZrB_2 is the major constituent phase along with $MoSi_2$ for the samples prepared at $1700^\circ C$ (Figure 2a). The microstructure of composite compacted at 381 MPa pressure exhibits uniformly distributed ZrB_2 and $MoSi_2$ phases in the microstructure (shown in Figure 2b).

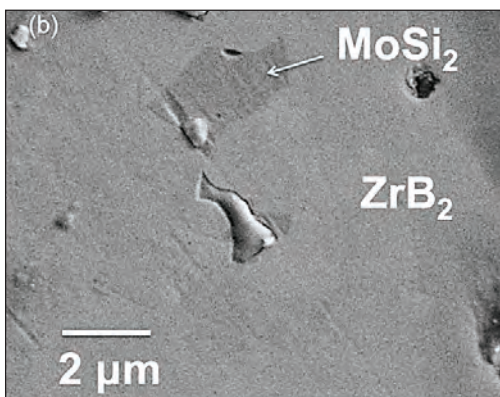
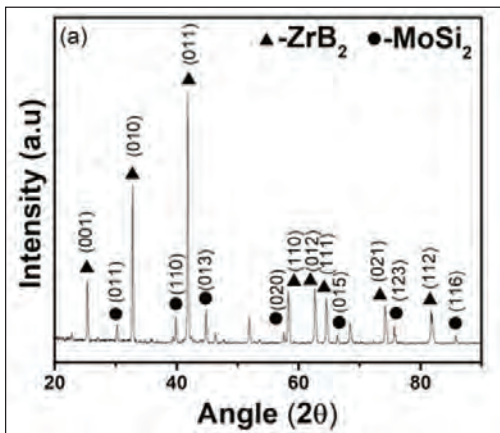


Figure 2: (a) XRD and (b) FESEM of ZM-20PS prepared by pressureless sintering at $1700^\circ C$

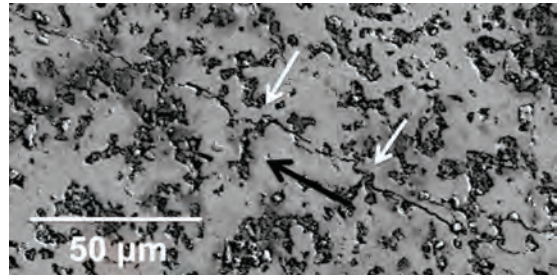


Figure 3. SEM image show crack propagation of ZM composite. Black and white arrows show the direction of crack extension and deflection, respectively.

The FESEM image of the ZM20-PS composite show two distinct phases in the microstructure, namely ZrB_2 and $MoSi_2$. The grains are irregular in shape throughout the microstructure.

3.3 Mechanical properties

Modulus of elasticity of the composite is enhanced by increasing the compaction pressure as higher compaction pressure improves densification through closure of larger fraction of pores, which in turn results in high elastic modulus (Table 1).

Table 1: Physical and mechanical properties of sintered composite

Compaction pressure MPa	Theoretical Density g/cm ³	Density, ρ g/cm ³	Relative density, ρ_r %	Elastic modulus, E GPa	Hardness, H _v GPa	Fracture toughness, K _{IC} MPa√m
127	6.1	4.5	74	190	5.7	2.3
254	6.1	5.5	90	345	7.4	3.4
381	6.1	6	98	460	10.1	4.5

The mechanical properties of ZrB_2 - $MoSi_2$ composite are summarized in Table 1. It is observed that an enhanced compaction pressure increases both the mechanical properties of the composites.

An increase in the density with the increase in compaction pressure results in the enhancement of the hardness, as hardness is proportional to specific density. The indentation crack (shown in Figure 3) indicates that interaction of the crack

DENSIFICATION AND CHARACTERIZATION OF PRESSURELESS SINTERED ZrB₂-20 VOL% MoSi₂ ULTRA HIGH TEMPERATURE CERAMIC COMPOSITES

with MoSi₂ particles leads to crack deflection. It may be observed from the white arrows in Figure 3 that crack deflection mostly occurs along the ZrB₂/MoSi₂ interface leading to toughening through fibre pull-out mechanism [20]. Besides the higher room temperature thermal expansion coefficient of MoSi₂ ($\sim 7 \times 10^{-6} \text{ K}^{-1}$) as compared to that of non-reinforced ZrB₂ ($\sim 5.3 \times 10^{-6} \text{ K}^{-1}$) may result in the development of radial tension and hoop compression stress field around MoSi₂ leading to crack deflection, as also discussed elsewhere [20]. Besides, the compressive stress field around MoSi₂ particles may also be attributed to cause crack deflection. One of the theories on the crack deflection mechanism in composites suggests that the presence of rod-shaped second phase particles is the most effective in enhancing toughness through crack deflection [21]. However, an in-depth examination the crack deflection mechanism in the present material that necessitates detailed microstructural investigations is part of an ongoing study and is also beyond the present scope of discussion.

4. Conclusion:

Densification of ZrB₂-20 vol% MoSi₂ under various compaction pressures and their physical and mechanical properties have been studied. The important conclusions drawn from the results and discussions of this study have been elucidated here

- i) The density of the composite increases with increasing compaction pressure.
- ii) An enhanced compaction pressure increases the elastic moduli, hardness and fracture toughness of the composites.
- iii) Interaction of the indentation crack with MoSi₂ particles plausibly leads to crack deflection resulting in enhanced fracture toughness through fibre pull-out mechanism.
- iv) A comparison of the results with the previous investigation in this direction [17] indicates

that compaction pressures exceeding 350 MPa with lower sintering temperatures ($\sim 1700^\circ\text{C}$) leads to $\sim 95.65\%$ increase in indentation fracture toughness of pressureless sintered ZrB₂-20 vol% MoSi₂ composites but results in $\sim 36.88\%$ and ~ 5.9 decrease in vickers microhardness and elastic modulus respectively of the aforementioned composite.

Acknowledgements

The authors would like to thank the technical personnel at COE, NIT Durgapur. The authors are thankful to X-ray diffraction lab operator Mr. Hiranmoy Bairagya for capturing XRD data.

References

- [1] B.R. Golla, A. Mukhopadhyay, B. Basu, S.K. Thimmapp, Review on ultra-high temperature boride ceramics, Prog. Mater. Sci. 111 (2020) 100651
- [2] R.A. Cutler, Engineering properties of borides, in: S.J. Schneider (Ed.), Ceramics and Glasses, Engineered Materials Handbook, ASM International, Materials Park, OH, 1992, pp. 787–803.
- [3] M. Mallik, A.J. Kailath, K.K. Ray, R. Mitra, Effect of SiC content on electrical, thermal and ablative properties of pressureless sintered ZrB₂-based ultra-high temperature ceramic composites, J. Eur. Ceram. Soc. 37 (2017) 559–572.
- [4] M. Mallik, A.J. Kailath, K.K. Ray, R. Mitra, Electrical and thermophysical properties of ZrB₂ and HfB₂ based composites, J. Eur. Ceram. Soc. 32 (2012) 2545–2555.
- [5] M. Natali, J.M. Kenny, L. Torre, Science and technology of polymeric ablative materials for thermal protection systems and propulsion devices: A review, Prog. Mater. Sci. 84 (2016) 192–275.
- [6] Q. Han, C. Sun, Y. Tao, Z. Li, Y. Zhang, Y. Che, Thermal protection of a hypersonic vehicle by modulating stagnation-point heat flux, Aerosp. Sci. Technol. 98 (2020) 105673.
- [7] M. Mallik, K.K. Ray, R. Mitra, Oxidation behavior of hot pressed ZrB₂-SiC and HfB₂-SiC composites, J. Eur. Ceram. Soc. 31 (2011) 199–215.

DENSIFICATION AND CHARACTERIZATION OF PRESSURELESS SINTERED ZrB_2 -20 VOL% $MoSi_2$ ULTRA HIGH TEMPERATURE CERAMIC COMPOSITES

- [8] T.R. Paul, M.K. Mondal and M. Mallik, Densification behavior of ZrB_2 - $MoSi_2$ - SiC_w composite processed by multi stage spark plasma sintering, *Ceram. Int.* 47(22) (2021) 31948-31972.
- [9] M. Mallik, S. Roy, K.K. Ray, R. Mitra, Effect of SiC content, additives and process parameters on densification and structure-property relations of pressureless sintered ZrB_2 -SiC composites, *Ceram. Int.* 39 (2013) 2915-2932.
- [10] S. Zhu, W.G. Fahrenholtz, G.E. Hilmas, Influence of silicon carbide particle size on the microstructure and mechanical properties of zirconium diboride-silicon carbide ceramics, *Journal of the European Ceramic Society.* 27(2007)2077-2083.
- [11] M. Mallik, S. Pan, H. Roy, Fracture toughness measurement of hot pressed ZrB_2 - $MoSi_2$ composite, *Int. J. Curr. Eng. Technol.* 3(2013)1647-1652.
- [12] M. Mallik, P. Mitra, N. Srivastava, A. Narain, S.G. Dastidar, A. Singh, T.R. Paul, Abrasive wear performance of zirconium diboride based ceramic composite, *Int. J. Refract. Metals Hard Mater.* 79 (2019) 224-232.
- [13] T.R. Paul, M.K. Mondal, M. Mallik, Dry sliding wear response of ZrB_2 -20vol.% $MoSi_2$ composite, *Mater. Today Proc.* 5 (2018) 7174-7183.
- [14] T.R. Paul, M.K. Mondal, M. Mallik, Abrasive wear performance and wear map of ZrB_2 - $MoSi_2$ - SiC_w composites, *J. Eur. Ceram. Soc.* 41 (2021) 3227-3251.
- [15] R. Mitra, S. Upender, M. Mallik, S. Chakraborty, K.K. Ray, Mechanical, thermal, and oxidation behavior of zirconium diboride based ultra-high temperature ceramic composites, *Key Eng. Mater.* 395 (2009) 55-68.
- [16] M. Mallik, S. Upender, R. Mitra, K.K. Ray, Thermal shock and ablation resistance of ZrB_2 based ultra-high temperature ceramic composites, in: K.K. Kar, K. Muralidhar, J. Ramkumar (Eds.), *Proceeding in International Conference on Future Trends in Composite Materials and Processing INCCOM-6*, vols. 12-14, Anamaya Publications, IIT Kanpur, December 2007, pp. 670-675.
- [17] D. Sciti, S. Guicciardi, A. Bellosi, G. Pezzotti, Properties of a pressureless-sintered ZrB_2 - $MoSi_2$ ceramic composites, *J. Am. Ceram. Soc.* 89 (2006) 2320-2322.
- [18] D. Sciti, M. Brach, A. Bellosi, Long-term oxidation behavior and mechanical strength degradation of a pressurelessly sintered ZrB_2 - $MoSi_2$ ceramic, *Scr. Mater.* 53 (2005) 1297-1302.
- [19] S. Guo, T. Nishimura, T. Mizuguchi, Y. Kagawa, Mechanical properties of hot-pressed ZrB_2 - $MoSi_2$ -SiC composites, *J. Eur. Ceram. Soc.* 28 (2008) 1891-1898.
- [20] K. Xia, T.G. Langdon, The toughening and strengthening of ceramic materials through discontinuous reinforcement. *J Mater Sci* 29 (1994)5219-5231
- [21] K.T. Faber, A.G. Evans. Crack deflection processes—I. Theory. *Acta metallurgica* 31(1983)565-76.

FABRICATION AND CHARACTERIZATIONS OF CARBON NANOTUBE DISPERSED ALUMINUM COMPOSITES

Saptarshi Saha¹, Lokesh Sarkar², Apurba Das^{*3}, Arijit Sinha¹

¹ Department of Metallurgical Engineering, KaziNazrul University, Asansol, West Bengal, India

¹ School of Laser Science and Engineering, Jadavpur University, Kolkata, West Bengal, India.

³ Department of Aerospace and Applied Mechanics, IEST, Shibpur, Howrah, West Bengal, India.

saptarshi.saheb.saha@gmail.com

Abstract: Fabrication and mechanical behaviour of carbon nanotubes (CNT) dispersed aluminum nanocomposites are presented in this work for possible use in different engineering and structural applications. CNT dispersed aluminum nanocomposites are fabricated using Aluminum powder and CNT flakes through powder metallurgy technique. Three different weight percentages of CNT (0.5%, 1%, and 1.5%) are considered for sample preparation along with the pure aluminum sample. The morphological features of CNT dispersed aluminum nanocomposites were observed using an optical microscope. The consolidation was observed through the estimation of the density of the prepared samples. Mechanical property in terms of compressive strength was evaluated by Instron tensile testing machine along with the Rockwell hardness (in B scale). 1.5% CNT dispersed aluminum nanocomposites exhibit around 20% enhancement in the compressive strength value along with 45% increment in the hardness value.

Keywords: Aluminum powder; CNT; Nanocomposite; Hardness; Compressive strength

1. Introduction

Research on composites with aluminum matrix reinforced with various particles has increased in recent years due to their advantages, which include good machinability, low coefficients of thermal expansion, lightweight, and excellent mechanical properties. Composites mainly used in aviation, energy and lightweight applications are stiffer and stronger than conventional materials [1-4]. Aluminum matrix nanocomposites have received a lot of research because of their unique properties, including good corrosion resistance, excellent strength-to-weight ratio, ductility, and a wide range of applications [5]. Solid-state, liquid-state, and semi-solid-state methods can be employed to manufacture metal matrix composites. Solid-state method among these three [6] are considered. Aluminum metal matrix composites (MMC) are used in numerous applications in the field of aviation, automobile because of their good wear resistance, high strength, and low density compared to other conventional metals. High

specific stiffness and high strength aluminum metal matrix composites can be used in long-term applications where saving weight is a priority, such as high-speed rotating, robotics, automotive engine parts, high-speed machinery, shafts, military powertrain, brake parts and suspension components [7]. The advantages of aluminum hybrid composites over conventional aluminum alloys include inaccessibility to conventional processing techniques, the possibility to reduce production costs, and improved mechanical properties. Composite materials can be micro composites or nano composites depending on the type of reinforcement phase. In micro composite, the size of the reinforcement phase is in the micrometer size, while, in the nanocomposite, the size of the reinforcement phase is nanometer size. CNT particles up to a specific weight percentage can be reinforced in aluminum MMCs to increase the compressive strength and hardness of the material. Material properties are different based on the percentage reinforcement of CNT particles. Comprehensive

FABRICATION AND CHARACTERIZATIONS OF CARBON NANOTUBE DISPERSED ALUMINUM COMPOSITES

knowledge of the properties is necessary for the intended use for the specific application. In this work, an effort has been made to investigate the effect of CNT percentage in aluminum nanocomposite [8-9]. In the development of aluminum matrix composite, carbon nanotubes (CNTs) can be used as a potential reinforcement [10-11]. Previous investigations have shown that the self-lubricating properties of CNTs reduce wear and friction between the surfaces of MMC because CNTs produce a film between surfaces that act as a lubricant during sliding [13-14].

From this past literature, it is evident that not much work has been done on the fabrication and characterizations of carbon nanotube dispersed aluminum composites. In this study fabrication of carbon nanotube dispersed aluminum composites are performed and the friction, wear properties along with the hardness and compression strength of nanocomposites of the developed samples is evaluated.

2. Experimental

2.1 Materials

In this work, metal matrix composites were prepared using aluminum as the matrix phase while carbon nanotube (CNT) was considered as the reinforcing phase. The specification of the aluminum powder and CNT powder used for this work is provided in table 1.

Table.1 Specification of the matrix and reinforcement particle

Serial No.	Materials	Specification
1	Aluminum powder	Make- M/S Loba Chemicals Private Limited, Mumbai, melting point- 660°C, purity-98%, fine grain
2	CNT powder (flakes size)	Make- M/S Ad-Nano Technologies Pvt. Ltd, Karnataka, purity: 99%, diameter: 10-15 nm

2.2 Sample preparation:

Aluminum powder and CNT powder (flakes size) are used in specific weight percentages and measured using a digital weight machine. The centre lathe is used for mixing aluminum matrix and reinforcement CNT powder. A cylindrical steel container ($\Phi 50$ mm, length 76 mm) was used during the ball milling process for mixing

the reinforcement particle in the matrix phase. As grinding media, stainless steel balls were used. The container was rotated at 130 rpm both anticlockwise and clockwise directions for 50 minutes in order to ensure homogeneous mixing of aluminum and CNT powder. Universal testing machine is used to press powdered mixtures uniaxially at ambient temperature in specially designed steel dies to obtain cylindrical specimens of approximately $\Phi 10.5$ mm and height 30.5 mm shown in Fig.1 after ball milling, applying a pressure of about 640 MPa for about 2 minutes. The sintering process is an essential technique for improving particle adhesion in powder metallurgy. In sintering, the green compact is heated to a temperature below the melting point of the matrix phase in an inert environment. The compacted green sample was sintered at a temperature of 600 °C while a vacuum was maintained within the vacuum furnace. When the temperature reaches, it is held in place for a short period of time. Holding time is required in order for grains to be formed and to grow. During the sintering process, a high-temperature tube furnace was used to prevent oxidation. This technique produces four different types of samples containing 0, 0.5, 1, and 1.5 percent of CNT. Each variety four samples are considered, and total 16 samples are prepared for the present study.



Fig.1. fabricated sample

FABRICATION AND CHARACTERIZATIONS OF CARBON NANOTUBE DISPERSED ALUMINUM COMPOSITES

2.3 Characterizations of Nanocomposites

The density of the specimens was determined by the weight and dimension of each specimen ($\rho = m/V$). Green density is measured before sintering, while sintering density is measured after sintering. A Rockwell hardness tester was used to measure specimen hardness in B scale with a constant load of 100 Kgf and a steel ball indenter of 1/16 in. The samples were tested for compressive strength using a universal testing machine. Measurements of the compressive strength were performed on cylindrical specimens having a diameter of approximately 10.5 mm and a length of approximately 30.5 mm. The diameter of the sample increased during compression testing, while the length decreased. From the display of the machine, can obtain the final reading of specimens. Wear and friction properties were measured using a pin on a disc tribo-meter in dry sliding conditions on a wear and friction monitoring machine (TR201, DUCOM Triboinnovators). The tests are in two sections, first by keeping the load constant at 40 N and varying the speed at 500 rpm, 550 rpm, and 600 rpm, then by keeping the speed at 550 rpm while varying the load at 35 N, 40 N, and 45 N. A steel counter surface disc was rotated while the cylindrical sample was fixed in a holder and positioned vertically on its surface. Wear rate by removing material from the cylindrical specimen in contact with the rotating disc was measured following the ASTM G99 standard. The wear rate (W_r) has been calculated using the following formula [14]:

$W_r = W_v / \{T \times (\pi DN / 1000) \times F\}$ where, W_v = wear volume (in mm^3), T = time of rotation (in minute), D = diameter of track in mm, N = rpm, F = applied load (in N), W_r = wear rate (in mm^3/Nm). The surface microstructure of samples was examined with a metallurgical microscope (Leica Model-

DM270M). To examine the microstructure of specimens, emery paper was used to polish them and the acid solution was used for etching (distilled water-92ml, hydrofluoric acid-2ml, and nitric acid-6 ml). A solution of this chemical has been used to etch the polished sample surfaces in order to observe the grains more clearly.

3. Results and Discussion:

Mechanical properties and photomicrograph and of the aluminum matrix nanocomposites reinforced with CNT are characterized by using various techniques. The details of the analysis and obtained results are discussed in the following sections.

3.1 Density

The green and sintered density of the samples has been determined and shown in Fig.2. It is observed that the maximum density is found in pure aluminium, and it decreases as the reinforcement percentage increases [15]. Because the density of the reinforcement used here is much lower than that of the pure metal because CNTs have lower density as compared to aluminium. Thus, aluminium nanocomposites reinforced with 1.5% CNTs exhibit minimum density. The sintered density of aluminium-based metal matrix nanocomposites is higher than the green density because of increased cohesion between the particles during sintering.

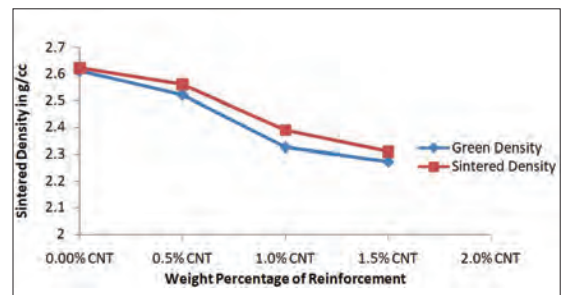


Fig.2. Green and sintered densities of CNT reinforced samples

FABRICATION AND CHARACTERIZATIONS OF CARBON NANOTUBE DISPERSED ALUMINUM COMPOSITES

3.2 Microstructure of composites

The microstructure of the samples has been observed with the help of Leica microscope to study the morphological features. The Keller's reagent has been used for etching purpose to get a distinct view of the grains and

its boundaries [16]. The microstructure with different CNT percentages is shown in Fig.3. The microstructure with 1% and 1.5% CNT sample clearly indicates the distinct grain boundary of the same. 1.5% CNT samples very few pores in the microstructure, indicating poor compaction.

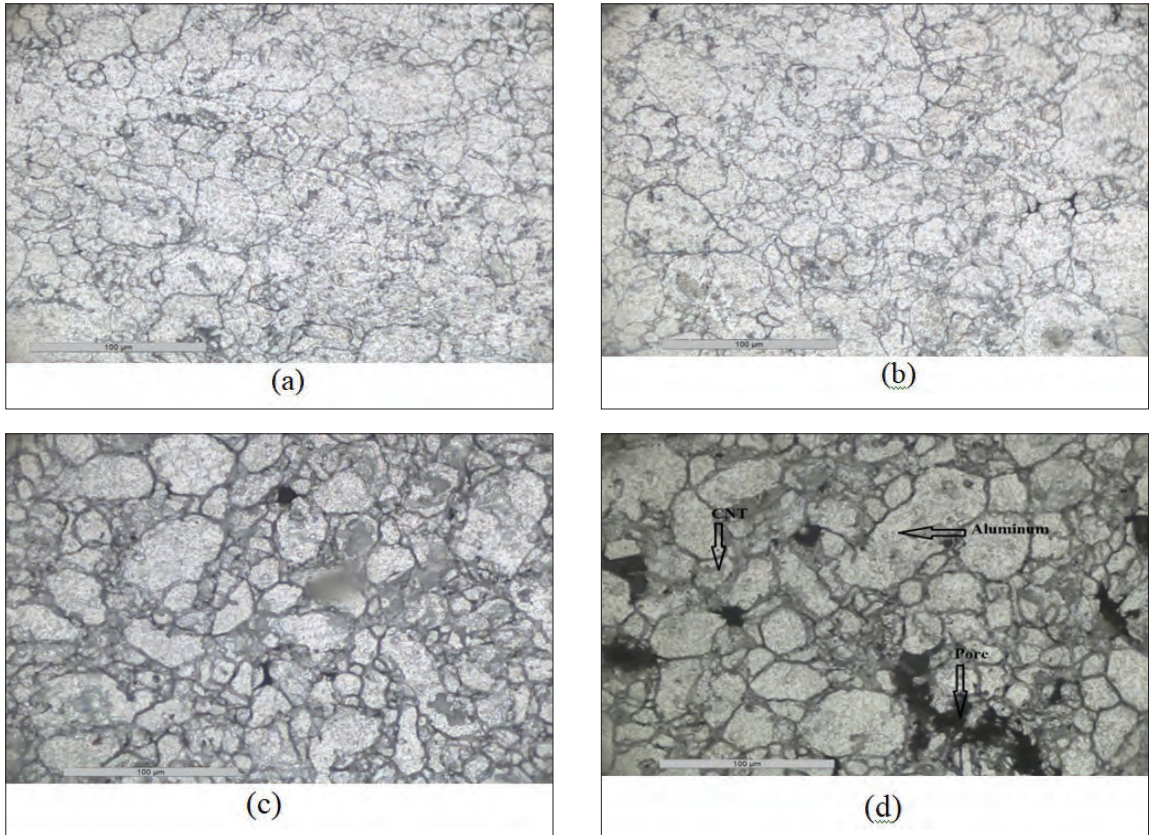


Fig 3. Photomicrograph of (a) pure aluminum-0% CNT (b) with 0.5% (c) 1% CNT (d) 1.5% CNT

3.3 Friction and wear properties of nanocomposites

Different percentages of CNT reinforcement at different loads have been shown to affect wear rate in Fig.4 and the variation in wear rate is shown in Fig.5 for different percentages of CNT reinforcement at various rotational speeds. On the wear and friction monitoring machine, samples

of pure aluminium and its composites have been tested for wear and friction [17]. The tests were conducted in two sections, first, a constant 40 N load was applied with variable speed at 550 rpm, 600 rpm and 650 rpm, and second, a constant 540 rpm speed was applied with varying loads at 40 N, 45 N, and 50 N. A 60 mm disk track diameter was taken and each test was conducted for 10

FABRICATION AND CHARACTERIZATIONS OF CARBON NANOTUBE DISPERSED ALUMINUM COMPOSITES

minutes. In the first section of the test, the load was set at 40 N and the speed varied different rpm. From the experimental results, 1.5% CNT reinforced aluminium composite at 500 rpm speed has the lowest wear rate, while pure aluminium at 650 rpm speed has the maximum wear rate. In comparison to unreinforced matrix, composite specimens showed a lower wear rate.

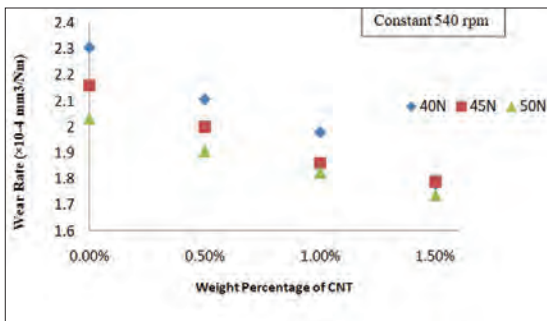


Fig.4. Effect of load on the wear rate for CNT reinforced aluminium composite

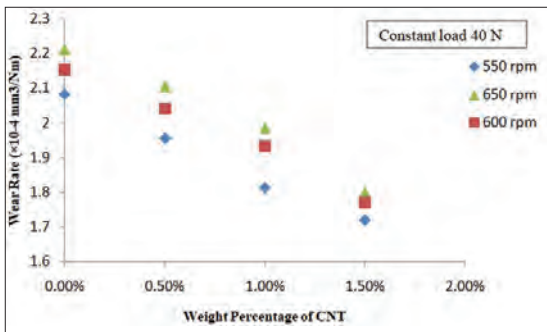


Fig.5. Effect of rpm on the wear rate for CNT reinforced aluminium composite.

3.4 Hardness and compression strength of nanocomposites

Compressive test and hardness value of the sample at different composition are also determined. It has been observed that compressive strength as well as hardness increase with an increase in CNT content. Rockwell hardness of different samples of various compositions has been shown

in Fig.6. The maximum compressive strength and hardness is obtained with 1.5 wt. percentage of CNT due to better dispersion of the same with the aluminum matrix [18-20]. Fig. 7 shows the compression strengths of composite materials containing CNT. The experimental results shown CNT reinforcement in an aluminum matrix of 1.5 wt% showed the greatest compression strength. Aluminum particles have been bridged with carbon nanotubes. As a result of bridging, cavities are filled and strength is increased [21].

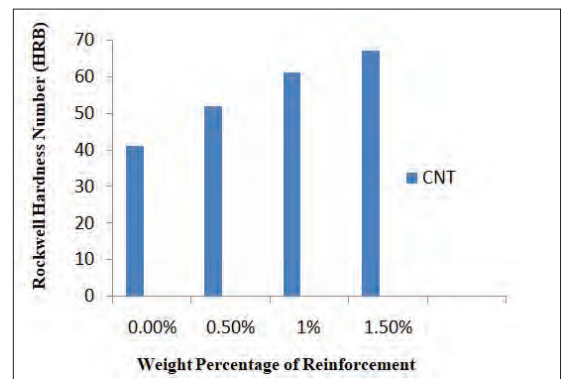


Fig.6. Hardness of different compositions CNT reinforced samples

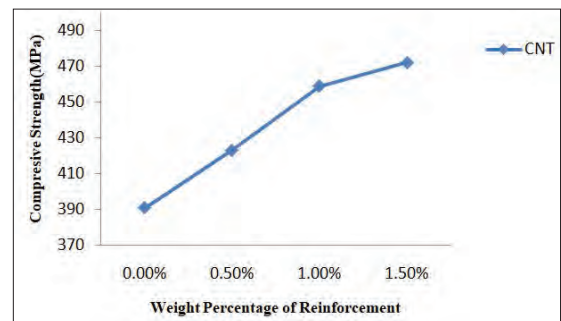


Fig.7. Variation of compression strength of nanocomposites

Conclusions: According to this study, Aluminum MMC can be replaced with other conventional metals in order to achieve better performance and longer life. Aluminum

FABRICATION AND CHARACTERIZATIONS OF CARBON NANOTUBE DISPERSED ALUMINUM COMPOSITES

composites are a new type of MMC that has the ability to fulfill the increasing needs of advanced technical applications. Because CNT has a lower density than aluminum, the green and sintered densities of the nanocomposites declined somewhat as the CNT content in the aluminum matrix rose. The sintered density of aluminium-based metal matrix nanocomposites is higher than the green density because of increased cohesion between the particles during sintering. CNT reinforced aluminum nanocomposites show enhancement in the compressive strength as well as in hardness compared to that of pure aluminum. Compressive strength and hardness is observed to increase by around 20% and 45% with the incorporation of 1.5% CNT within the aluminum matrix. Wear and friction behaviour of developed composite reduces with higher CNT concentration in the aluminum matrix. The metallurgical microscope revealed a uniform dispersion of the CNT reinforcement particle in the aluminum metal matrix. There are no pores present in the samples, indicating good compaction has achieved.

References:

- [1] Bodunrin, Michael Oluwatosin, Kenneth Kanayo Alaneme, and Lesley Heath Chown. "Aluminium matrix hybrid composites: a review of reinforcement philosophies; mechanical, corrosion and tribological characteristics." *Journal of materials research and technology* 4, no. 4 (2015): 434-445.
- [2] Harichandran, R., and N. Selvakumar. "Effect of nano/micro B4C particles on the mechanical properties of aluminium metal matrix composites fabricated by ultrasonic cavitation-assisted solidification process." *Archives of civil and mechanical engineering* 16, no. 1 (2016): 147-158.
- [3] Valibeygloo, N. R. Azari Khosroshahi, and R. Taherzadeh Mousavian. "Microstructural and mechanical properties of Al-4.5 wt% Cu reinforced with alumina nanoparticles by stir casting method." *International Journal of Minerals, Metallurgy, and Materials* 20, no. 10 (2013): 978-985.
- [4] Kim, H. H., J. S. S. Babu, and C. G. Kang. "Fabrication of A356 aluminum alloy matrix composite with CNTs/Al₂O₃ hybrid reinforcements." *Materials Science and Engineering: A* 573 (2013): 92-99.
- [5] Alaneme, Kenneth Kanayo, and Kazeem Oladiti Sanusi. "Microstructural characteristics, mechanical and wear behaviour of aluminium matrix hybrid composites reinforced with alumina, rice husk ash and graphite." *Engineering Science and Technology, an International Journal* 18, no. 3 (2015): 416-422.
- [6] Chen, B., K. Kondoh, H. Imai, and J. Umeda. "Effect of initial state on dispersion evolution of carbon nanotubes in aluminium matrix composites during a high-energy ball milling process." *Powder Metallurgy* 59, no. 3 (2016): 216-222.
- [7] S. T. Mavhungu, E. T. Akinlabi, M. A. Onitiri, and F. M. Varachia. "Aluminum matrix composites for industrial use: advances and trends." *Procedia Manufacturing* 7 (2017): 178-182.
- [8] A. Reeb, V. Walter, V. Schulze, and K. A. Weidenmann. "Characterization of a Hybrid Al₂O₃-Aluminum Matrix Composite Manufactured Via Composite Extrusion," *Journal of Composite Materials*, Vol. 50, no. 8, pp. 1099-1108, 2016.
- [9] B. C. Kandpal, J. Kumar, H. Singh, "Fabrication and Characterisation of Al₂O₃/Aluminium Alloy 6061 Composites Fabricated by Stir Casting" *Materials Today*, Vol. 4, pp. 2783-2792, 2016
- [10] Harris, Peter JF. "Carbon nanotube composites." *International materials reviews* 49, no. 1 (2004): 31-43.
- [11] Bakshi, Srinivasa R., Debrupa Lahiri, and Arvind Agarwal. "Carbon nanotube reinforced metal matrix composites-a review." *International materials reviews* 55, no. 1 (2010): 41-64.
- [12] Kuzumaki, Toru, K. Miyazawa, Hideki Ichinose, and Kunio Ito. "Processing of carbon nanotube reinforced aluminum composite." *Journal of materials Research* 13, no. 9 (1998): 2445-2449.
- [13] Berger, Claire, Zhimin Song, Tianbo Li, Xuebin Li, Asmerom Y. Ogbazghi, Rui Feng, Zhenting Dai et al. "Ultrathin epitaxial graphite: 2D electron gas properties and a route toward graphene-based nanoelectronics." *The Journal of Physical Chemistry B* 108, no. 52 (2004): 19912-19916.

FABRICATION AND CHARACTERIZATIONS OF CARBON NANOTUBE DISPERSED ALUMINUM COMPOSITES

- [14] Harris, Peter JF. "Carbon nanotube composites." *International materials reviews* 49, no. 1 (2004): 31-43.
- [15] Garg, Pulkit, Pallav Gupta, Devendra Kumar, and Om Parkash. "Structural and mechanical properties of graphene reinforced aluminum matrix composites." *J. Mater. Environ. Sci* 7, no. 5 (2016): 1461-1473.
- [16] Choi, H. J., G. B. Kwon, G. Y. Lee, and D. H. Bae. "Reinforcement with carbon nanotubes in aluminum matrix composites." *Scripta Materialia* 59, no. 3 (2008): 360-363.
- [17] Singla, Devanshu, Kaza Amulya, and Qasim Murtaza. "CNT reinforced aluminium matrix composite-a review." *Materials Today: Proceedings* 2, no. 4-5 (2015): 2886-2895.
- [18] KS, Lokesh, I. C. Chethan, K. R. Naveen Kumar, Vinayaka Kannantha, and Naveen Kumar JR. "Determination of compressive strength of graphene reinforced with aluminium-7075 metal matrix composites." (2018).
- [19] Rajmohan, T., K. Palanikumar, and S. Ranganathan. "Evaluation of mechanical and wear properties of hybrid aluminium matrix composites." *Transactions of nonferrous metals society of China* 23, no. 9 (2013): 2509-2517.
- [20] Khanna, Virat, Vanish Kumar, and Suneev Anil Bansal. "Mechanical properties of aluminium-graphene/carbon nanotubes (CNTs) metal matrix composites: Advancement, opportunities and perspective." *Materials Research Bulletin* 138 (2021): 111224.
- [21] L. Shahrđami, A. Sedghi, and M. H. Shaeri. "Microstructure and mechanical properties of Al matrix nanocomposites reinforced by different amounts of CNT and SiCW." *Composites Part B: Engineering* 175 (2019): 107081.

A SHORT REVIEW ON THE EFFECT OF CERAMIC PARTICLES, MWCNT, AND GRAPHENE ON THE PROPERTIES OF Cu MATRIX COMPOSITES BY POWDER METALLURGY ROUTE

Saroj Kumar Sahu^a, Suhree P Mohapatra^a, Dinesh Kumar Mishra^a, Renu Prava Dalai^a

^aDepartment of Metallurgical & Materials Engineering,
Veer Surendra Sai University of Technology, Burla, India.

sahoosaroj234@gmail.com

Abstract: Copper in pure form is applicable in many electrical applications because of its higher electrical and thermal conductivity. But leaner physical and mechanical properties restrict its application in various fields where demand for high tensile and wear resistance is needed. Past research experiments on Cu and its alloys have shown that the addition of high-strength nanoparticles like Titanium Chloride(TiC), Silicon carbide(SiC), Titanium dioxide(TiO₂), Aluminum oxide(Al₂O₃), Multiwalled carbon nanotubes(MWCNT), Carbon nanotube(CNT), Graphene, etc., improves the tensile and wear resistance properties. While simultaneously, the corrosion resistance and thermal conductivity properties deteriorate. Fabrication of the Cu matrix composites by powder metallurgy process is a low-temperature processing method, which provides better properties. This review work gives an idea about the effect of nanoparticles on the properties of Cu.

Keywords: Powder metallurgy; nanoparticles; CNT; Graphene; mechanical properties; wear

1. Introduction

Copper and its alloys have low strength and hardness, with poor tribological properties restricting their practical applications in many fields [1-2]. High loads or high sliding speeds in friction and wear processes fail Cu and its alloys. Composite materials contain two or more constituents having different physical, chemical, and mechanical properties [3]. In composite materials, the matrix provides ductility and toughness. The reinforcement gives high modulus and strength. In recent years the development of advanced metal matrix nanocomposites for structural engineering and functional devices are generated new materials like CNT and Graphenes. Graphite, carbon nanotubes (CNTs), and graphene possess unique electrical, mechanical, and thermal properties [4]. A nanomaterial refers to a material, at least one dimension in a three-dimensional space or composition to a nanoscale (1-100 nm). MMCs hold the opportunity to change the properties of Cu by adding a suitable reinforcement

phase [5]. SiC to meet the demands for high thermal conductivities in thermal management applications. Thermal conductivity decreases with a decrease in particles of SiC. Electrical conductivity increases with increasing particle sizes but decreases with increasing volume fraction of SiC in the copper matrix [6-7]. For the Cu-TiC composite, tensile properties increase with the addition of TiC. There is a significant increase in the tensile properties due to the addition of graphene along with TiC. The Vickers hardness values also enhanced significantly with the addition of TiC and graphene. The addition of graphene in the Cu-TiC composites shows an increment in thermal conductivity [8]. Reinforcement of Cu with different hard ceramic particles like Al₂O₃, SiC, TiO₂, and TiC in the form of MMCs improves the mechanical properties of Cu. The SWCNT(single walled carbon nanotube) is very useful for electrical and electronics applications. MWCNT reinforcement improves strength and hardness. The thermal conductivity value decreases drastically with

A SHORT REVIEW ON THE EFFECT OF CERAMIC PARTICLES, MWCNT, AND GRAPHENE ON THE PROPERTIES OF Cu MATRIX COMPOSITES BY POWDER METALLURGY ROUTE

an increase in MWCNT weight percentage. So, it is clear that the thermal conductivity of Cu is superior to MWCNT particles. With a higher wt% of MWCNT, the thermal conductivity of the composites gets reduced due to cluster formation [9].

2. Effect of Al_2O_3 nanoparticles on Cu matrix composite

Al_2O_3 nanoparticles reinforced Cu matrix composites have many electrical applications due to their high electrical and thermal conductivity [10]. Li et al., developed Cu matrix composite reinforcing with the Al_2O_3 nanoparticles by powder metallurgy process. They studied the tribological behavior of the composite by a ring-on-block sliding friction test. According to their results, the hardness and wear resistance of the composites increase with the reinforcement of Al_2O_3 nanoparticles [11]. L Rajesh Kumar and K.S Amirthagadeswaran studied the wear and corrosion behavior of the Al_2O_3 nanoparticles on Cu matrix composite fabricated by high-energy ball milling. They observed that 10-15wt% reinforcement of the Al_2O_3 nanoparticles improves the corrosion and wear properties of the Al_2O_3 nanoparticles reinforced Cu matrix composite [12]. ViselavaRajkovic et al., observed that the simultaneous addition of the nano- and micro-sized Al_2O_3 particles improves the microhardness of the Cu matrix composite [13].

3. Effect of TiC nanoparticles on Cu matrix composite

Nawal Ali Abd et al., reinforced both micro and nano-size TiC particles into the Cu matrix and observed that the addition of nano TiC particles enhances the microhardness values of the developed composite than the micro TiC particles [14]. Nalin Somani and Nitin Kumar Gupta analyzed the effect of TiC nanoparticles on the microstructural and tribological properties

of Cu-TiC nano-composites. They developed the Cu-TiC nanocomposites using the powder metallurgy process by varying the wt% of TiC particles from 0-20%. According to their research findings reinforcement of TiC nanoparticles improves the hardness, tensile strength, and wear resistance of the Cu-TiC nanocomposite [15].

4. Effect of SiC nanoparticles on Cu matrix composite

Reinforcement of SiC nanoparticles into the metal matrix provides higher mechanical strength, thermal conductivity, low density, low coefficient of thermal expansion (CTE), and good electrical conductivity [16]. Akbarpour et al., developed Cu matrix nanocomposite by reinforcing SiC nanoparticles with high energy mechanical milling. According to their findings, the densification percentage significantly decreases with the milling time. However, a slight decrease in densification percentage with an increasing the amount of SiCwt% [17]. Essam et al., developed a Cu-SiC nanocomposite through mechanical alloying and studied the microstructure, mechanical and thermal properties of the developed composite. According to their research finding there is an enhancement in the mechanical properties, electrical conductivity, and thermal stability of the developed Cu-SiC composite due to SiC reinforcement and increasing sintering temperature [18].

5. Effect of TiO_2 nanoparticles on Cu matrix composite

TiO_2 reinforced Cu matrix composite is suitable for electrical contact materials. TiO_2 -Cu composites provide high strength at high temperatures and good electrical and thermal conductivity. Amirhossein Moghanian et al., developed Cu- TiO_2 nanocomposite by mechanical alloying. They observed that the density of the developed

A SHORT REVIEW ON THE EFFECT OF CERAMIC PARTICLES, MWCNT, AND GRAPHENE ON THE PROPERTIES OF Cu MATRIX COMPOSITES BY POWDER METALLURGY ROUTE

nanocomposite deteriorates with increasing the wt% of TiO₂. They determined the hardness and electrical resistivity of the composite. According to their observation hardness and electrical resistivity decreases with increasing the wt% of TiO₂ [19]. Abdollah Bahador et al., developed 8wt% TiO₂ reinforced Cu matrix composite by powder metallurgy process using spark plasma sintering process. Cu-8wt% TiO₂ nanocomposite provides higher tensile strength and lower ductility than pure Cu [20].

6. Effect of MWCNT on Cu matrix composite

B. Stalin et al., developed Cu-MWCNT composite by powder metallurgy process by varying the MWCNT wt% 4, 8, and 12. They observed reinforcement of MWCNT significantly enhances the relative density, hardness, and tensile strength of the developed composite. However, there is a decrease in the thermal conductivity values for 8 and 12wt% than the 4wt% MWCNT [21]. MarjanDarabi et al., developed an MWCNT reinforced Cu matrix composite with 4 and 6 vol% of MWCNT by powder metallurgy process using microwave sintering. According to their research finding as the vol% of the MWCNT increases the relative density of the developed composite decreases. The Cu-MWCNT composite with 4vol% MWCNT gives higher microhardness, bending strength, and thermal conductivity than the 6vol% MWCNT [22]. Lailesh Kumar et al. studied the mechanical and wear resistance properties of Cu-MWCNT composite developed by powder metallurgy process. There is a significant enhancement in the relative density, microhardness, and wear resistance of the 2wt% MWCNT reinforced composite [23].

7. Effect of Graphene on Cu matrix composite

Graphene is a 2D allotrope of carbon having superior mechanical, electrical, and thermal properties. F. Chen et al., developed the Cu matrix with the addition of graphene not more

than 2 vol% through molecular level mixing and spark plasma sintering process. He observed that the mechanical and thermal properties increase, while with more addition of graphene content the properties show a decrease in trend [24]. Similarly, Gao et al., developed Cu/Gr composite through the powder metallurgy route and observed that the maximum UTS and thermal conductivity achieved at 0.3 wt% graphene decreases with the increase in graphene content [25]. A similar effect has also been observed by C. Ayyappadas et al., through the powder metallurgy route, his investigation was done on varying content of graphene powder i.e., 0.9%, 1.8%, 2.7%, 3.6%, and the sintering was done on both conventional and microwave route. His observation revealed that the microwave sintering of 0.9 wt% graphene exhibits excellent electrical properties than conventional sintering. This was due to the presence of porosity in the conventional route. Thus, the addition of graphene has shown that the addition of the proper amount of graphene leads to enhanced mechanical, electrical, and thermal properties [26]. Jian wang et.al studied the microstructure, thermal, mechanical, and Corrosion properties with graphene contains of 0.5wt% 1wt% and 1.5 wt% when 0.5wt% graphene was added and the graphene dispersed in the grain boundaries of copper matrix produced a height dislocation density. When prevent dislocation movement in grain boundaries and enhanced the hardness of the G/Cu composite and also improve the corrosion resistance [27]. N.Vijayponraj et.al developed a Cu matrix composite with reinforcing graphene nano sheet (GNS) wear prepared by using the powder metallurgy technique and they study the microstructure and mechanical properties of Cu/GNS composite are better than the pure Cu with a compressive strength of 290mpa, 280mpa at 2wt% and 1wt% addition of GNS which is 10% more than pure copper [28].

A SHORT REVIEW ON THE EFFECT OF CERAMIC PARTICLES, MWCNT, AND GRAPHENE ON THE PROPERTIES OF Cu MATRIX COMPOSITES BY POWDER METALLURGY ROUTE

Table 1. Effect of Al_2O_3 , TiC, SiC, TiO_2 , and MWCNT on Cu matrix composite

Chemical compositions	Key Findings
10 to 15 wt% Al_2O_3 reinforced in Cu matrix [12]	Improves corrosion resistance and wear properties
0 to 20 wt% TiC reinforced in Cu matrix [15]	Improves tensile, hardness and wear resistance
Addition of SiC in Cu matrix [18]	Improves the mechanical, electrical and thermal properties
8wt% TiO_2 reinforced in Cu matrix [20]	Improves higher ductility and lower tensile strength
4 to 6 vol% MWCNT in Cu matrix [22]	Improves microhardness, bending strength and wear resistance
0.9 wt%, 1.8 wt%, 2.7 wt% and 3.6 wt% graphene reinforced in Cu matrix [26]	Improves mechanical, electrical and thermal properties

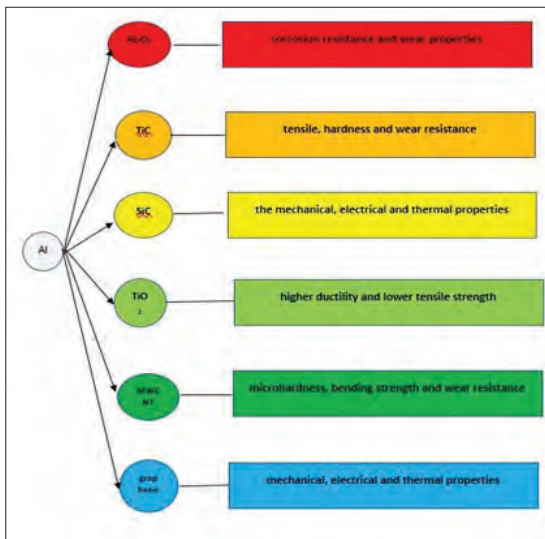


Figure 1. Variation of different reinforcement materials in Cu matrix

8. Conclusions

Copper, a poor performer of mechanical strength has shown improvement in it by suppressing its other physical properties like electrical and thermal conductivities. It also shows poor corrosion resistance while reinforcing with elements like TiC. Elements like B_4C and Al_2O_3 with increase in fraction also elevated their mechanical properties but it was observed that their electrical and thermal conductivities also

lower down. Thus, the application of copper composites poses limited application because of the restricted benefits of different reinforcement materials.

Acknowledgement

The authors acknowledge VSSUT Burla for their support to complete this work.

References

- [1] Moghadam AD, Omrani E, Menezes PL, Rohatgi PK., Mechanical and tribological properties of self-lubricating metal matrix nanocomposites reinforced by carbon nanotubes (CNTs) and graphene - A review, *Comp Part B: Engg* 2015; 77: 402-420. <https://doi.org/10.1016/j.compositesb.2015.03.014>
- [2] Pan Y, Lu X, Volinsky AA, Liu BW, Xiao SQ, Zhou C, Li Y, Chen MY, Qu XH, Tribological and mechanical properties of copper matrix composites reinforced with carbon nanotube and alumina nanoparticles, *Mater. Res. Express* 2019;6:116524. <https://doi.org/10.1088/2053-1591/ab4674>
- [3] Lin CB, Chang ZC, Tung YH, Ko YY, Manufacturing and tribological properties of copper matrix/carbon nanotubes composites, *Wear*, 2011;270: 382-394. <https://doi.org/10.1016/j.wear.2010.11.010>
- [4] Stalin B, Ravichandran M, Karthick A, Meignanamoorthy M, Sudha GT, Karunakaran S, Bharani M, Investigations on Microstructure, Mechanical, Thermal, and Tribological Behavior of Cu-MWCNT Composites Processed by Powder Metallurgy, *J Nanomater* 2021: 2021:1- 15. <https://doi.org/10.1155/2021/3913601>
- [5] Khan I, Saeed K, Khan I, Nanoparticles: Properties, applications and toxicities, *Arabian J Chem* 2019;12: 908-931. <https://doi.org/10.1016/j.arabj.2017.05.011>
- [6] Fatoba OS, Popoola O, Popoola API, The effects of silicon carbide reinforcement on the properties of Cu/SiCp composites, *Silicon* 2015; 7:351-356. <https://doi.org/10.1007/s12633-014-9199-x>
- [7] Efe GC, Ipek M, Zeytin S, Bindal C, An investigation of the effect of SiC particle size

A SHORT REVIEW ON THE EFFECT OF CERAMIC PARTICLES, MWCNT, AND GRAPHENE ON THE PROPERTIES OF Cu MATRIX COMPOSITES BY POWDER METALLURGY ROUTE

- on Cu-SiC composites, *Compo Part B: Eng* 2012; 43:1813-1822. <https://doi.org/10.1016/j.compositesb.2012.01.006>
- [8] Nazeer F, Ma Z, Gao L, Malik A, Khan MA, Abrar S, Ahmed B, Wang F, Li H, Effect of graphene on thermal and mechanical properties of copper-titanium carbide composites, *Vacuum* 2020; 173:109100. <https://doi.org/10.1016/j.vacuum.2019.109100>
- [9] Kumar L, SahooSK, Alam SN, Influence of nanostructured Cu on the mechanical properties of Cu-MWCNTs composites, *Inter J Mater Res* 2020; 111: 469-478. <https://doi.org/10.3139/146.111906>
- [10] M.F. Zawrah, Hamdia A. Zayed, Raghieba A. Essawy, Amira H. Nassar, Mohammed A. Taha, Preparation by mechanical alloying, characterization and sintering of Cu-20wt.% Al₂O₃ nanocomposites, *Mater & Design* 2012; 46:485-490. <https://doi.org/10.1016/j.matdes.2012.10.032>
- [11] Li G, Peng N, Sun D, Sun S, Friction and Wear Behavior of Nano-Al₂O₃ Particles Reinforced Copper Matrix Composites, *ASME. J. Tribol* 2015; 137: 011604. <https://doi.org/10.1115/1.4028486>
- [12] Rajesh kumar L, Amirthagadeswaran KS, Corrosion and wear behaviour of nano Al₂O₃ reinforced copper metal matrix composites synthesized by high energy ball milling, *Particulate Sci and Tech* 2020; 38:228-235. <https://doi.org/10.1080/02726351.2018.1526834>
- [13] Rajkovic V, Bozic D, Devacerski A, Jovanovic MT, Characteristic of copper matrix simultaneously reinforced with nano- and micro-sized Al₂O₃ particles, *Mater Character*;67:129-137. <https://doi.org/10.1016/j.matchar.2012.02.022>
- [14] Abd NA, Yagoob JA, Razeg KH, The Effect of Micro and Nano Size TiC Additions on Some Properties of Copper Fabricated by Powder Metallurgy, *J Nano Struc* 2021;11:588-600. <https://doi.org/110.22052/JNS.2021.03.016>
- [15] Somani N, Gupta NK, Effect of TiC nanoparticles on microstructural and tribological properties of Cu-TiC nano-composites, *Proceedings of the Institution of Mechanical Engineers, Part B: Journal of Engineering Manufacture* 2022; 236:319-336. <https://doi.org/10.1177/09544054211029828>
- [16] Nasir Ahmed Alawad, Afafjebar Muter, Optimal Control of Model Reduction Binary Distillation Column, *Inter J Modern Education and Computer Science* 2021; 1: 59-68.
- [17] Akbarpour MR, Salahi E, AlikhaniHesari F, Yoon EY, Kim HS, Simchi A, Microstructural development and mechanical properties of nanostructured copper reinforced with SiC nanoparticles, *Mater Sci Eng A* 2013;568:33-39. <https://doi.org/10.1016/j.msea.2013.01.010>
- [18] Moustafa EB, Taha MA, Evaluation of the microstructure, thermal and mechanical properties of Cu/SiC nanocomposites fabricated by mechanical alloying, *Int J Miner Metall Mater* 2021;28:475-486. <https://doi.org/10.1007/s12613-020-2176-z>
- [19] Moghanian A, Sharifianjazi F, Abachi P, Sadeghi E, Jafarikhorami H, Sedghi A, Production and properties of Cu/TiO₂ nano-composites, *J Alloys Compounds* 2016; 698:518-524. <https://doi.org/10.1016/j.jallcom.2016.12.180>
- [20] Bahador A, Umeda J, Hamzah E, Yusof F, Li X, Kondoh K, Synergistic strengthening mechanisms of copper matrix composites with TiO₂ nanoparticles, *Mater Sci Eng A* 2020;772:138797. <https://doi.org/10.1016/j.msea.2019.138797>
- [21] Sorkhe YA, Aghajani H, Tabrizi AT, Synthesis and characterisation of Cu-TiO₂ nanocomposite produced by thermochemical process, *Powder Metallurgy* 2016; 59:107-111. DOI: 10.1179/1743290115Y.0000000020
- [22] Darabi M, Rajabi M, Nasiri N, Microstructural, mechanical and thermal properties of microwave sintered Cu-MWCNT nanocomposites, *J Alloys Compounds* 2020; 822:153675. <https://doi.org/10.1016/j.jallcom.2020.153675>
- [23] Kumar L, Alam SN, Sahoo SK, Teja MBK., Mechanical Properties of Cu-MWCNT Composites Developed by Powder Metallurgy Route, *Mater Today: Proc* 2018; 5 : 19883-19892. <https://doi.org/10.1016/j.matpr.2018.06.353>
- [24] Boden A, Boerner B, Kusch P, Firkowska I, Reich S, Nanoplatelet Size to Control the Alignment and Thermal Conductivity in Copper-Graphite Composites, *Nano Letters* 2014; 14: 3640-3644. DOI: 10.1021/nl501411g

A SHORT REVIEW ON THE EFFECT OF CERAMIC PARTICLES, MWCNT, AND GRAPHENE ON THE PROPERTIES OF Cu MATRIX COMPOSITES BY POWDER METALLURGY ROUTE

- [25] Gao X, Yue H, Guo E, Zhang H, Lin X, Yao L, Wang B, Mechanical properties and thermal conductivity of graphene reinforced copper matrix composites, *Powder Technology* 2016; 301:601-607. <https://doi.org/10.1016/j.powtec.2016.06.045>
- [26] Ayyappadas, C.ao A Raja Annamalai, and Dinesh K Agrawal. An investigation on the effect of sintering mode on various properties of copper-graphene metal matrix composite *Advanced powder Technology* 28 no 7(2017):1760-1768
- [27] Wang, jain, Li-na Guo, Wan-ming, Lin, Jin Chen, Shuai Zhang, Tian-tian Zhen, and Yu-Yang Zhang. The effects of graphene content on the corrosion resistance, and electrical, thermal and mechanical properties of graphene/copper composites. *New Carbon Materials* 34, no. 2(2019):161-169.
- [28] Swikker, K. Robinstone Jeyasing, H. Kanagasabapathy, I Neethi Manickam, N Vijay Ponraj Nadar, and S. Alwin. Effect of sintering tempertaure on grain growth and mechanical properties of copper/graphene nanaosheet composite, *Dimond and Related Materials* 110(2020):108111

COST SAVING OPPORTUNITIES USING PM & APPROACH USED IN OFF HIGHWAY VEHICLES

Amol Devikar

Materials Engineering, Enterprise Technology & Engineering Center (ETEC)
John Deere India Private Ltd, Pune, Maharashtra, India
DevikarAmol@JohnDeere.com

Abstract: Powder or Sintered Metal is one of the most widely used manufacturing process globally to produce small to mid-sized components in automotive & non Automotives segment. One of main advantage of powder metallurgy process is lower cost of manufacturing over other established processes like forging, machining, casting or similar. Use of PM components in off highway vehicles are still a challenge & even today designers are still reluctant to design components using powder metallurgy. The current study is focused on 'cost saving opportunities' using PM process & approach used in off highway vehicles & highlighting different aspects for PM conversion. With harmonized approach followed, cost reduction is possible to achieve in off highway vehicles.

Keywords: powder metallurgy, off highway, cost saving, feasible criteria

1. Introduction

Use of PM components in off highway vehicles are still a challenge & even today designers are still reluctant to design components using powder metal process. The current study is focused on cost reduction approach and initiative of using Powder metallurgy for selective components used in off highway vehicles. With the standardized approach followed, cost reduction or avoidance is possible to achieve.

1.1. Common statements used by Design Engineers for PM

These are some of the few "common" statements used by design engineers for Powder or sintered metal parts, irrespective of industry-

They are porous and brittle in nature!

They are not suitable for current design load conditions..

High strengths are not possible- meant only for non-critical functions!

Suitable only for high volumes or quantities!

Limited supply base..

Cannot be coated or plated - resulting issue in corrosion, wear..

Complex shapes are not possible to manufacture!

There are many machining suppliers, who can manufacture this part...

Etc

1.2. Off highway vehicles & sintered metal

Off highway vehicles are those vehicles which are capable of driving on and off paved or gravel surface. The functions of these vehicles are more dynamic in nature compared to general automotive vehicles. Most of the off-highway vehicles fall under Agricultural & construction-forestry machines like tractors, harvesters, trucks, backhoes, loaders, etc.



Powder or Sintered Metal is one of the most widely used manufacturing process globally to produce small to mid-sized components in automotive & non Automotives. One of main advantage of powder metallurgy process is lower cost of manufacturing over other established processes like forging, machining, casting & similar.

COST SAVING OPPORTUNITIES USING PM & APPROACH USED IN OFF HIGHWAY VEHICLES

Advantages of PM -

- Net shape production, eliminates or minimizes machining
- Wide range of engineered materials (Fe, Non-Fe)
- Material/process selection permits microstructure/property control
- Facilitates manufacture of complex or unique shapes
- Lower density product, thereby reducing weight
- Uses more than 97% of the starting raw material in the finished part
- Accepted quality, reproducibility & consistency
- Efficient alloy choices
- Parts may be heat treated for increased strength or enhanced wear resistance
- Product uniqueness (Ex. Self-lubricating bearings)

Disadvantages of PM -

- Ferrous PM parts have lower ductility and reduced impact resistance compared with wrought and some cast components
- While dimensional precision is good, it does not match that of machined parts
- Cost advantage decreases as part mass increases or production volume decreases
- Parts are porous, consideration must be given to this when performing post-sintering operations
- In case of plating/ coating, additional process required – pores impregnation

With advancements in PM materials & processes, achieving the required properties & meeting “most” of the components design requirement is possible using PM.

1.3. Changing thought process



Use of PM components in off highway vehicles are still a challenge & even today designers are still reluctant to design components using ‘so called porous powder metallurgy’. Though the statement doesn’t hold true & need extensive awareness with respect to PM process & materials as a whole, but due to ‘inherent porosity’ constraint it does hold true to certain extent & may not be applicable to all category of components.

The current study is focused on ‘cost reduction opportunities’ using PM process for off highway vehicles & highlighting different aspects for PM conversion. Changing the “thought process” of the design engineer on PM was an important initial task. This was attained by gaining confidence of the engineers by conducting “Knowledge sharing sessions” on PM material & process (Internal & external speakers / experts) across the organization. These KSS included topics – PM process, materials, applications, design guidelines, advantages, limitations, supply base availability, etc. External speakers gave insights on other industry applications using PM parts. Training session slide decks were circulated to engineers further as a record.

1.4. PM feasibility criteria & approach



COST SAVING OPPORTUNITIES USING PM & APPROACH USED IN OFF HIGHWAY VEHICLES

Identifying feasible components for PM was the next step including below selection criteria & approach -

- o Part Geometry (Area, length, Diameter, shape, weight)
- o Part Quantity / volumes
- o Mechanical or physical requirements (YS, UTS, Charpy impact, fatigue, Youngs Modulus, etc)
- o Part design aspects at assembly level (loads, fastening / welding, service temp, etc)
- o Part current manufacturing location & respective PM supply base available
- o PM Supplier manufacturing capability
- o PM material selection
- o Virtual validation (FEA - Finite Element Analysis)
- o Physical validation (PV or field testing)
- o Results (implementation / learning)

Most of the PM design guideline information were captured from MPIF standard, external speaker references, ASM handbooks, PM supplier sites, etc. A compiled list was created based on the above points & feasible components were identified. Internal should costing was carried out which gave idea on cost estimation in PM vs current. Based on should costing estimation, if found feasible in terms of lower cost, request for quote (RFQ) were floated to different powder metal suppliers. Based on successful manufacturing feasibility & PM material confirmation from PM supplier, virtual validation (FEA) is planned & further will be validated with physical test using PM components.

1.5. PM feasible components

Considering inherent constraints of PM process such as porosity, higher other factors- the feasibility study was initially limited to low critical components like spacers, bushings, sprockets, sensing gear, etc.



Once successfully implemented from production intent, the study is further planned to extend to slightly more critical components from transmission & engine assemblies such as gears, rings, fittings, etc.



With standardized approach followed, cost reduction or cost avoidance is possible to attain in off highway vehicles also.

Acknowledgements

The author would like to thank PMAI Conference team for accepting the submission of this abstract & write up for PMAI 2022 event. Author would also like to thank John Deere - ETEC who directly or indirectly helped or helping in this work.

References

- <https://www.mpif.org/>
- <https://asminternational.org>
- <https://pickpm.com/>
- <https://www.hoganas.com/en/>